Chang Chuan You

Fabrication and Characterization of Ferroelectric Nanomesas: A Scanning Probe Approach

Thesis for the degree of Philosophiae Doctor

Trondheim, January 2010

Norwegian University of Science and Technology
Faculty of Information Technology,
Mathematics and Electrical Engineering
Department of Electronics and Telecommunications

NTNU
Norwegian University of
Science and Technology

NTNU
Norwegian University of Science and Technology

Thesis for the degree of Philosophiae Doctor

Faculty of Information Technology,
Mathematics and Electrical Engineering
Department of Electronics and Telecommunications

ISBN 978-82-471-1954-9 (printed ver.)
ISBN 978-82-471-1955-6 (electronic ver.)
ISSN 1503-8181

Doctoral theses at NTNU, 2010:4

Printed by NTNU-trykk

Abstract

The present study focuses on experimental investigations of size effects in ferroelectric perovskite nanostructures. When the size of a ferroelectric material is reduced down to the nanoscale, its physical properties are expected to differ considerably from the bulk properties. In order to address size effects, we have developed a novel fabrication scheme which allows us to define sub-50 nm ferroelectric $PbTiO_3$ nanomesas on prestructured $SrRuO_3$ templates, grown on $SrTiO_3$ substrates.

The $SrRuO_3$ templates were prepared using a top-down lithography technique based on scanning tunneling microscopy (STM). Surface modifications through STM line etching of $SrRuO_3$ thin films have been carried out in order to establish the etching process in a controllable and reproducible fashion. From these line etching experiments, we observed that an applied bias voltage above a threshold value was necessary for successful line etching. Moreover, the line etching was found to depend on both bias voltage and scan speed for a fixed number of scans. The depth of the etched lines increases with increasing bias voltage and scan repetitions as well as with decreasing scan speed.

The $PbTiO_3$ nanomesas were deposited on the nanostructured $SrRuO_3$ templates using an off-axis radio frequency magnetron sputtering technique. The as-grown $PbTiO_3$ nanomesas had a lateral size and a thickness down to $\sim$ 30 nm and $\sim$ 4 nm, respectively. Piezoresponse force microscopy measurements for the 4 nm thick $PbTiO_3$ nanomesas showed that the piezoelectric response increases strongly as the lateral size was reduced from $\sim$ 120 nm down to 30 nm. For the same lateral size range, a reduction of the coercive voltage was also observed. The laterally size-dependent behavior is attributed to the reduction of in-plane strain, imposed on the mesa structure by the substrate, when shrinking the lateral dimensions of the nanomesas. In addition, it was found that the $PbTiO_3$ nanomesas had a polydomain structure, similar to that observed in the as-grown, surrounding, homogeneous $PbTiO_3$ thin film.

Acknowledgements

The work presented in this thesis was carried out at the Department of Electronics and Telecommunications, Norwegian University of Science and Technology (NTNU), from January 2004 to October 2009. The support by the Research Council of Norway and the NANOMAT nationally coordinated project "Oxides for Future Information and Communication Technology" is acknowledged.

Many people have contributed to my thesis work. First, I would like to express my sincere gratitude to my supervisor professor Thomas Tybell for giving me the opportunity to work on this PhD project, and for introducing me to the exciting research field of complex perovskite oxides. This thesis work would not have been succeeded without his continuing guidance, patience, and understanding.

I am gratefully indebted to my co-supervisor professor Jostein Grepstad. His advice and suggestions have been very helpful.

I would also like to thank professor Anne Borg at the Department of Physics for the collaboration on the scanning tunneling microscopy (STM) etching of perovskite oxides. This collaboration with Anne's group was instructive and fruitful. In particular, I thank Nils Vidar Rystad, Anne's master student in 2005, for his important contribution to the experimental work on STM etching.

During my PhD studies, I also got the opportunity to work with many amiable fellow PhD students and postdocs in the Oxide Electronics group; Øystein Dahl, Lucero Alvarez, Sarin Kumar, Ryota Takahashi, Yun Liu, Ørnulf Nordseth, Espen Eberg, Erik Folven, Åsmund Monsen, and Jos Emiel Boschker, thanks a lot for your friendliness and assistance when I was stuck with technical problems in the lab. Especially, Øystein is acknowledged for sharing his experience and teaching me how to operate the sputter machine, the x-ray diffractometer, and the atomic force microscope.

Special thanks goes to my office mates, Tajeshwar Singh, Tron Arne Nilsen, and Elena Hammari, for the interesting and fun conversations we had during many lunch/tea/coffee breaks. Tajeshwar also deserves a big thanks for proofreading parts of this thesis. Also, I would like to thank the former and present staff engineers, Einar Lars Myhre, Silje Marie Nedland, Gaurav Sharma, and Steinar Smistad, for providing technical support.

Finally, I wish to thank my family and friends for their support and encouragement.

最后我衷心感谢我的家人给我的关怀和支持。

Trondheim, October 2009

Chang Chuan You (尤长川)

Contents

List of abbreviations

AC	Alternating Current
AFM	Atomic Force Microscope/Microscopy
DC	Direct Current
DRAM	Dynamic Random Access Memory
EBDW	Electron Beam Direct Writing
EBL	Electron Beam Lithography
EFM	Electrostatic Force Microscopy
FeRAM	Ferroelectric Random Access Memory
FIB	Focused Ion Beam
FWHM	Full Width at Half Maximum
GLD	Ginzburg-Landau-Devonshire
PFM	Piezoresponse Force Microscope/Microscopy
PMMA	Polymethyl Methacrylate
RF	Radio Frequency
RMS	Root-Mean-Square
SEM	Scanning Electron Microscope/Microscopy
SRAM	Static Random Access Memory
STM	Scanning Tunneling Microscope/Microscopy
XRD	X-Ray Diffraction

Clarification to author's contributions

All papers included in this thesis were written by the author. In Paper 1, the author performed the experiments shown in figures 1 and 5(c), and contributed to the development of the scanning tunneling microscopy line etching process. All experiments in Paper 2 were performed by the author. The author performed all experiments in Paper 3 except the x-ray diffraction measurements.

Chapter 1

Introduction

Nowadays, modern electronic appliances, such as MP3 players, cell phones, and personal computers, have become a part of everyday life. What these electronic devices have in common is that they all utilize random access memories (RAM) to store digital information. When it comes to data storage, there is no such thing as too *much* or too *fast* memory. For this reason, there is an ongoing effort to develop novel memories with better functionality, larger scalability, and higher performance than today's leading solid-state memory technologies, such as static RAM (SRAM), dynamic RAM (DRAM), and Flash [1, 2, 3]. Recently, ferroelectric RAM (FeRAM)[1] has emerged as one of the strong contenders for the *ultimate* memory [4], which combines the best attributes of SRAM, DRAM, and Flash. Such a memory may eliminate the need for multiple memories and may reduce the overall system cost in many applications[2] [1, 3]. As a stand-alone memory, FeRAM is currently utilized in niche products, including smart cards, automotive (e.g., smart airbags), and video game consoles [5, 6]. The key advantages of FeRAM are fast data read and write speeds, high write endurance, low power consumption (i.e., energy-saving), and non-volatile[3] data storage [6]. The main challenges FeRAM faces today are lower storage density and higher cost compared to, e.g., Flash. Hence, in order to achieve cost-effective high-density data storage devices based on FeRAM, it is necessary to develop appropriate manufacturing techniques which can scale down ferroelectric components to smallest sizes.

---

[1] In a FeRAM, the bistable + or − polarization states of a ferroelectric material are used to represent a bit of data storage, as "1" or "0".

[2] For example in so-called embedded applications, where an entire electronic system is implemented on a single device with SRAM, DRAM, and Flash often used together.

[3] Non-volatility means that the data is retained even when the power is switched off.

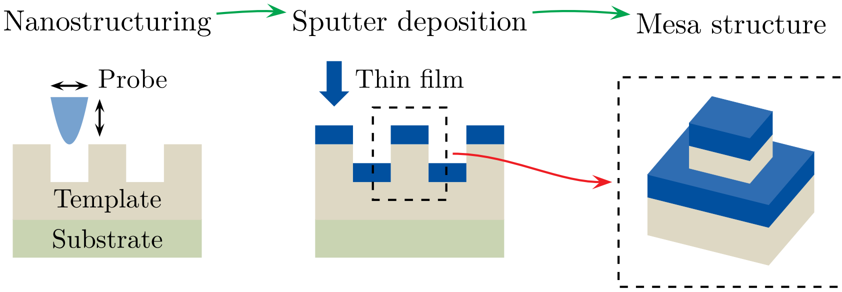

Figure 1.1: Schematic illustration of the fabrication scheme for achieving nanoscale ferroelectric mesa structures.

Ferroelectric materials are not only appealing for memory devices, but they also possess useful electrical and mechanical properties, such as dielectricity, piezoelectricity, and pyroelectricity, interesting for a wide range of potential nanodevice applications, for example in sensors, actuators, surface acoustic wave filters, and electro-optic modulators [7, 8, 9, 10]. However, when the size of ferroelectric materials becomes smaller and approaches the nanometer length scale, their physical properties are observed to differ from the bulk properties [11, 12, 13, 14]. A sound understanding of how these properties behave at the nanoscale is therefore essential for the incorporation of ferroelectric materials in future nanoelectronic applications. For example, for memory nanodevices, evaluating the size limit, below which the ferroelectricity disappears, will also yield valuable information about the maximum attainable data storage density. Furthermore, probing finite size effects in materials with the smallest dimensions might lead to new insights on the fundamental physical mechanisms responsible for nanoscale ferroelectricity [12, 15]. The development of appropriate nanostructuring techniques, which can provide the capability to produce high-quality and well-defined nanostructures, plays therefore a key role in terms of facilitating experimental investigations of ferroelectric size effects.

The primary goal of the present study is therefore to investigate how reduced material size affects the physical properties. In order to explore size effects, we aim to develop a novel fabrication scheme which allows us to define sub-50 nm ferroelectric perovskite nanostructures with a controlled geometry. This fabrication scheme is schematically outlined in figure 1.1, and involves the following two steps:

1. Definition of nanoscale templates into the surface of a perovskite oxide thin film (e.g., $SrRuO_3$) using extremely fine scanning probes, based on scanning tunneling microscopy (STM) nanostructuring

2. Subsequent sputter deposition of a desired ferroelectric perovskite thin film (e.g., $PbTiO_3$) on top of predefined templates. Laterally confined isolated mesa structures are formed on the templates when the thickness of the deposited film is less than the depth of the etched trenches, defined by the templates

To map out the dependence of ferroelectric properties on the lateral size for such $PbTiO_3$ nanomesas grown on $SrRuO_3$ templates, we use a nanoscale characterization technique based on piezoresponse force microscopy (PFM).

This thesis is organized as follows. In chapter 2 an introduction of ferroelectricity is given. Chapter 3 presents a literature overview of state-of-the-art fabrication methods for achieving ferroelectric nanostructures, including some interesting experimental observations of ferroelectric size effects. The experimental techniques are described in chapter 4. In chapter 5, the STM nanostructuring of $SrRuO_3$ thin film surfaces is given (Paper 1 [16]). Chapter 6 reports the fabrication and characterization of $PbTiO_3$ nanomesas realized on nanostructured $SrRuO_3$ templates (Paper 2 [17]). Chapter 7 presents the PFM study of the ferroelectric domain structure in $PbTiO_3$ thin films and nanomesas (Paper 3). Finally, conclusions are drawn in chapter 8 together with outlook.

References

[1] U. Böttger and S. R. Summerfelt. Ferroelectric random access memories. In R. Waser, editor, *Nanoelectronics and Information Technology*, pages 565–606. Darmstads: Wiley-VCH Verlag, 2003.

[2] O. Auciello, J. F. Scoot, and R. Ramesh. The physics of ferroelectric memories. *Physics Today*, 51:22, 1998.

[3] J. Åkerman. Toward a universal memory. *Science*, 308:508, 2005.

[4] J. F. Scott. Nanoferroelectrics: statics and dynamics. *J. Phys.: Condens. Matter*, 18:361, 2006.

[5] J. F. Scott. *Ferroelectric Memories.* Berlin Heidelberg: Springer-Verlag, 2000.

[6] G. R. Fox, R. Bailey, W. B. Kraus, F. Chu, S. Sun, and T. Davenport. The current status of FeRAM. In H. Ishiwara, M. Okuyama, and Y. Arimoto, editor, *Ferroelectric Random Access Memories*, volume 93 of *Topics in Applied Physics*, pages 139–149. Berlin Heidelberg: Springer-Verlag, 2004.

[7] M. E. Lines and A. M. Glass. *Principles and Applications of Ferroelectrics and Related Materials.* Oxford: Clarendon Press, 1979.

[8] A. K. Sarin Kumar, P. Paruch, J.-M. Triscone, W. Daniau, S. Ballandras, L. Pellegrino, D. Marré, and T. Tybell. High-frequency surface acoustic wave device based on thin-film piezoelectric interdigital transducers. *Appl. Phys. Lett.*, 85:1757, 2004.

[9] B. W. Wessels. Ferroelectric epitaxial thin films for integrated optics. *Annu. Rev. Mater. Res.*, 37:659, 2007.

[10] J. F. Scott. Applications of modern ferroelectrics. *Science*, 315:954, 2007.

[11] T. M. Shaw, S. Trolier-McKinstry, and P. C. McIntyre. The properties of ferroelectric films at small dimensions. *Annu. Rev. Mater. Sci.*, 30:263–298, 2000.

[12] C. H. Ahn, K. M. Rabe, and J.-M. Triscone. Ferroelectricity at the nanoscale: Local polarization in oxide thin films and heterostructures. *Science*, 303:488, 2004.

[13] M. Dawber, K. M. Rabe, and J. F. Scott. Physics of thin-film ferroelectric oxides. *Rev. Mod. Phys.*, 77:1083–1130, 2005.

[14] C. Lichtensteiger, M. Dawber, and J.-M. Triscone. Ferroelectric size effects. In K. M. Rabe, C. H. Ahn, and J.-M. Triscone, editor, *Physics of Ferroelectrics: A Modern Perspective*, volume 105 of *Topics in Applied Physics*, pages 305–338. Berlin Heidelberg: Springer-Verlag, 2007.

[15] J. F. Scott. Novel geometric ordering of ferroelectricity. *Nat. Mater.*, 4:13, 2005.

[16] C. C. You, N. V. Rystad, A. Borg, and T. Tybell. Nanoscale structuring of $SrRuO_3$ thin film surfaces by scanning tunneling microscopy. *Appl. Surf. Sci.*, 253:4704, 2007.

[17] C. C. You, R. Takahashi, A. Borg, J. K. Grepstad, and T. Tybell. The fabrication and characterization of $PbTiO_3$ nanomesas realized on nanostructured $SrRuO_3/SrTiO_3$ templates. *Nanotechnology*, 20:255705, 2009.

Chapter 2

Ferroelectricity

In this chapter the basic properties of ferroelectric materials, such as spontaneous polarization, domains, and polarization switching, are reviewed. A phenomenological theory based on thermodynamics, originally developed by Devonshire using the Ginzburg-Landau formalism to describe such macroscopic properties, is presented. The piezoelectric properties of ferroelectrics are also discussed. Finally, theoretical predictions of ferroelectric size effects are mentioned, while experimental observations of size effects will be given in chapter 3.

2.1 Basic properties

Ferroelectrics are insulating materials exhibiting a spontaneous electric polarization in the absence of an external electric field. A very technologically important and extensively studied group of ferroelectrics is based on the pseudo-cubic perovskite structure with general formula ABO_3, as sketched in figure 2.1(a). The valence of the A cations at the cube corners is +1 or +2 and of the B cations at the body centers is +4 or +5 [1]. The B cation is surrounded by an octahedron, formed by the oxygen anions at the cube face centers. A typical example of ferroelectric perovskites is $PbTiO_3$, which is the material used in this study. At high temperatures, above the phase transition Curie temperature T_c, a ferroelectric material behaves like an ordinary dielectric and is termed paraelectric. When the temperature is decreased below T_c, a symmetry breaking structural phase transition[1]

---

[1] In some ferroelectric perovskites such as $BaTiO_3$, successive transitions to three different lower-symmetry ferroelectric phases (tetragonal, orthorhombic, and rhombohedral) are observed as the temperature is lowered. However, in $PbTiO_3$, only a single transition takes place from a cubic paraelectric phase to a tetragonal ferroelectric phase.

(a) $T > T_c$

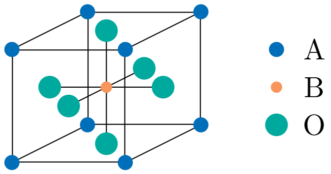

(b) Phase transition: $T < T_c$

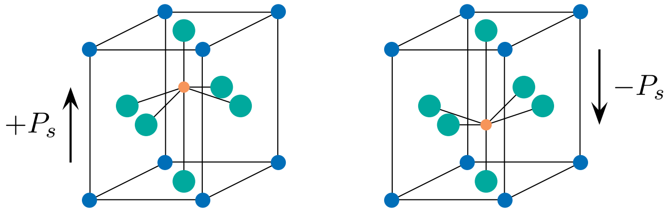

Figure 2.1: (a) ABO_3 unit cell structure of a ferroelectric perovskite in the high-temperature paraelectric cubic phase. (b) At $T < T_c$, the ferroelectric perovskite undergoes a crystal symmetry breaking phase transition from the cubic phase to the tetragonal phase with two possible polarization states, $+P_s$ and $-P_s$, which can be switched by an external electric field.

may take place from a high-temperature paraelectric cubic phase to a low-temperature ferroelectric tetragonal phase, as described in figure 2.1(b). In the tetragonal phase, the center of gravity for the positive charges (cations) is displaced relative to the center of gravity for the negative charges (anions), giving rise to a nonzero microscopic electric dipole moment in each unit cell, and a macroscopic spontaneous polarization of the material. In addition, there exists two symmetry equivalent polarization states, $\pm P_s$, oriented in parallel with the c-axis of the material. For a material to be considered ferroelectric, it must be possible to switch between these polarization states with an external electric field [1, 2].

In a tetragonal ferroelectric material such as $PbTiO_3$, the spontaneous polarization is usually not oriented along the same direction throughout the whole material. The regions of the material with uniform orientation of the spontaneous polarization are termed ferroelectric domains. Two neighboring domains are separated by a domain wall, as shown by the gray regions in figure 2.2. Domains with oppositely oriented polarization are separated by 180° walls (figure 2.2(a)), while regions with mutually perpendicular polarization are divided by 90° walls (figure 2.2(b)). The width of a 180° domain

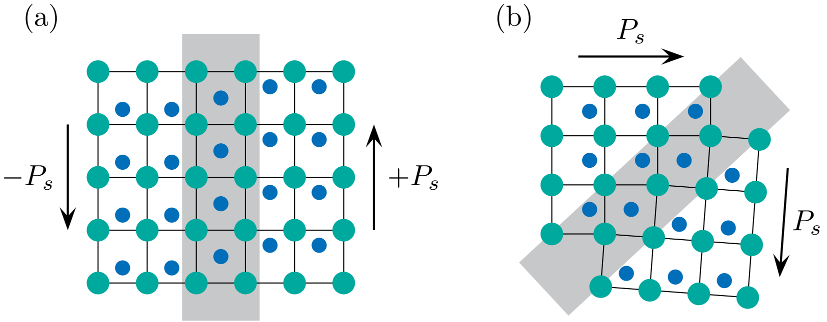

Figure 2.2: Schematic illustration of ferroelectric domains having a 180° (a) and 90° (b) wall in a tetragonal ferroelectric perovskite. From [4].

wall is typically in the range of $1-10$ nm [3]. The occurrence of ferroelectric 180° domain walls is due to the electrostatic energy associated with depolarization fields. The depolarization field is generated by uncompensated charges at the material surface or by an inhomogeneous distribution of polarization[2]. The depolarization field is oriented oppositely to the direction of polarization, thus renders a monodomain state energetically unfavorable. As a result, multiple domains with antiparallel polarizations are formed in order to minimize the depolarization field. The depolarization field can also be reduced if the surface charges are compensated for by screening charges from the surrounding medium, for instance, through short-circuited metal electrodes deposited on the ferroelectric material [1].

An important feature of ferroelectric materials is the possibility to switch between the stable polarization states by an electric field. Figure 2.3 illustrates a polarization versus electric field ($P-E$) hysteresis loop. When an electric field is applied, domains with an unfavorable direction of polarization are switched in the same direction as the field. New domains with reversed polarization can also nucleate, which then grow and coalesce by domain wall motion. When all the domains are reversed the polarization starts to saturate. The polarization remaining at zero field is termed remanent polarization, P_r. The induced polarization is not vanished at zero field, but instead at a negative field $-E_c$, which is called the coercive field[3]. When the field is raised above $+E_c$, a hysteresis loop is obtained between

---

[2] In general, any spatial variation of polarization acts as a source for a depolarization field, for instance, in the presence of a defect or grain boundary.

[3] The coercive field for bulk ferroelectrics is typically on the order of 10 to 100 kV/cm. This relatively small value reflects the fact that polarization reversal generally takes place through nucleation and growth of domains.

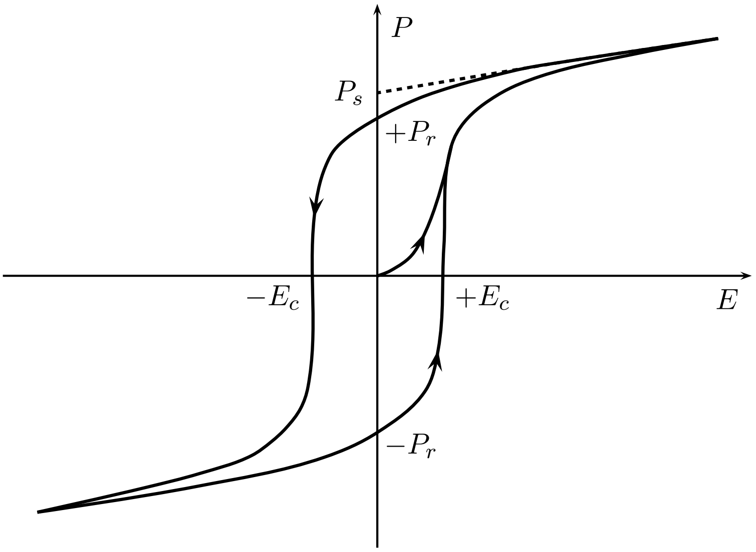

Figure 2.3: Ferroelectric $P - E$ hysteresis loop. P_s and P_r are the spontaneous and remanent (zero field) polarization, respectively. E_c is the coercive field, necessary to reduce the polarization to zero. From [4].

the two nonzero values of the spontaneous polarization, $\pm P_s$. P_s is usually defined as the extrapolation to zero field of the linear segment of the saturated polarization at high field [4].

2.2 Thermodynamics of ferroelectrics

Changes of macroscopic properties, such as polarization and permittivity, at a phase transition from a high-temperature high-symmetry paraelectric phase to a low-temperature low-symmetry ferroelectric phase can be described by phenomenological Ginzburg-Landau-Devonshire (GLD) theory based on thermodynamics, using for example the Gibbs free energy. The theory is based on the idea of an order parameter, which is used to define the ferroelectric phase in terms of deviations from the atomic arrangement of the non-polar paraelectric phase. The phase transition is characterized as first or second order. The order of the phase transition is defined by the discontinuity in the partial derivatives of the Gibbs free energy. For a ferroelectric second order phase transition, the spontaneous polarization and strain change continuously at T_c, while they become discontinuous for a first order phase transition. For example, $PbTiO_3$ is a ferroelectric material with a first order phase transition and LiNbO3 is a ferroelectric with a second order phase transition. Assuming that the direction of both polarization and applied electric field takes place along one of the crystallographic axes, and that all stresses are zero, and that the non-polar phase is centrosymmetric, the elastic Gibbs free energy, G_1, can be expressed by a simple polynomial thermodynamic potential with even-order terms

$$G_1 = \frac{\alpha}{2}D^2 + \frac{\gamma}{4}D^4 + \frac{\delta}{6}D^6 \tag{2.1}$$

where the electric displacement, D, is used as the order parameter. D is correlated to P_s via

$$D = P_s + \varepsilon E \tag{2.2}$$

where ε is the dielectric permittivity. A stable ferroelectric state is obtained when the elastic Gibbs free energy hits a minimum at constant temperature. The condition for the free energy minimum is given by

$$\frac{\partial G_1}{\partial D} = E = \alpha D + \gamma D^3 + \delta D^5 \tag{2.3}$$

where α, γ, and δ are material-dependent coefficients. For simplicity, only coefficient α is assumed to be temperature dependent. Close to the transition temperature, α depends linearly on temperature in the form $\alpha = \beta(T - T_0)$, where β is a positive constant, and T_0 is called the Curie-Weiss temperature and is not equal to the transition temperature T_c for a first order phase transition. Coefficient δ must be positive because G_1 can not become $-\infty$ when $D \to +\infty$. Hence, the order of the phase transition depends on the sign of γ. The transition is of first order for $\gamma < 0$ and second order for $\gamma > 0$ [1, 4].

2.2.1 Second order phase transition

The elastic Gibbs energy versus the electric displacement for a second order phase transition is qualitatively illustrated in figure 2.4(a). With coefficients γ and δ being positive, the free energy function has a single minimum at $D = 0$ for $\alpha \geq 0$, but for $\alpha < 0$ the function has two minima appearing at nonzero values of D. These minima correspond to the equilibrium values of spontaneous polarization in the absence of an external electric field. As α is passed through zero, P_s undergoes a continuous second order phase transition. For $E = 0$, it follows that $D = P_s$, an expression for P_s can be derived from equation (2.3)

$$P_s(\alpha + \gamma P_s^2 + \delta P_s^4) = 0 \tag{2.4}$$

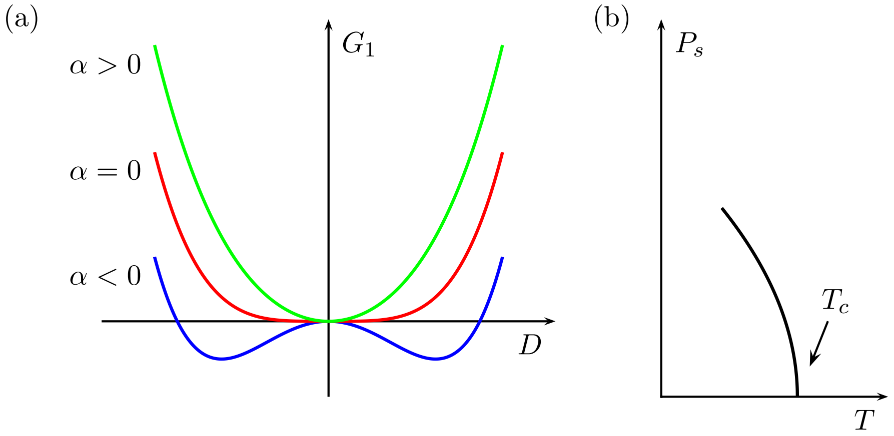

Figure 2.4: (a) Elastic Gibbs free energy G_1 versus electric displacement D for a second order phase transition. (b) Spontaneous polarization P_s versus temperature T near a second order ferroelectric transition. From [1].

Solving the above equation for $P_s \neq 0$ and $\gamma^2 \gg \alpha\delta$, one obtains

$$P_s^2 = -\frac{\alpha}{\gamma} = \frac{\beta(T_0 - T)}{\gamma} \tag{2.5}$$

where $T < T_0 = T_c$ for a second order phase transition. Equation (2.5) gives two possible equilibrium orientations of P_s, namely, $+P_s$ and $-P_s$. Close to T_c, P_s approaches continuously towards zero, as schematically shown in figure 2.4(b).

Based on equation (2.3) we can deduce an expression for the dielectric permittivity ε just above T_c, in the paraelectric phase where $P_s = 0$ with zero field. Differentiating E with respect to D gives the reciprocal permittivity

$$\frac{1}{\varepsilon} = \frac{\partial E}{\partial D} = \beta(T - T_c) \tag{2.6}$$

ε has a temperature dependence similar to that of α, and it diverges rapidly as T_c is approached from above.

The spontaneous polarization in response to an applied electric field can also be derived from equation (2.3), as schematically shown in figure 2.5, where D is plotted as a function of E for a second order phase transition. The dashed and dotted curves represent regions which correspond to unstable and metastable states of the system, respectively. When the external field exceeds the coercive field, defined as the intercepts on the E-axis, the metastable state jumps abruptly to the equilibrium stable state, as indicated

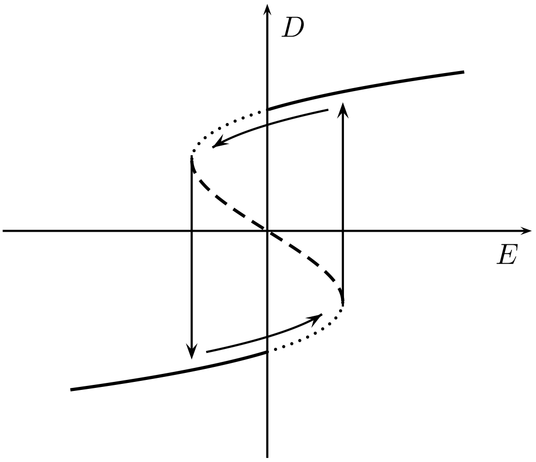

Figure 2.5: Schematic illustration of D versus E for $T < T_c$. The dashed curve represents regions of instability and dotted curve regions of metastability. The long arrow denotes transition from a metastable state to a stable equilibrium state when the applied electric field exceeds the coercive field, as defined by the intercepts on the E-axis. From [1].

by the long arrows. The GLD theory predicts a so-called intrinsic coercive field [5], which is the field necessary to reverse the spontaneous polarization *homogeneously* over the ferroelectric sample, without the domain nucleation and growth processes.

2.2.2 First order phase transition

For a first order phase transition with $\gamma < 0$, the elastic Gibbs free energy function has equal minima at $D = 0$ and at $D = \pm D_c$ at T_c, as qualitatively shown in figure 2.6(a). In the absence of an external electric field, a first order phase transition takes place when $G_1 = 0$ and $\partial G_1/\partial D = 0$ for nonzero values of D if the following conditions are simultaneously satisfied

$$\frac{\beta}{2}(T - T_0) - \frac{\gamma'}{4}P_s^2 + \frac{\delta}{6}P_s^4 = 0 \tag{2.7}$$

$$\beta(T - T_0) - \gamma' P_s^2 + \delta P_s^4 = 0 \tag{2.8}$$

where $\gamma' = -\gamma$. For $T = T_c$, the solution is given by

$$T_c = T_0 + \frac{3}{16}\frac{\gamma'^2}{\beta\delta} \tag{2.9}$$

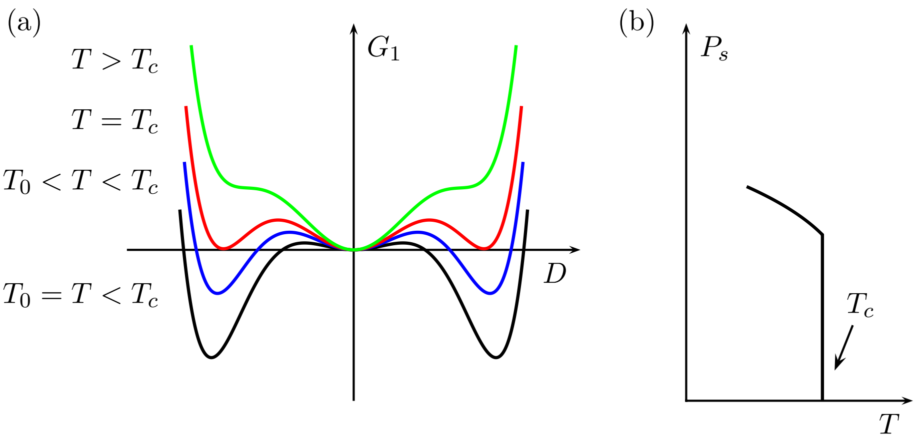

Figure 2.6: (a) Elastic Gibbs free energy G_1 versus electric displacement D for a first order phase transition. (b) P_s versus T. From [1].

Note that $T_c > T_0$ for a first order phase transition. The spontaneous polarization at T_c can be obtained by inserting equation (2.9) into (2.7)

$$P_s^2 = \frac{3\gamma'}{4\delta} \tag{2.10}$$

As shown in figure 2.6(b), P_s jumps from zero to $\sqrt{\frac{3\gamma'}{4\delta}}$ at T_c. Hence, the system undergoes a first order phase transition from stable states at $T = T_c$ with a discontinuity in spontaneous polarization.

2.3 Piezoelectricity

All ferroelectric materials are also piezoelectric, i.e., the material can be polarized by applying a mechanical stress in addition to an electric field. This is known as the direct piezoelectric effect (figure 2.7(a)), and the induced electric displacement D can be written as

$$D_i = d_{im}^E \sigma_m + \varepsilon_{ij}^\sigma E_j \tag{2.11}$$

where the piezoelectric coefficient, d_{im}, is a third-rank tensor written in the matrix notation, and σ is the applied stress. In addition, the material dimensions may be changed in response to an applied electric field and stress, which is known as the converse piezoelectric effect, and the induced strain e can be expressed as

$$e_m = s_{mn}^E \sigma_n + d_{im}^\sigma E_i \tag{2.12}$$

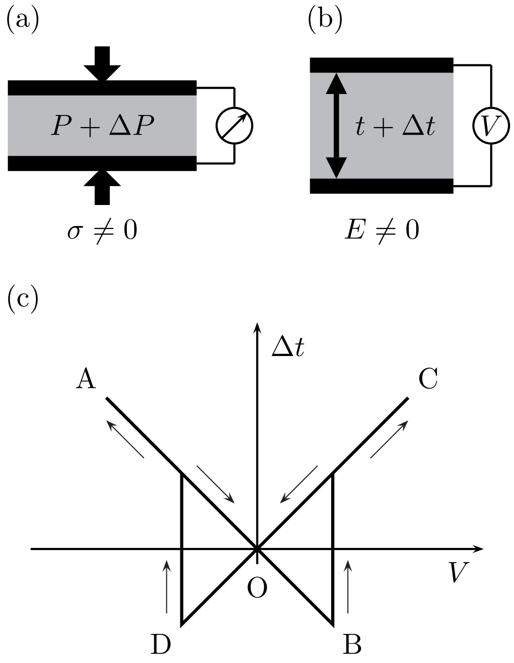

Figure 2.7: (a) A bulk ferroelectric sample is polarized by ΔP when subjected to a mechanical stress, σ, in the absence of an external electric field. (b) The thickness of a sample is changed by Δt when a voltage V is applied across the ferroelectric capacitor. (c) Schematic representation of an idealized butterfly-shaped $\Delta t - V$ hysteresis loop for a ferroelectric monodomain sample in which the direction of polarization switches only by 180° reversal. From [4].

where the elastic compliance s_{mn} is a fourth-rank tensor. The subscripts[4] $i, j = 1, 2, 3$ and $m, n = 1, 2, \ldots, 6$, and the superscripts σ, E denote coefficients at constant stress and electric field, respectively.

Since the piezoelectric coefficient d_{im} is a tensor quantity, it means that the piezoelectricity depends on the direction of the applied electric field. As a result, the measured piezoelectric strain may consist of contributions from d_{im} along the field direction and other nonzero values of d_{im} which are coupled to the electric field. When an electric field is applied across a stress-free bulk ferroelectric sample, with thickness t, sandwiched between top and bottom metallic electrodes (figure 2.7(b)), the resulting longitudinal

---

[4] The number of unique coefficients in equations (2.11) and (2.12) depends on the symmetry class of the ferroelectric crystal [6].

strain (i.e., perpendicular to the sample surface) is given by

$$e_3 = d_{33}E_3 \Rightarrow \Delta t = d_{33}V \tag{2.13}$$

where Δt is the change in sample thickness and V is the applied voltage. Note that the resulting thickness change, Δt, can be estimated from V. Additionally, by changing the sign of V, the sample may contract or expand. Figure 2.7(c) illustrates how induced strain (Δt) of a ferroelectric monodomain single-crystal (e.g., $PbTiO_3$) changes ideally with the applied electric field (or voltage), assuming that polarization can be instantaneously switched by 180° reversal [4]. At zero field (point O in figure 2.7(c)), the strain of the sample is taken to be zero. The sample expands via the converse piezoelectric effect, according to equation (2.12), as the voltage increases from O to A, with the direction of the field parallel to the direction of polarization. From A to O, the voltage decreases and the strain is again zero at O. From O to B, the sample contracts because the direction of the field is antiparallel to the direction of polarization. However, when the voltage is raised above B, the direction of polarization is reversed, thus the sample expands again with increasing voltage towards C. As the voltage is lowered, the strain reaches zero at O. The sample begins to contract as the voltage is further reduced due to the field is oriented oppositely to the direction of polarization. When the voltage exceeds point D, the direction of polarization is reversed, i.e., parallel to the field, the sample expands again towards A, defining a butterfly-shaped hysteresis loop ABCDA. Such piezoelectric hysteresis loop measurements can be carried out using PFM [7] (see chapter 4.4). The PFM technique also provides the possibility to probe local, nanoscale, piezoelectric properties in ferroelectric thin films and nanostructures.

2.4 Ferroelectric size effects

Ferroelectricity is classically viewed as a collective phenomenon with a spontaneous polarization arising from the alignment of localized dipoles within a finite correlation volume [1]. In this picture, the delicate balance between short-range (E_{SR}) dipolar forces and long-range dipole-dipole (E_{DD}) interactions play an important role for the stability of ferroelectricity [8]. Since the parallel alignment of dipoles in a ferroelectric is due primarily to strong long-range dipole-dipole (figure 2.8(a)) interactions along the longitudinal polar c-axis and weaker short-range (figure 2.8(b)) interactions along the transverse direction, i.e., perpendicular to the c-axis, the correlation volume

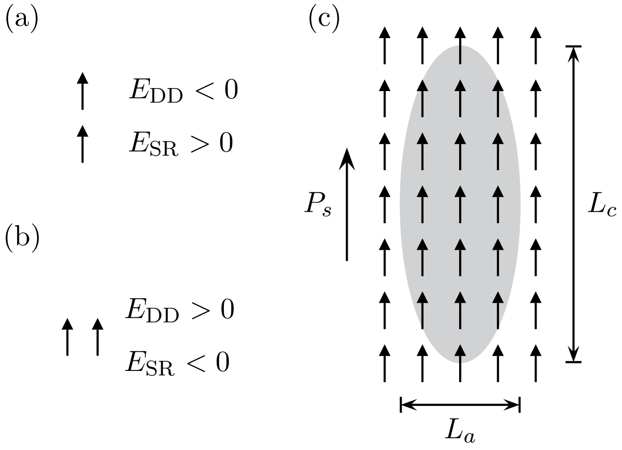

Figure 2.8: Contributions of long-range dipole-dipole (E_{DD}) and short-range (E_{SR}) interactions to the energy of a system made of a dipole alignment (a) along the polar c-axis or (b) along the normal to this axis. (c) Schematic drawing of a needle-shaped anisotropic correlation volume oriented along the polar c-axis of perovskite ferroelectrics. From [1, 8].

is expected to be highly anisotropic. This anisotropy arises because for electric dipolar forces the parallel alignment of an isolated pair of c-axis dipoles are more energetically favorable compared to an isolated pair of dipoles normal to the polar axis. Typically, the correlation volume is viewed as a needle-shaped ellipsoid of a size defined by two characteristic lengths, L_a and L_c, as schematically shown in figure 2.8(c). Typical accepted values for many perovskite ferroelectrics are $L_a = 1 - 2$ nm and $L_c = 10 - 50$ nm, leading to correlation volumes of $10 - 100$ nm^3. Hence, when the physical dimensions of a ferroelectric material are reduced, the ferroelectric phase is expected to become less stable, and eventually disappears below a critical size.

2.4.1 Thin films and nanoparticles

Size effects in the Ginzburg-Landau-Devonshire theory

The phenomenological GLD model, as discussed in chapter 2.2, has been extensively used to study the effects of size on the physical properties of finite, nanostructured, ferroelectric systems, such as thin films and nanoparticles [9, 10, 11, 12, 13, 14]. The total free energy, F, of a finite-sized and inhomogeneous ferroelectric can be generally written as (see, for instance, [12])

$$\begin{aligned} F = &\int_V \left[\frac{1}{2}AP^2 + \frac{1}{4}BP^4 + \frac{1}{6}CP^6 + \frac{1}{2}D(\nabla P)^2 - E_{\text{ext}}P\right] \mathrm{d}V \\ &+ \frac{D}{2\delta}\int_S P^2\,\mathrm{d}S \end{aligned} \tag{2.14}$$

where P is the polarization and E_{ext} is the external electric field. S represents a closed surface of a ferroelectric of volume V. Here, $A = A_0(T - T_0)$, and A_0, B, C, D, and δ are material parameters. Note that $B < 0$ for a first order phase transition, and $B > 0$ and $C = 0$ for a second order phase transition [10]. The first three terms in the first integral measure the conventional free energy of an infinite and homogeneous system, as previously described in chapter 2.2. The gradient term gives the free energy from inhomogeneous polarization, while the surface integral calculates the free energy contribution due to variation of polarization at the surface. The extrapolation length, δ, is a measure of the strength of the surface effect, describing whether the polarization at the surface is enhanced or suppressed compared to the bulk value. In general, δ depends on the coordination number within the surface layer, as well as the inter-site interaction [12]. For a thin film geometry, δ is independent on the film thickness because the surface coordination number does not vary with the film thickness. On the other hand, for nanostructures with a geometry of cylinder or sphere, such as nanowires and nanoparticles, the coordination number decreases as the size is reduced. As a result, δ is size-dependent for nanoparticles. When $\delta < 0$, the polarization at the surface is enhanced relative to that of the bulk value. When $\delta > 0$, the polarization at the surface is reduced. For perovskite ferroelectrics, δ is estimated to be typically $\sim 1 - 10$ nm, and it is usually taken as positive, which means that the polarization at the surface is suppressed [10, 13].

The main results from the GLD model for perovskite nanoparticles can be summarized as follows: (1) A size driven ferroelectric−paraelectric phase transition takes place when the particle size is below a critical size, below which the ferroelectricity is disappeared. (2) The size driven phase transition has the same order as the phase transition driven by the temperature. (3) The transition temperature, T_c, drops as the particle reaches the critical size, at which the permittivity is increased while the polarization becomes zero. For $PbTiO_3$ and $BaTiO_3$ nanoparticles, the theoretically predicted critical sizes are 4.2 and 44 nm, respectively [10].

The strong anisotropic character of the dipole-dipole interaction was taken into account by Li *et al.* [13, 14], and they examined the size limits in nanostructured ferroelectrics under short-circuit boundary conditions.

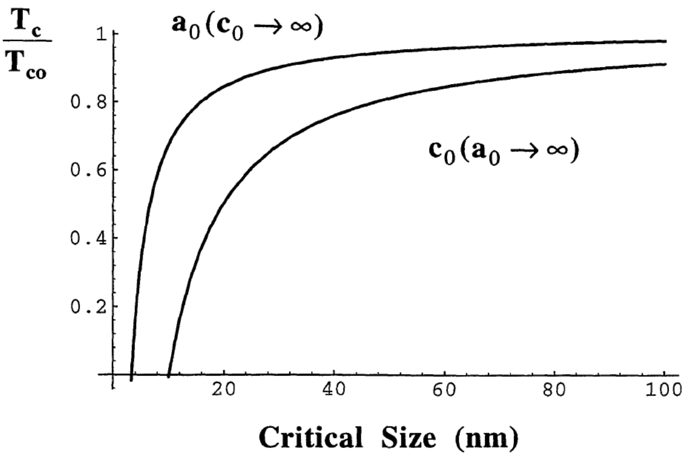

Figure 2.9: Transition temperature versus the minimum critical thickness and lateral dimensions of a $PbTiO_3$ cell. The upper and lower curves represent the laterally confined (i.e., corresponding to a nanowire structure) and the thin film geometries, respectively. It is shown that the minimum film thickness and lateral size at which ferroelectricity is suppressed, at $T_c = 0$ K, are $\sim$ 3 and $\sim$ 1 nm, respectively. From [14].

Figure 2.9 displays the results from the calculations for a $PbTiO_3$ cell. As shown, at $T_c = 0$ K, the critical thickness c_0 and lateral size a_0, below which the ferroelectric phase becomes unstable, are $\sim$ 3 nm and $\sim$ 1 nm, respectively. For a $Pb(Zr_{0.5}Ti_{0.5})O_3$ cell, the critical thickness and lateral size are $\sim$ 10 nm and $\sim$ 4 nm. At room temperature, the critical thickness are $\sim$ 18 nm for $Pb(Zr_{0.5}Ti_{0.5})O_3$ and $\sim$ 5 nm for $PbTiO_3$. Moreover, within this model a critical volume can be obtained at a given thickness. As an example, the critical lateral size of an infinitely thick ($c_0 \rightarrow \infty$) $BaTiO_3$ is $\sim 2 - 3$ nm, and it increases to $5 - 6$ nm as the thickness is reduced to 40 nm [13]. This indicates that the characteristic sizes of a confined system are anisotropic in character, and that the lateral size effect is cooperatively associated with the thickness.

In the above theoretical calculations, the depolarization effects were neglected. For thin films, it has been previously shown that the calculated spontaneous polarization is suppressed [15] and the transition temperature is reduced [16] if the depolarization field is taken into consideration. Therefore, the model underestimates the critical size. When the polarization is not well screened at the interfaces, or varying inhomogeneously inside the ferroelectric, an increase of the minimum critical size should be expected.

It should also be pointed out that the calculations were performed for free-standing films. Recently, Zembilgotov *et al.* [17] have studied the effect compressive strain, imposed on the film by a thick substrate, has on the polarization. According to their calculations for $PbTiO_3$ and $BaTiO_3$ films, a strong decrease of the polarization at room temperature is expected only for ultrathin films with thicknesses of ~ 1 nm.

Predictions from first-principles calculations

Recent first-principles calculations [18] have focused on predictions of size effects in ultrathin perovskite films, with an emphasis on the influence that the mechanical and electrostatic boundary conditions have on the stability of ferroelectricity [19, 20, 21, 22, 23, 24, 25]. For instance, it has been shown by Ghosez and Rabe [19] that stress-free $PbTiO_3$ films, as thin as 3 unit cells, exhibit a spontaneously polarized ferroelectric ground state, with the polarization perpendicular to the surface, when the depolarization field is not taken into account. Later, Junquera and Ghosez [22] performed first-principles calculations for a realistic $SrRuO_3/BaTiO_3/SrRuO_3$ capacitor under short-circuit conditions, and showed that the large depolarization fields, caused by dipoles at the ferroelectric−metal interfaces, will destabilize ferroelectricity in monodomain, defect-free perfectly insulating, $BaTiO_3$ films with thicknesses less than 2.4 nm (6 unit cells). Furthermore, it was found that the depolarization field depends linearly on the polarization of the thin film and is inversely proportional to the film thickness. This residual depolarization field couples with the polarization, giving rise to an extra electrostatic energy that tends to reduce the polarization. Figure 2.10

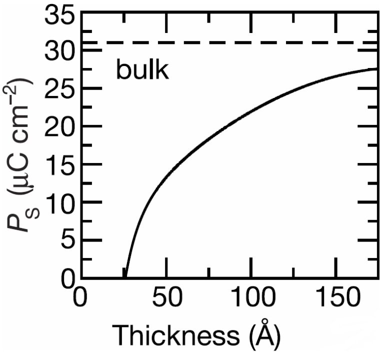

Figure 2.10: The spontaneous polarization versus thickness of $BaTiO_3$ thin films. From [22].

displays the evolution of the spontaneous polarization with thickness. As shown, the depolarization field reduces the amplitude of the spontaneous polarization, which only reaches the bulk value for increasing film thickness. According to recent calculations for $PbTiO_3$ thin films sandwiched between $SrRuO_3$ electrodes, a stable monodomain ferroelectric state can persist in films less than 1 nm thick [24]. In contrast to the results from the GLD calculations discussed above, the first-principles calculations, overall, suggest that the ferroelectricity can be preserved at the monolayer level under appropriate boundary conditions. Hence, no thickness limit is imposed on practical thin film ferroelectric devices.

2.4.2 Nanowires and nanodots

Recently, there has been an increasing focus on the investigation of physical properties of ferroelectric perovskite nanostructures, such as nanowires, nanorods, and nanodots, using phenomenological GLD theory [26, 27, 28] and atomic simulations [29, 30, 31, 32, 33, 34, 35]. Several groups have studied the influence of size on the stability of ferroelectricity in nanowires. For example, Geneste *et al.* [33] performed first-principles calculations on $BaTiO_3$ nanowires, and they predicated that the suppression of the ferroelectric distortion along the wire axis may take place below a critical diameter of 1.2 nm.

In a series of study by Bellaiche and co-workers [29, 30, 32, 35], a novel domain pattern of electric dipoles, in the form of a vortex structure, has been predicated to occur in ultrasmall ferroelectric perovskite nanostructures, when their dimensions approach the order of a few nm. Figure 2.11 illustrates the local dipole pattern in a $Pb(Zr_{0.5}Ti_{0.5})O_3$ nanorod with a diameter of 2.8 nm and a length of 11.2 nm [30]. Similar vortex dipole pattern is also expected in $BaTiO_3$ nanodots smaller than ~ 5 nm [29]. Furthermore, atomic simulations showed that the formation of vortex structure depends on several factors, such as the size of nanostructures and different electrical and mechanical boundary conditions [32]. For instance, under perfect short-circuit boundary conditions, a free-standing, cubic, finite $Pb(Zr_{0.4}Ti_{0.6})O_3$ nanodot, with a lateral size of 4.8 nm, exhibits a spontaneous polarization along one of its axes. However, under open-circuit conditions, the spontaneous polarization is suppressed by the large residual depolarization field inside the nanodot. In order to efficiently minimize the depolarization field, the dipoles are forced to rearrange themselves into a vortex structure. This vortex dipole structure results in a nonzero toroidal moment of polarization, rather than a net polarization, which can be used as an order parameter in potential memory nanodevices, enabling an ultrahigh storage density of

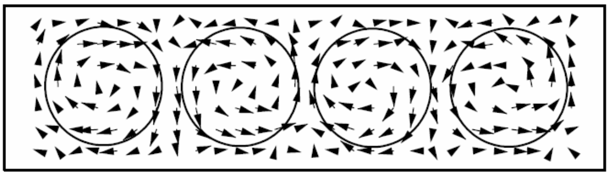

Figure 2.11: Local dipole pattern in a $Pb(Zr_{0.5}Ti_{0.5})O_3$ rod with a diameter of 2.8 nm and a length of 11.2 nm. The dipole vortices are schematically shown as circles. From [30].

60 Tb inch^{-2} [30]. Unlike the situation in ferroelectrics where the polarization states can be reversed by a static external electric field, the bistable toroidal states can be switched by applying a time-dependent magnetic field, B, which generates a curling electric field via $\nabla \times E = -\partial B/\partial t$. In addition, the existence of toroidal moments can be confirmed by measuring the electrostatic field, generated by the toroidal phase, using an atomic force microscope (AFM). Thus the AFM can also be employed to read the memory bits. The toroidally ordered structure may also be revealed by synchrotron x-ray diffraction (XRD) measurements [30].

2.4.3 Nanoislands

In chapter 2.3 we have considered the case in which a bulk ferroelectric sample is mechanically free to change its dimensions in response to an external electric field. However, if the sample is partially or fully clamped, for example, a thin film deposited on a thick substrate, the resulting piezoelectric deformation will be dependent on both the piezoelectric strain and the mechanical strain, as described by equation (2.12). In general, the nature of clamping of a thin film to a substrate is determined by many factors [36], such as film thickness [37]. For film thicknesses below a critical value, typically tens of nanometers, a thin film can be grown coherently onto a substrate and becomes fully clamped. Above the critical value, a film can be partially or fully relaxed by the formation of misfit dislocations at the film−substrate interface. For instance, for $Pb(Zr_{0.2}Ti_{0.8})O_3$ thin films grown on Nb-doped $SrTiO_3$ substrates, fully relaxed films were observed for thicknesses above typically 80 nm [38]. A completely clamped thin film is able to deform freely only in the direction perpendicular to the surface. The electromechanical displacement along the direction parallel to the surface, determined by the transverse piezoelectric coefficient d_{31}, is impeded due to the in-plane strain imposed on the film by the substrate. The measured

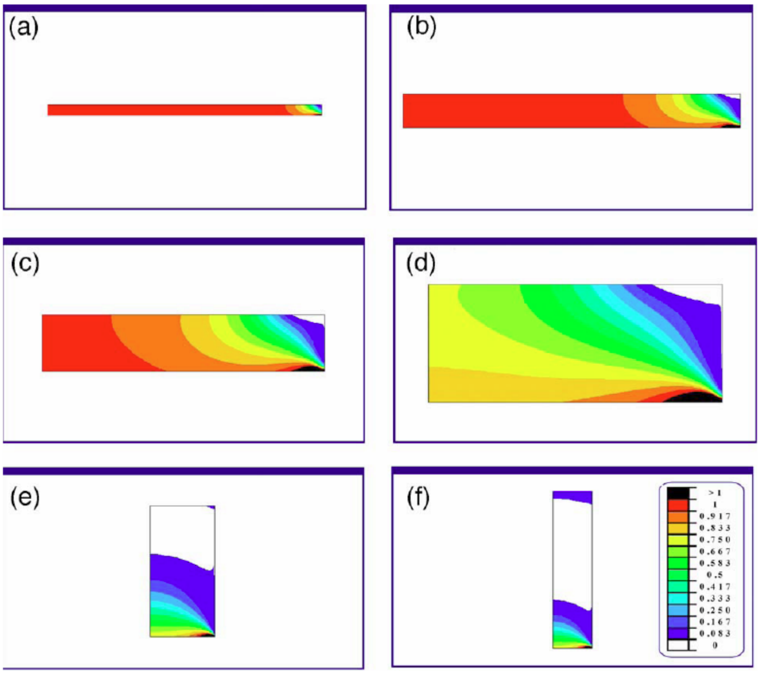

Figure 2.12: Finite element simulation results of in-plane strain states in epitaxial ferroelectric patterns with the aspect ratio of (a) 50, (b) 20, (c) 10, (d) 5, (e) 1, and (f) 0.5 at room temperature. The strain states are normalized with the value of in-plane strain of continuous thin films. From [41].

longitudinal piezoelectric coefficient of a clamped thin film, d_{33}^{f}, is related to the bulk coefficient, d_{33}, of a unclamped, monodomain, ferroelectric single-crystal, and can be written as [39]

$$d_{33}^{f} = d_{33} - \frac{2s_{13}}{s_{11} + s_{12}} d_{31} \qquad (2.15)$$

where s_{13}, s_{12}, and s_{11} are the elastic compliances of the film, determined under a constant electric field. Since d_{31}, s_{12}, and s_{13} are negative and s_{11} positive and larger than s_{12}, the measured coefficient in a clamped thin film always yields a lower value than that of a stress-free bulk sample due to the clamping effect. Recently, it has been verified experimentally [37] that the piezoelectric response of thin films increases with increasing film thickness, due to the decrease of substrate clamping for thicker films, in agreement with equation (2.15).

According to recent work by Nagarajan *et al.* [40], the measured piezoelectric coefficient for a patterned island structure with a fixed film thickness can also be expressed in terms of an effective in-plane stress, σ_{eff},

$$d_{33}^{\mathrm{measured}} = d_{33} - \frac{2s_{13}\sigma_{\mathrm{eff}}}{E_3} \tag{2.16}$$

Here, σ_{eff} is a measure of the degree of clamping and can be estimated from the following equation

$$\sigma_{\mathrm{eff}} = Y_f^0\, \chi_0\, e_{\mathrm{eff}} \tag{2.17}$$

where Y_f^0 is the generalized Young's modulus of the film, χ_0 is the geometry factor introduced to account for the lateral size of the ferroelectric island, and e_{eff} is the effective in-plane strain and is obtained from $e_{\mathrm{eff}} = d_{31}E_3$.

Furthermore, Lee *et al.* [41] have shown that the in-plane strain state in a patterned ferroelectric island structure depends on the aspect ratio, i.e., the lateral size over the thickness of the island. The evolution of the in-plane strain relaxation with the aspect ratio of the island is illustrated in figure 2.12. As can be seen, when the aspect ratio decreases, the degree of clamping drops drastically, starting in the regions close to the edges. As the aspect ratio reaches 5 or less (figures 2.12(d) – (f)), the in-plane strain in the entire upper part of the island is relaxed. In addition, results from the finite element simulations revealed that the average volumetric in-plane strain in patterned structures, with an aspect ratio below 20, is appreciably lower than that of the continuous film. Hence, when the in-plane strain is reduced, an enhancement of piezoelectric activity should be expected, according to equations (2.16) and (2.17).

References

[1] M. E. Lines and A. M. Glass. *Principles and Applications of Ferroelectrics and Related Materials.* Oxford: Clarendon Press, 1979.

[2] K. M. Rabe, M. Dawber, C. Lichtensteiger, C. H. Ahn, and J.-M. Triscone. Modern physics of ferroelectrics: Essential background. In K. M. Rabe, C. H. Ahn, and J.-M. Triscone, editor, *Physics of Ferroelectrics: A Modern Perspective*, volume 105 of *Topics in Applied Physics*, pages 1–30. Berlin Heidelberg: Springer-Verlag, 2007.

[3] C.-L. Jia, S.-B. Mi, K. Urban, I. Vrejoiu, M. Alexe, and D. Hesse. Atomic-scale study of electric dipoles near charged and uncharged domain walls in ferroelectric films. *Nat. Mater.*, 7:57, 2008.

[4] D. Damjanovic. Ferroelectric, dielectric and piezoelectric properties of ferroelectric thin films and ceramics. *Rep. Prog. Phys.*, 61:1267–1324, 1998.

[5] S. Ducharme, V. M. Fridkin, A. V. Bune, S. P. Palto, L. M. Blinov, N. N. Petukhova, and S. G. Yudin. Intrinsic ferroelectric coercive field. *Phys. Rev. Lett.*, 84:175, 2000.

[6] J. F. Nye. *Physical Properties of Crystals*, pages 110–130. Oxford: Clarendon Press, 1984.

[7] M. Alexe and A. Gruverman, editor. *Nanoscale Characterisation of Ferroelectric Materials: Scanning Probe Microscopy Approach.* Berlin Heidelberg: Springer-Verlag, 2004.

[8] G. Geneste, E. Bousquet, and P. Ghosez. New insight into the concept of ferroelectric correlation volume. *J. Comput. Theor. Nanosci.*, 5:517, 2008.

[9] D. R. Tilley and B. Žekš. Landau theory of phase transitions in thick films. *Solid State Commun.*, 49:823, 1984.

[10] W. L. Zhong, Y. G. Wang, P. L. Zhang, and B. D. Qu. Phenomenological study of the size effect on phase transition in ferroelectric particles. *Phys. Rev. B*, 50:698, 1994.

[11] Y. G. Wang, W. L. Zhong, and P. L. Zhang. Lateral size effects on cells in ferroelectric films. *Phys. Rev. B*, 51:17235, 1995.

[12] C. L. Wang and S. R. P. Smith. Landau theory of the size-driven phase transition in ferroelectrics. *J. Phys.: Condens. Matter*, 7:7163, 1995.

[13] S. Li, J. A. Eastman, Z. Li, C. M. Foster, R. E. Newnham, and L. E. Cross. Size effects in nanostructured ferroelectrics. *Phys. Lett. A*, 212:341, 1996.

[14] S. Li, J. A. Eastman, J. M. Vetrone, C. M. Foster, R. E. Newnham, and L. E. Cross. Dimension and size effects in ferroelectrics. *Jpn. J. Appl. Phys.*, 36:5169, 1997.

[15] W. L. Zhong, B. D. Qu, P. L. Zhang, and Y. G. Wang. Thickness dependence of the dielectric susceptibility of ferroelectric thin films. *Phys. Rev. B*, 50:12375, 1994.

[16] W. L. Zhong, Y. G. Wang, and P. L. Zhang. Size effects on phase transitions in ferroelectric films. *Phys. Lett. A*, 189:121, 1994.

[17] A. G. Zembilgotov, N. A. Pertsev, H. Kohlstedt, and R. Waser. Ultrathin epitaxial ferroelectric films grown on compressive substrates: Competition between the surface and strain effects. *J. Appl. Phys.*, 91:2247, 2002.

[18] P. Ghosez and J. Junquera. First-Principles Modeling of Ferroelectric Oxides Nanostructures. In M. Rieth and W. Schommers, editor, *Handbook of Theoretical and Computational Nanotechnology*, volume 4. Stevenson Ranch: American Scientic Publisher, 2006.

[19] P. Ghosez and K. M. Rabe. Microscopic model of ferroelectricity in stress-free $PbTiO_3$ ultrathin films. *Appl. Phys. Lett.*, 76:2767, 2000.

[20] B. Meyer and D. Vanderbilt. *Ab initio* study of $BaTiO_3$ and $PbTiO_3$ surfaces in external electric fields. *Phys. Rev. B*, 63:205426, 2001.

[21] S. Tinte and M. G. Stachiotti. Surface effects and ferroelectric phase transitions in $BaTiO_3$ ultrathin films. *Phys. Rev. B*, 64:235403, 2001.

[22] J. Junquera and P. Ghosez. Critical thickness for ferroelectricity in perovskite ultrathin films. *Nature*, 422:506, 2003.

[23] E. Almahmoud, Y. Navtsenya, I. Kornev, H. Fu, and L. Bellaiche. Properties of $Pb(Zr,Ti)O_3$ ultrathin films under stress-free and open-circuit electrical boundary conditions. *Phys. Rev. B*, 70:220102, 2004.

[24] N. Sai, A. M. Kolpak, and A. M. Rappe. Ferroelectricity in ultrathin perovskite films. *Phys. Rev. B*, 72:020101, 2005.

[25] M. Stengel, D. Vanderbilt, and N. A. Spaldin. Enhancement of ferroelectricity at metal−oxide interfaces. *Nat. Mater.*, 8:392, 2009.

[26] J. Hong and D. Fang. Size-dependent ferroelectric behaviors of $BaTiO_3$ nanowires. *Appl. Phys. Lett.*, 92:012906, 2008.

[27] J. Hong and D. Fang. Systematic study of the ferroelectric properties of $Pb(Zr_{0.5}Ti_{0.5})O_3$ nanowires. *J. Appl. Phys.*, 104:064118, 2008.

[28] J. Wang, M. Kamlah, T.-Y. Zhang, Y. Li, and L.-Q. Chen. Size-dependent polarization distribution in ferroelectric nanostructures: Phase field simulations. *Appl. Phys. Lett.*, 92:162905, 2008.

[29] H. Fu and L. Bellaiche. Ferroelectricity in barium titanate quantum dots and wires. *Phys. Rev. Lett.*, 91:257601, 2003.

[30] I. I. Naumov, L. Bellaiche, and H. Fu. Unusual phase transitions in ferroelectric nanodisks and nanorods. *Nature*, 432:737, 2004.

[31] I. I. Naumov and H. Fu. Spontaneous polarization in one-dimensional $Pb(Zr,Ti)O_3$ nanowires. *Phys. Rev. Lett.*, 95:247602, 2005.

[32] I. Ponomareva, I. I. Naumov, and L. Bellaiche. Low-dimensional ferroelectrics under different electrical and mechanical boundary conditions: Atomistic simulations. *Phys. Rev. B*, 72:214118, 2005.

[33] G. Geneste, E. Bousquet, J. Junquera, and P. Ghosez. Finite-size effects in $PbTiO_3$ nanowires. *Appl. Phys. Lett.*, 88:112906, 2006.

[34] I. Naumov and A. M. Bratkovsky. Unusual polarization patterns in flat epitaxial ferroelectric nanoparticles. *Phys. Rev. Lett.*, 101:107601, 2008.

[35] S. Prosandeev, I. Ponomareva, I. Naumov, I. Kornev, and L. Bellaiche. Original properties of dipole vortices in zero-dimensional ferroelectrics. *J. Phys.: Condens. Matter*, 20:193201, 2008.

[36] D. G. Schlom, L.-.Q. Chen, C. B. Eom, K. M. Rabe, S. K. Streiffer, and J.-M. Triscone. Strain tuning of ferroelectric thin films. *Annu. Rev. Mater. Res.*, 37:589–626, 2007.

[37] D. M. Kim, C. B. Eom, V. Nagarajan, J. Ouyang, R. Ramesh, V. Vaithyanathan, and D. G. Schlom. Thickness dependence of structural and piezoelectric properties of epitaxial $Pb(Zr_{0.52}Ti_{0.48})O_3$ films on Si and $SrTiO_3$ substrates. *Appl. Phys. Lett.*, 88:142904, 2006.

[38] S. Gariglio, N. Stucki, J.-M. Triscone, and G. Triscone. Strain relaxation and critical temperature in epitaxial ferroelectric $Pb(Zr_{0.20}Ti_{0.80})O_3$ thin films. *Appl. Phys. Lett.*, 90:202905, 2007.

[39] K. Lefki and G. J. M. Dormans. Measurement of piezoelectric coefficients of ferroelectric thin films. *J. Appl. Phys.*, 76:1764, 1994.

[40] V. Nagarajan, A. L. Roytburd, A. Stanishevsky, S. Prasertchoung, T. Zhao, L. Chen, J. Melngailis, O. Auciello, and R. Ramesh. Dynamics of ferroelastic domains in ferroelectric thin films. *Nat. Mater.*, 2:43, 2003.

[41] K. Lee, H. Yi, W.-H. Park, Y. K. Kim, and S. Baik. Lateral size effects on domain structure in epitaxial $PbTiO_3$ thin films. *J. Appl. Phys.*, 100:051615, 2006.

Chapter 3

Nanoscale ferroelectrics

In this chapter a review of state-of-the-art fabrication techniques for achieving ferroelectric nanostructures is given. Some interesting experimental observations of ferroelectric size effects are mentioned.

3.1 Fabrication of ferroelectric nanostructures

In the last decade, there has been a constant pursuit for miniaturization of ferroelectric materials due to their potential utilization in nanoelectronic applications [1, 2, 3]. In general, downscaling can be achieved in three dimensions, i.e., both laterally and vertically, resulting in geometries such as thin films, nanoparticles, nanoislands, nanowires, and nanotubes, as shown in figure 3.1. A brief summary of some state-of-the-art fabrication techniques (see table 3.1) is presented below, with a focus on nanoislands, since this geometry is most interesting for the present study.

Ferroelectric nanostructures can be in principle produced by patterning a thin film into isolated islands using advanced top-down lithography techniques, such as focused ion beam (FIB) milling [4] and electron beam lithography (EBL) [5]. Alternatively, nanostructures can be achieved by novel bottom-up approaches based on self-assembly and self-patterning [6, 7], or by processing methods utilizing shadow/deposition masks [8, 9]. In general, the top-down approaches provide a highly precise positioning and size definition but have a limited lateral resolution. They are also prone to processing damage and are relatively time-consuming. The bottom-up routes offer structures with smaller feature size, but are hampered by poor registration and size control, and thus need special substrate patterning (i.e., prestructuring of templates) that usually involves top-down processing [3].

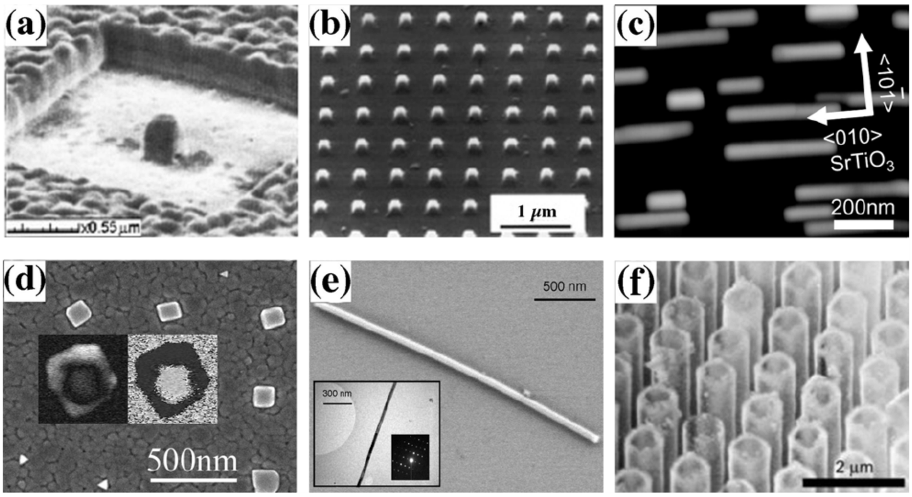

Figure 3.1: (a) Scanning ion beam image of a nanoscale Pb(Zr,Ti)O_3 capacitor fabricated by FIB milling [4]. (b) SEM image showing a Pb(Zr,Ti)O_3 cell array written by electron beam [5]. (c) AFM topographic image of self-assembled $PbTiO_3$ nanoislands on a Pt/$SrTiO_3$ substrate [6]. (d) Pb(Zr,Ti)O_3 crystallites grown on 150 nm wide TiO_2 seeds [7]. The inset shows PFM images of the amplitude and phase of one of the squares. (e) SEM image of an isolated $BaTiO_3$ nanowire [22]. (f) A micrograph of a free-standing array of $SrBi_2Ta_2O_9$ tubes with diameter of about 800 nm [25]. The figure is adapted from [3].

3.1.1 Top-down approaches

Ganpule *et al.* [4, 10] have employed the FIB patterning technique to produce nanoscale ferroelectric capacitors by milling out an isolated island from Pt-coated 120 nm thick polycrystalline $Pb(Nb_{0.04}Zr_{0.28}Ti_{0.68})O_3$ and 180 nm thick $SrBi_2Ta_2O_9$ films using a 50 kV focused beam of Ga ions. Capacitors (figure 3.1(a)) with lateral dimensions down to 70×70 nm^2 can be obtained by optimizing the processing procedure. The main advantage of this technique is the straightforward approach to define nanostructures without using any mask. The key challenges of FIB are slow processing, restriction to small areas, and implantation of Ga into the structure, which causes a permanently damaged dielectric layer [11]. The latter effect can be minimized by post-annealing in oxygen. Recently, damage-free $Pb(Zr_{0.3}Ti_{0.7})O_3$ nanostructures, ranging in size from 1 μm down to 250 nm, have been achieved when a 250 nm thick protective photo resist layer was used during FIB milling [12].

Table 3.1: Examples of state-of-the-art fabrication routes for achieving ferroelectric perovskite nanostructures.

Material	Processing	Lateral size (nm)	Ref.
Top-down approaches			
Pb(Nb,Zr,Ti)O_3	FIB	70	[4]
Pb(Zr,Ti)O_3	EBL	100	[13]
Pb(Zr,Ti)O_3	EBDW	100	[5]
Bottom-up approaches			
$PbTiO_3$	Self-patterning	20	[16]
Pb(Zr,Ti)O_3	Self-patterning	40	[14]
$PbTiO_3$	Template-based	50	[17]
Pb(Zr,Ti)O_3	Template-based	120	[7]
Alternative approaches			
Pb(Zr,Ti)O_3	Deposition mask	60	[9]
$BaTiO_3$	Nanosphere	200	[21]
Pb(Zr,Ti)O_3	Nanoimprint	300	[19]

Bühlmann *et al.* [13] have fabricated $Pb(Zr_{0.4}Ti_{0.6})O_3$ features with a lateral size ranging from 100 − 300 nm using the EBL technique. For the patterning process, a 150 nm thick polymethyl methacrylate (PMMA) resist layer was first written by an electron beam. A 75 nm thick Cr hard masking layer was subsequently evaporated onto the developed PMMA layer with holes of 50 − 200 nm in lateral size. After the lift-off process in acetone, reactive ion etching was employed to define ferroelectric patterns. By applying a low ion energy for the dry etching process, it was possible to achieve high-quality $Pb(Zr_{0.4}Ti_{0.6})O_3$ patterns.

The lithography methods mentioned above typically yield a low throughput. One promising way to increase the throughput is the application of electron beam direct writing (EBDW) [5]. In this approach, a metal-organic film deposited on a conductive substrate is exposed locally by an electron beam, and the desired pattern is impressed by scanning the electron beam over the sample. The pattern is subsequently developed by dissolving the unexposed areas. After developing, the remaining metal-organic mesas are transformed into ferroelectric oxide cells with well-defined shape and dimension by annealing and crystallization at high temperatures. Periodic patterns of 100×100 nm^2 cells of Pb(Zr,Ti)O_3 have been fabricated, as shown by the scanning electron microscopy (SEM) image in figure 3.1(b).

3.1.2 Bottom-up approaches

At present, top-down lithography approaches can generally provide ferroelectric nanostructures with lateral sizes down to $\sim$ 70 nm. In order to scale down below 50 nm, fabrication methods based on bottom-up approaches are preferred. Szafraniak *et al.* [14] used a self-patterning technique to produce $Pb(Zr_{0.52}Ti_{0.48})O_3$ nanoislands by exploiting the microstructural instability of ultrathin films when annealing at high temperatures. $Pb(Zr_{0.52}Ti_{0.48})O_3$ thin films were deposited onto Nb-doped $SrTiO_3$ substrates by a chemical solution. After annealing at 800 – 1100 °C for one hour in a lead oxide atmosphere, the as-deposited film breaks into islands with lateral sizes of 40 – 90 nm and a height of about 9 nm. The key challenge of this approach is that misfit dislocations can be formed at the film–substrate interface, which were found to drastically degrade the ferroelectric properties [15].

Using a similar approach, Roelofs and co-workers [16] have prepared $PbTiO_3$ nanograins on Pt-coated Si substrates by chemical solution deposition. An anhydrous lead acetate based precursor solution was spin-coated onto the substrate. After a rapid thermal annealing, single separated ferroelectric grains with sizes ranging from 20 – 200 nm were obtained.

Another approach is based on metal-organic chemical vapor deposition and terminating the deposition before dense films are formed. This technique has been used by Nonomura *et al.* [6] to synthesize self-assembled $PbTiO_3$ nanoislands on Pt-coated $SrTiO_3$ substrates. The islands had a lateral size and a height down to 40 and 4 nm, depending on the shape of the island. Figure 3.1(c) displays an AFM image of $PbTiO_3$ nanoislands prepared on a Pt/$SrTiO_3$ substrate.

Challenges related to self-patterning of ferroelectric nanostructures are poor registration due to the random distribution of the nucleation sites, and a resulting large size distribution. Regular and periodic pattern definition, which is required for individually addressing the nanoscale ferroelectric structures used in memory or any other devices, can be realized by performing the self-assembling process on a prestructured template [3].

Bühlmann *et al.* used a lithography-modulated self-assembly method to establish $Pb(Zr_{0.4}Ti_{0.6})O_3$ single crystallites on precisely predefined TiO_2 seeds by sputter deposition [7]. EBL followed by dry etching were used to pattern 100 – 200 nm wide nucleation sites in an epitaxial 2 nm thick rutile TiO_2 film, grown on epitaxial (111)-oriented Pt/$SrTiO_3$ substrate. During sputtering, the nucleation of $Pb(Zr_{0.4}Ti_{0.6})O_3$ crystallites takes place preferentially on these predefined TiO_2 seeds, which provide a locally enhanced chemical affinity for capturing PbO molecules and a lower nucleation activation energy due to Ti enrichment. As a result, nucleation outside the defined area was 60 times less likely. In addition, the as-fabricated perovskite crystallites had a narrow size distribution with lateral sizes in the range of 120 – 150 nm, as indicated in figure 3.1(d).

More recently, Clemens *et al.* [17] reported a similar template-based technique to arrange $PbTiO_3$ nanostructures on predefined TiO_2 seeds. In their work, the TiO_2 nucleation sites were directly evaporated on top of the developed, prestructured, PMMA resist mask layer. After the remaining resist was removed, a highly dilute $PbTiO_3$ precursor solution was spun onto the seeded substrate. Upon crystallization at 700 °C, $PbTiO_3$ grains with lateral sizes down to 50 nm were formed on the TiO_2 nucleation sites.

3.1.3 Alternative approaches

Recent developments of various lithography-based techniques and nanoscale shadow/deposition masks have triggered further progress in the fabrication of large-scale two-dimensional periodic arrays of ferroelectric nanostructures with a well-defined size. A promising technique is nanoimprint lithography [18]. This lithography technique is based on compression molding to create a thickness contrast pattern in a thin resist layer deposited on a substrate. During the imprint process, the thermoplastic resist undergoes a glass transition above a certain temperature and can be readily deformed into the shape of the mold. After the mold is removed, the pattern is transferred using anisotropic etching to remove the residue resist in the compressed areas. The pattern can be further transferred into the substrate using selective etching techniques. The key advantage of this manufacturing technology is the ability to pattern sub-100 nm structures over a large area with a high throughput and a low cost [3].

Harnagea *et al.* [19] have utilized nanoimprint lithography to fabricate arrays of ferroelectric $Pb(Zr,Ti)O_3$ cells with lateral sizes ranging from several μm down to 300 nm. The cell arrays were obtained by imprinting the precursor gel films, deposited on Nb-doped $SrTiO_3$ substrates by chemical solution deposition. Recently, Hu and co-workers [20] demonstrated that the nanoimprinting process can be used to produce regular arrays of highly ordered nanostructures of a ferroelectric polymer, with an integration density exceeding 33 Gb inch^{-2}.

A few research groups have attempted to prepare ferroelectric perovskite oxides using nanosphere lithography [21] and nanoscale shadow/deposition masks [8, 9]. For example, Lee *et al.* [9] have fabricated nanocapacitors of $Pt/Pb(Zr_{0.2}Ti_{0.8})O_3/Pt$, with a diameter of about 60 nm and a height of $20-40$ nm, through an ultrathin anodic aluminium oxide mask using pulsed laser deposition. An island density up to 180 Gb inch^{-2} was achieved.

3.1.4 Novel geometries

Much effort has also been made to synthesize one-dimensional ferroelectric nanostructures. Yun *et al.* [22] have fabricated $BaTiO_3$ nanowires using solution-phase decomposition of barium titanium isopropoxide. This synthesis yields separated single-crystalline $BaTiO_3$ nanowires with diameters ranging from 5 to 60 nm and lengths above 10 μm (figure 3.1(e)). Zhang and co-workers [23] have synthesized $Pb(Zr_{0.53}Ti_{0.47})O_3$ nanowires by immersing nanochannel alumina templates into a sol-gel precursor solution. After subsequent annealing, the templates were etched away, and free-standing polycrystalline nanowires with diameters of about 45 nm and lengths of 6 μm were obtained. Based on a template-free surfactant-assisted hydrothermal synthesis route, Rørvik *et al.* [24] have produced arrays of single-crystalline $PbTiO_3$ nanorods on a substrate. The nanorods had a square cross-section of $35 - 400$ nm and were up to 5 μm long.

Ferroelectric perovskite nanotubes have also attracted attention due to their potential utilization as nanofluidic devices in ink-jet printing and nanopositioners [3]. As an example, Morrison *et al.* [25] used a technique based on liquid source misted chemical deposition to fabricate a free-standing array of $SrBi_2Ta_2O_9$ tubes (figure 3.1(f)), with a diameter ranging from 4 μm down to $\sim$ 800 nm, a wall thickness less than 100 nm, and a length of $\sim$ 100 μm.

3.2 Experimental observations of size effects

3.2.1 Thin films

A large amount of progress has been recently achieved in the epitaxial growth of thin films of perovskite ferroelectrics using advanced deposition techniques, such as radio frequency (RF) magnetron sputter deposition, pulsed laser deposition, and metal-organic chemical vapor deposition, enabling fabrication of high-quality ultrathin films [26]. Experimental results from several groups suggest that ferroelectricity at room temperature can persist at a very small size. Bune *et al.* reported that for crystalline copolymer films, a ferroelectric phase persists down to a film thickness of 1 nm (two monolayers) [27]. Tybell *et al.* demonstrated a stable polarization perpendicular to the surface in high-quality $Pb(Zr_{0.2}Ti_{0.8})O_3$ thin films, grown epitaxially on metallic Nb-doped $SrTiO_3$ substrates by off-axis RF magnetron sputtering, down to thicknesses of 4 nm, and possibly even lower, using a combination of electrostatic force microscopy (EFM) and PFM [28]. Kim *et al.* [29] measured polarization versus electric field hysteresis loops in

$SrRuO_3/BaTiO_3/SrRuO_3$ capacitors, with a film thickness down to 5 nm, grown on $SrTiO_3$ substrates by pulsed laser deposition. Fong and co-workers [30, 31] showed that $PbTiO_3$ films with thicknesses down to 1.2 nm (3 unit cells), grown on $SrTiO_3$ substrates by metal-organic chemical vapor deposition, can sustain ferroelectricity, based on observations of periodic 180° oppositely polarized stripe domains. These findings imply that there is basically no fundamental thickness limit imposed on practical devices by an intrinsic ferroelectric size effect, in conformity with theoretical calculations discussed in chapter 2.4.1.

3.2.2 Nanoparticles

There have been several reports on the size effects of the ferroelectric properties of nanoparticles. Ishikawa *et al.* [32] reported that the transition temperature in ultrafine $PbTiO_3$ nanoparticles, determined by Raman scattering measurements, decreases from the bulk value when the average particles size was reduced from 52 nm down to 22 nm, as shown in figure 3.2. The average size was determined by XRD analysis using Scherrer equation. An extrapolated critical size, below which the ferroelectricity is lost, can be derived from the following empirical expression

$$T_c(d) = T_c^{\mathrm{bulk}} - \frac{C}{d - d_{\mathrm{crit}}} \tag{3.1}$$

where d is the particle size, C is a fitting parameter, and d_{crit} is the critical particle size at which $T_c = 0$ K. The solid curve in figure 3.2 is obtained with $T_c^{\mathrm{bulk}} = 500$ °C, $C = 588.5$ °C nm, and $d_{\mathrm{crit}} = 12.6$ nm. Zhong and co-workers [33] carried out both Raman scattering and specific-heat measurements on $PbTiO_3$ nanoparticles, and they estimated the critical size to be 9.3 nm. Jiang *et al.* [34] used high resolution transmission electron microscopy to study the crystal structure of $PbTiO_3$ particles. They reported that particles as small as 15 nm in diameter had a tetragonal structure, indicating a ferroelectric phase. For other perovskite-related systems, Yu *et al.* reported the size effect in $SrBi_2Ta_2O_9$ nanoparticles with a size ranging from 11 – 71 nm [35]. A critical size of 2.6 nm was obtained, following the empirical expression (3.1). Overall, these experimental results are in good agreement with theoretical predications from the GLD model for perovskite nanoparticles [36].

3.2.3 Nanowires

Ferroelectric size effects in nanowires are currently much less studied as compared to thin films and nanoparticles, presumably due to the limita-

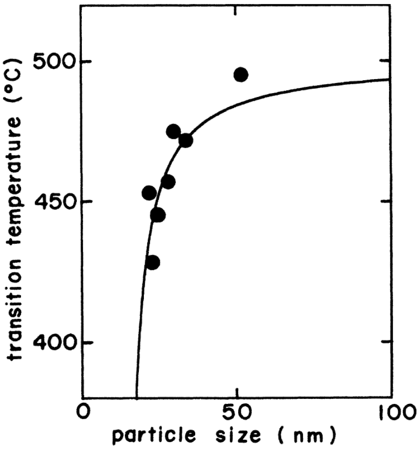

Figure 3.2: Transition temperature versus particle size for ultrafine $PbTiO_3$ particles. An extrapolated critical size of 12.6 nm is obtained by fitting the observed values (symbols) using equation (3.1), as shown by the solid curve. From [32].

tions and difficulties of producing one-dimensional nanostructures with a controllable size definition [37]. In a recent study, Spanier *et al.* [38] have performed variable-temperature EFM measurements to study the dependence of transition temperature on the nanowire size for single-crystalline $BaTiO_3$ nanowires, with a diameter ranging from 3 to 100 nm and a length up to and above 10 μm. The transition temperature was suppressed as the nanowire diameter decreases. The smallest diameter at which a remanent polarization, oriented perpendicularly to the nanowire axis, can be measured at room temperature was $\sim$ 3 nm. Extrapolation of the experimental data indicates that nanowires of 0.8 nm in diameter can support ferroelectricity at lower temperatures, in agreement with the first-principles calculations outlined in chapter 2.4.2.

3.2.4 Nanoislands

As mentioned in chapter 2.4.3, the piezoelectric response of nanostructured ferroelectrics is expected to be enhanced as their lateral sizes are scaled down, due to the decrease of in-plane strain. Recently, such piezoelectric behavior has been verified experimentally in ferroelectric perovskite nanostructures [13, 39, 40]. For instance, Bühlmann *et al.* [13] have performed PFM measurements on $Pb(Zr_{0.4}Ti_{0.6})O_3$ patterns, and they observed a prominent increase in piezoelectric response when the lateral size of the patterns was

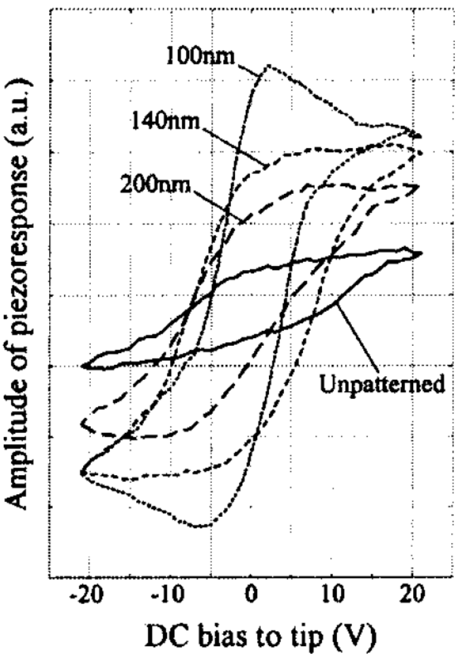

Figure 3.3: Piezoelectric hysteresis loops of $Pb(Zr_{0.4}Ti_{0.6})O_3$ patterns revealing enhanced piezoelectric activity as the lateral size was reduced from 200 nm down to 100 nm. From [13].

reduced from 200 nm down to 100 nm, as can be seen from figure 3.3. Also, the measured piezoresponse of the patterns was appreciably higher than that of the continuous unpatterned film.

3.2.5 Domain structure in nanoscale ferroelectrics

Recently, a ferroelectric monodomain to polydomain transition has been reported by Nagarajan *et al.* [41] and Lichtensteiger *et al.* [42] for epitaxial ultrathin films of $Pb(Zr_{0.2}Ti_{0.8})O_3$ and $PbTiO_3$, respectively. For example, in the latter study, high-resolution XRD measurements were used to study the evolution of the film tetragonality, c/a, for $2.8 - 48$ nm thick $PbTiO_3$ films, with $La_{0.67}Sr_{0.33}MnO_3$ bottom electrodes grown on $SrTiO_3$ substrates. It was found that the tetragonality was reduced with decreasing film thickness. However, a striking recovery of the tetragonality was observed for the thinnest films with thicknesses below ~ 12 nm. PFM measurements showed that this recovery was accompanied by a transition from monodomain to polydomain structure. The findings were interpreted as a result of an increasing depolarization field as the film thickness was reduced, for which a polydomain ground state was produced to minimize the electrostatic energy associated with the large depolarization field for the thinnest films.

For laterally confined ferroelectric nanostructures, the domain structure was found to be dependent on the lateral size for single separated $PbTiO_3$ grains, fabricated on $Pt/TiO_2/SiO_2/Si$ substrates by chemical solution deposition [16]. It was shown that the nanograins often had two domains with 180° domain walls for a size in the range of $40-50$ nm, whereas the grains became monodomain for grain sizes smaller than 40 nm.

Although vortex states in soft ferromagnetic nanostructures have been previously detected [43, 44], no such direct experimental observations have been made to date on nanoscale ferroelectrics. Recently, Gruverman *et al.* [45] and Rodriguez *et al.* [46] have attempted to probe the vortex domain configuration (figure 2.11) in ferroelectric perovskites. Most notably in the latter, vertical and lateral PFM were combined to visualize the domain structure in $Pb(Zr_{0.4}Ti_{0.6})O_3$ nanodots, with a diameter of 50 nm and a height of 20 nm, deposited on $SrRuO_3/SrTiO_3$ substrates through an anodic aluminium oxide stencil mask using pulsed laser deposition. It was seen that some of the nanodots exhibited a domain structure similar to the intermediate vortex domain state, in which a toroidal moment and an out-of-plane polarization may coexist, according to theoretical calculations [47]. The observation of such unusual domain structures were interpreted, with the aid of a theoretical model, as an indication for the presence of vortex polarization states.

References

[1] M. Dawber, K. M. Rabe, and J. F. Scott. Physics of thin-film ferroelectric oxides. *Rev. Mod. Phys.*, 77:1083–1130, 2005.

[2] A. Rüdiger, T. Schneller, A. Roelofs, S. Tiedke, T. Schmitz, and R. Waser. Nanosize ferroelectric oxides – tracking down the superparaelectric limit. *Appl. Phys. A*, 80:1247, 2005.

[3] A. Gruverman and A. Kholkin. Nanoscale ferroelectrics: processing, characterization and future trends. *Rep. Prog. Phys.*, 69:2443–2474, 2006.

[4] C. S. Ganpule, A. Stanishevsky, S. Aggarwal, J. Melngailis, E. Williams, R. Ramesh, V. Joshi, and C. Paz de Araujo. Scaling of ferroelectric and piezoelectric properties in Pt/$SrBi_2Ta_2O_9$/Pt thin films. *Appl. Phys. Lett.*, 75:3874, 1999.

[5] M. Alexe, C. Harnagea, D. Hesse, and U. Gösele. Patterning and switching of nanosize ferroelectric memory cells. *Appl. Phys. Lett.*, 75:1793, 1999.

[6] H. Nonomura, M. Nagata, H. Fujisawa, M. Shimizu, H. Niu, and K. Honda. Structural control of self-assembled $PbTiO_3$ nanoislands fabricated by metalorganic chemical vapor deposition. *Appl. Phys. Lett.*, 86:163106, 2005.

[7] S. Bühlmann, P. Muralt, and S. Von Allmen. Lithography-modulated self-assembly of small ferroelectric $Pb(Zr,Ti)O_3$ single crystals. *Appl. Phys. Lett.*, 84:2614, 2004.

[8] H.-J. Shin, J. H. Choi, H. J. Yang, Y. D. Park, Y. Kuk, and C.-J. Kang. Patterning of ferroelectric nanodot arrays using a silicon nitride shadow mask. *Appl. Phys. Lett.*, 87:113114, 2005.

[9] W. Lee, H. Han, A. Lotnyk, M. A. Schubert, S. Senz, M. Alexe, D. Hesse, S. Baik, and U. Gösele. Individually addressable epitaxial ferroelectric nanocapacitor arrays with near Tb inch^{-2} density. *Nat. Nanotechnol.*, 3:402, 2008.

[10] C. S. Ganpule, A. Stanishevsky, Q. Su, S. Aggarwal, J. Melngailis, E. Williams, and R. Ramesh. Scaling of ferroelectric properties in thin films. *Appl. Phys. Lett*, 75:409, 1999.

[11] A. Stanishevsky, B. Nagaraj, J. Melngailis, R. Ramesh, L. Khriachtchev, E. McDaniel. Radiation damage and its recovery in focused ion beam fabricated ferroelectric capacitors. *J. Appl. Phys.*, 92:3275, 2002.

[12] M. Hambe, S. Wicks, J. M. Gregg, and V. Nagarajan. Creation of damage-free ferroelectric nanostructures via focused ion beam milling. *Nanotechnology*, 19:175302, 2008.

[13] S. Bühlmann, B. Dwir, J. Baborowski, and P. Muralt. Size effect in mesoscopic epitaxial ferroelectric structures: Increase of piezoelectric response with decreasing feature size. *Appl. Phys. Lett.*, 80:3195, 2002.

[14] I. Szafraniak, C. Harnagea, R. Scholz, S. Bhattacharyya, D. Hesse, and M. Alexe. Ferroelectric epitaxial nanocrystals obtained by a self-patterning method. *Appl. Phys. Lett.*, 83:2211, 2003.

[15] M.-W. Chu, I. Szafraniak, R. Scholz, C. Harnagea, D. Hesse, M. Alexe, and U. Gösele. Impact of misfit dislocations on the polarization instability of epitaxial nanostructured ferroelectric perovskites. *Nat. Mater.*, 3:87, 2004.

[16] A. Roelofs, T. Schneller, K. Szot, and R. Waser. Piezoresponse force microscopy of lead titanate nanograins possibly reaching the limit of ferroelectricity. *Appl. Phys. Lett.*, 81:5231, 2002.

[17] S. Clemens, T. Schneller, A. van der Hart, F. Peter, and R. Waser. Registered deposition of nanoscale ferroelectric grains by template-controlled growth. *Adv. Mater.*, 17:1357, 2005.

[18] S. Y. Chou, P. R. Krauss, and P. J. Renstrom. Nanoimprint lithography. *J. Vac. Sci. Technol. B*, 14:4129, 1996.

[19] C. Harnagea, M. Alexe, J. Schilling, J. Choi, R. B. Wehrspohn, D. Hesse, and U. Gösele. Mesoscopic ferroelectric cell arrays prepared by imprint lithography. *Appl. Phys. Lett.*, 83:1827, 2003.

[20] Z. Hu, M. Tian, B. Nysten, and A. M. Jonas. Regular arrays of highly ordered ferroelectric polymer nanostructures for non-volatile low-voltage memories. *Nat. Mater.*, 8:62, 2009.

[21] W. Ma, C. Harnagea, D. Hesse, and U. Gösele. Well-ordered arrays of pyramid-shaped ferroelectric $BaTiO_3$ nanostructures. *Appl. Phys. Lett.*, 83:3770, 2003.

[22] W. S. Yun, J. J. Urban, Q. Gu, and H. Park. Ferroelectric properties of individual barium titanate nanowires investigated by scanned probe microscopy. *Nano Lett.*, 2:447, 2002.

[23] X. Y. Zhang, X. Zhao, C. W. Lai, J. Wang, X. G. Tang, and J. Y. Dai. Synthesis and piezoresponse of highly ordered $Pb(Zr_{0.53}Ti_{0.47})O_3$ nanowire arrays. *Appl. Phys. Lett.*, 85:4190, 2004.

[24] P. M. Rørvik, Å. Almli, A. T. J. van Helvoort, R. Holmestad, T. Tybell, T. Grande, and M.-A. Einarsrud. $PbTiO_3$ nanorod arrays grown by self-assembly of nanocrystals. *Nanotechnology*, 19:225605, 2008.

[25] F. D. Morrison, L. Ramsay, and J. F. Scott. High aspect ratio piezoelectric strontium−bismuth−tantalate nanotubes. *J. Phys.: Condens. Matter*, 15:527, 2003.

[26] A.-B. Posadas, M. Lippmaa, F. J. Walker, M. Dawber, C. H. Ahn, and J.-M. Triscone. Growth and novel applications of epitaxial oxide thin films. In K. M. Rabe, C. H. Ahn, and J.-M. Triscone, editor, *Physics of Ferroelectrics: A Modern Perspective*, volume 105 of *Topics in Applied Physics*, pages 219–304. Berlin Heidelberg: Springer-Verlag, 2007.

[27] A. V. Bune, V. M. Fridkin, S. Ducharme, L. M. Blinov, S. P. Palto, A. V. Sorokin, S. G. Yudin, and A. Zlatkin. Two-dimensional ferroelectric films. *Nature*, 391:874, 1998.

[28] T. Tybell, C. H. Ahn, and J.-M. Triscone. Ferroelectricity in thin perovskite films. *Appl. Phys. Lett.*, 75:856, 1999.

[29] Y. S. Kim, D. H. Kim, J. D. Kim, Y. J. Chang, T. W. Noh, J. H. Kong, K. Char, Y. D. Park, S. D. Bu, J.-G. Yoon, and J.-S. Chung. Critical thickness of ultrathin ferroelectric $BaTiO_3$ films. *Appl. Phys. Lett.*, 86:102907, 2005.

[30] D. D. Fong, G. B. Stephenson, S. K. Streiffer, J. A. Eastman, O. Auciello, P. H. Fuoss, C. Thompson. Ferroelectricity in ultrathin perovskite films. *Science*, 304:1650, 2004.

[31] S. K. Streiffer, J. A. Eastman, D. D. Fong, C. Thompson, A. Munkholm, M. V. Ramana Murty, O. Auciello, G. R. Bai, and G. B. Stephenson. Observation of nanoscale 180° stripe domains in ferroelectric $PbTiO_3$ thin films. *Phys. Rev. Lett.*, 89:067601, 2002.

[32] K. Ishikawa, K. Yoshikawa, and N. Okada. Size effect on the ferroelectric phase transition in $PbTiO_3$ ultrafine particles. *Phys. Rev. B*, 37:5852, 1988.

[33] W. L. Zhong, B. Jiang, P. L. Zhang, J. M. Ma, H. M. Cheng, Z. H. Yang, and L. X. Li. Phase transition in $PbTiO_3$ ultrafine particles of different sizes. *J. Phys.: Condens. Matter*, 5:2619, 1993.

[34] B. Jiang, J. L. Peng, L. A. Bursill, and W. L. Zhong. Size effects on ferroelectricity of ultrafine particles of $PbTiO_3$. *J. Appl. Phys.*, 87:3462, 2000.

[35] T. Yu, Z. X. Shen, W. S. Toh, J. M. Xue, and J. Wang. Size effect on the ferroelectric phase transition in $SrBi_2Ta_2O_9$ nanoparticles. *J. Appl. Phys.*, 94:618, 2003.

[36] W. L. Zhong, Y. G. Wang, P. L. Zhang, and B. D. Qu. Phenomenological study of the size effect on phase transition in ferroelectric particles. *Phys. Rev. B*, 50:698, 1994.

[37] P. M. Rørvik. *Synthesis of ferroelectric nanostructures.* PhD thesis, Norwegian University of Science and Technology, 2008.

[38] J. E. Spanier, A. M. Kolpak, J. J. Urban, I. Grinberg, L. Ouyang, W. S. Yun, A. M. Rappe, and H. Park. Ferroelectric phase transition in individual single-crystalline $BaTiO_3$ nanowires. *Nano Lett.*, 6:735, 2006.

[39] V. Nagarajan, A. L. Roytburd, A. Stanishevsky, S. Prasertchoung, T. Zhao, L. Chen, J. Melngailis, O. Auciello, and R. Ramesh. Dynamics of ferroelastic domains in ferroelectric thin films. *Nat. Mater.*, 2:43, 2003.

[40] A. L. Roytburd, S. P. Alpay, V. Nagarajan, C. S. Ganpule, S. Aggarwal, E. D. Williams, and R. Ramesh. Measurements of internal stresses via the polarization in epitaxial ferroelectric films. *Phys. Rev. Lett.*, 85:190, 2000.

[41] V. Nagarajan, J. Junquera, J. Q. He, C. L. Jia, R. Waser, K. Lee, Y. K. Kim, S. Baik, T. Zhao, R. Ramesh, P. Ghosez, and K. M. Rabe. Scaling of structure and electrical properties in ultrathin epitaxial ferroelectric heterostructures. *J. Appl. Phys.*, 100:051609, 2006.

[42] C. Lichtensteiger, M. Dawber, N. Stucki, J.-M. Triscone, J. Hoffman, J.-B. Yau, C. H. Ahn, L. Despont, and P. Aebi. Monodomain to polydomain transition in ferroelectric $PbTiO_3$ thin films with $La_{0.67}Sr_{0.33}MnO_3$ electrodes. *Appl. Phys. Lett.*, 90:052907, 2007.

[43] T. Shinjo, T. Okuno, R. Hassdorf, K. Shigeto, and T. Ono. Magnetic vortex core observation in circular dots of permalloy. *Science*, 289:930, 2000.

[44] A. Wachowiak, J. Wiebe, M. Bode, O. Pietzsch, M. Morgenstern, and R. Wiesendanger. Direct observation of internal spin structure of magnetic vortex cores. *Science*, 298:577, 2002.

[45] A. Gruverman, D. Wu, H.-J. Fan, I. Vrejoiu, M. Alexe, R. J. Harrison, and J. F. Scott. Vortex ferroelectric domains. *J. Phys.: Condens. Matter*, 20:342201, 2008.

[46] B. J. Rodriguez, X. S. Gao, L. F. Liu, W. Lee, I. I. Naumov, A. M. Bratkovsky, D. Hesse, and M. Alexe. Vortex polarization states in nanoscale ferroelectric arrays. *Nano Lett.*, 9:1127, 2009.

[47] I. Naumov and A. M. Bratkovsky. Unusual polarization patterns in flat epitaxial ferroelectric nanoparticles. *Phys. Rev. Lett.*, 101:107601, 2008.

Chapter 4

Experimental

4.1 The material system

The material system, used in the present study, consists of $SrTiO_3$ (substrate) and $PbTiO_3$ (ferroelectric material), with an interposed thin film layer of $SrRuO_3$, which serves both as a template material and a bottom electrode. In figure 4.1 the room-temperature unit cell structures of $SrTiO_3$ and $PbTiO_3$ are schematically illustrated.

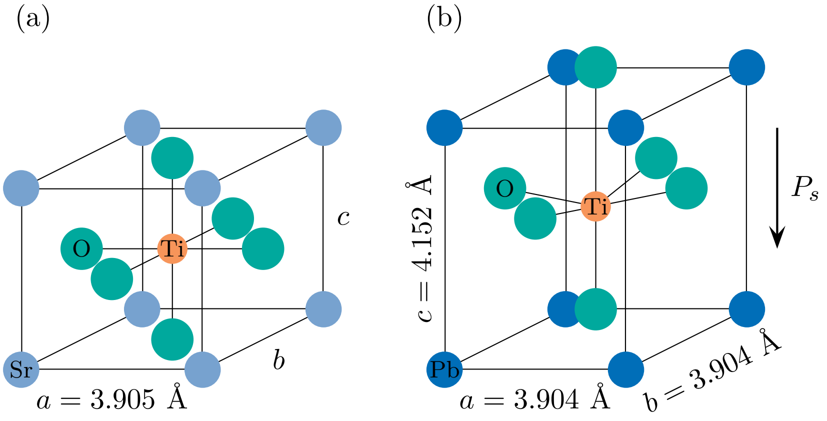

Figure 4.1: (a) The cubic unit cell structure of $SrTiO_3$ substrate with lattice parameters $a = b = c = 3.905$ Å. (b) The room-temperature tetragonal unit cell structure of $PbTiO_3$ with bulk lattice parameters $a = b = 3.904$ Å and $c = 4.152$ Å. Also shown is the spontaneous polarization arising from atomic displacements.

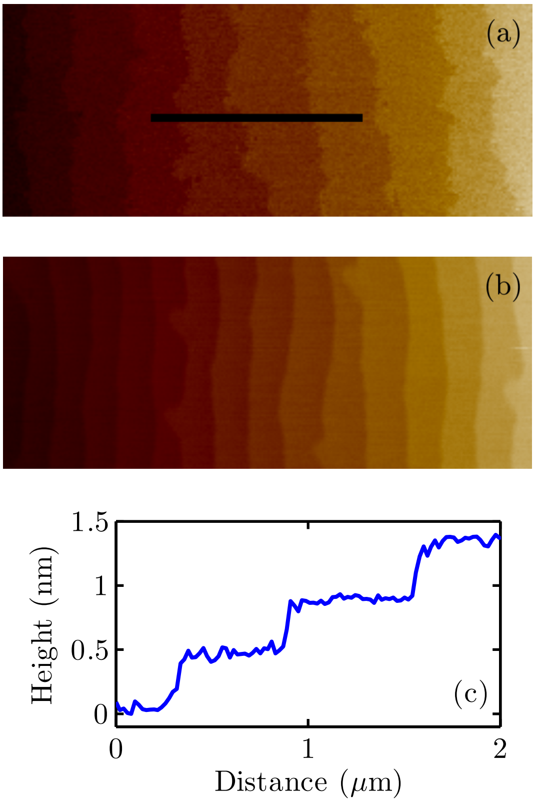

Figure 4.2: AFM topography images ($5 \times 2\ \mu m^2$) of $SrTiO_3$ substrates taken before (a) and after (b) annealing. (c) Cross-sectional profile corresponding to the marker line in (a).

4.1.1 $SrTiO_3$

$SrTiO_3$ is an insulating and paraelectric perovskite at room temperature with its free energy being minimum for zero polarization. However, it has been recently reported that room-temperature ferroelectricity can be induced in strained $SrTiO_3$ [1]. $SrTiO_3$ has a cubic unit cell, with lattice parameters $a = b = c = 3.905$ Å [2], as sketched in figure 4.1(a).

In the present work, (001)-oriented single-crystalline $SrTiO_3$ substrates, with a TiO_2-terminated surface layer [3, 4] and a miscut angle of less than 0.1°, were used. The as-received substrates had a smooth step and terrace surface structure (figure 4.2(a)), with the step height being typically one unit cell thick, as indicated by the cross-sectional profile in figure 4.2(c). Prior to any film deposition, the substrates were annealed in an oxygen gas flow for one hour at high temperatures[1], usually in the range of $\sim 950-1050$ °C, in order to obtain a better defined surface morphology with straighter step ledges, as can be seen by comparing the AFM (chapter 4.2.3) images taken before and after the annealing process in figure 4.2.

4.1.2 $PbTiO_3$

At room temperature, $PbTiO_3$ is a ferroelectric perovskite with a tetragonal unit cell structure (figure 4.1(b)), with bulk lattice parameters a and b being 3.904 Å, and $c = 4.152$ Å [2]. It undergoes a structural phase transition to the cubic and paraelectric phase at 493 °C, with $a = b = c = 3.96$ Å [5]. In the tetragonal phase, the oxygen (O) anions in the octahedral cage and the Ti cation are shifted in the same direction relative to the Pb cations at the cube corners [6], resulting in a nonzero spontaneous polarization[2], P_s. Since the mismatch between the in-plane lattice parameters of $PbTiO_3$ and $SrTiO_3$ is rather small, a relatively thick film of $PbTiO_3$ can be grown coherently on $SrTiO_3$ substrate, with the resulting polarization pointing along the out-of-plane c-axis direction. Electronic-structure calculations [7] have previously demonstrated that the hybridization between the Ti $3d$ states and the O $2p$ states is essential to weaken the short-range dipolar forces and allow the ferroelectric transition in $PbTiO_3$. In addition, it has been shown that the Pb $6s$ and O $2p$ states are also strongly hybridized, leading to a large strain[3] which stabilizes the tetragonal phase.

4.1.3 $SrRuO_3$

$SrRuO_3$ is a metallic perovskite oxide with an orthorhombic crystal structure with a slightly distorted RuO_6 octahedron [8]. The lattice parameters are $a = 5.53$ Å, $b = 5.57$ Å, and $c = 7.85$ Å. The unit cell structure can be viewed as pseudo-cubic with $a = b = c = 3.93$ Å, with a lattice distortion of 89.6°. The in-plane lattice of $SrRuO_3$ and $SrTiO_3$ is closely matched, permitting growth of relatively thick epitaxial and coherent films [9]. $SrRuO_3$ thin films with a step and terrace surface structure can be grown on $SrTiO_3$ substrates. Since this material is metallic, chemically inert in air [10], and well-lattice-matched to many ferroelectric perovskites, such as $PbTiO_3$, it

---

[1] Note that high-temperature annealing can also remove residue PMMA resist from the surface of $SrTiO_3$ substrate, as indicated by the AFM image in figure 4.2(b). Refer to Paper II for further details.

[2] The polarization can be as large as 75 $\mu C/cm^2$ [6].

[3] $PbTiO_3$ has a large 6% c/a strain. Typical ferroelectrics show strains of $0.5-3\%$ [7].

is particularly useful as a template material, in addition to the typical use as a bottom electrode.

4.2 Thin film growth and characterization

4.2.1 Sputter deposition

The thin film samples of $PbTiO_3$ and $SrRuO_3$ were grown on $SrTiO_3$ substrates using an off-axis RF magnetron sputtering technique [11, 12]. Typical deposition parameters are given in table 4.1. In the sputtering process, atoms are ejected from the surface of a target by bombardment with a flux of highly energetic particles. For the growth of $PbTiO_3$ thin films, a composite $PbTiO_3$ target with 10% excess lead was used as the source material. The target is mounted on the cathode (sputtering gun), and the substrate is positioned 90° with respect to the target, as illustrated in figure 4.3. The main advantage of the off-axis geometry is that resputtering of the film/substrate is reduced, so that smooth films can be produced at the expense of a lower deposition rate. Before film growth, a mixture of Ar and O gases is allowed to flow into the vacuum chamber. An alternating electric field, generated by a RF (13.56 MHz) power supply, is then applied between the cathode and the anode (usually grounded to the vacuum chamber), ionizing the Ar gas between the electrodes. The energetic and heavy Ar^+ ions are accelerated by the electric field towards the target, removing the atoms from the target

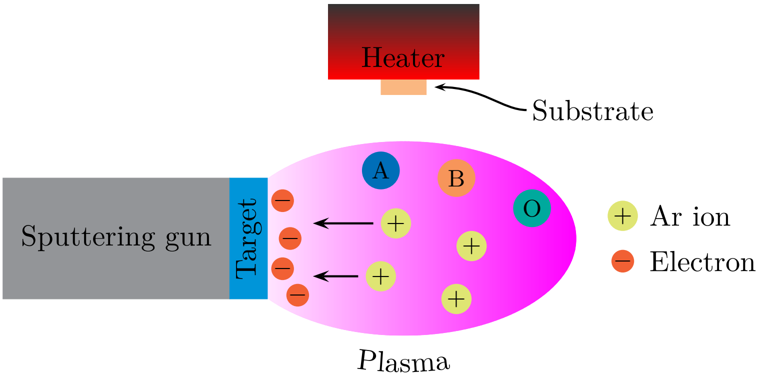

Figure 4.3: Schematic representation of thin film growth by sputter deposition in a 90° off-axis geometry. A high voltage is applied to generate a plasma. The highly energetic Ar ions will collide the target, thereby ejecting atoms from the target surface. Some of the atoms (A, B, and O) will finally arrive at the heated substrate and form a thin film.

surface upon collisions. Some of the ejected atoms are eventually collected onto a radiatively heated substrate and form a thin film. When the Ar ions collide with the target, secondary electrons are produced, which in turn ionize the Ar gas, leading to the creation of a self-sustained plasma. In order to increase the deposition rate, a magnetron is employed. A static magnetic field, parallel to the cathode surface, is generated by strong permanent magnets placed behind the target. The magnetic field and the electric field will confine the secondary electrons and make a very dense plasma in the region close to the cathode, thus increasing the sputtering rate.

Table 4.1: Growth parameters for $PbTiO_3$ and $SrRuO_3$ thin films on $SrTiO_3$ substrates. T_{sub} is temperature measured at the center of the substrate, using an optical pyrometer at a wavelength of 1.5 μm with the emissivity set at 0.7. The ratio of oxygen and argon gas is $O_2 : Ar = 4 : 10$.

Material	T_{sub} (°C)	Gas pressure (mTorr)	RF power (W)
$PbTiO_3$	500 – 530	165	90
$SrRuO_3$	590 – 690	100	100

4.2.2 X-ray diffraction

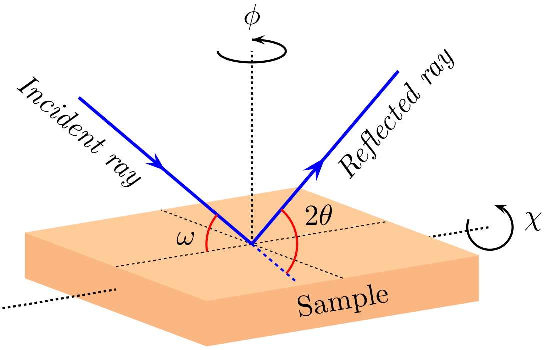

Figure 4.4: Sketch of a four-circle x-ray diffractometer with the four angles: ω, 2θ, ϕ, and χ.

A four-circle Bruker D8 Discover x-ray diffractometer was used to investigate the crystalline properties of samples. Figure 4.4 shows the four angles, ω, 2θ, ϕ, and χ, available for sample characterization. Three types

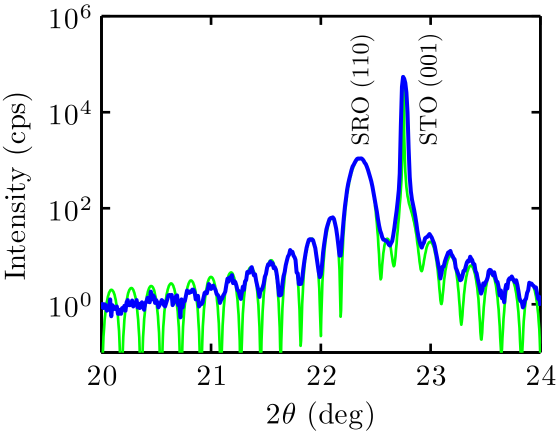

Figure 4.5: $\theta - 2\theta$ diffractogram of the $SrRuO_3$ (SRO) (110) reflection for a 50 nm thick film, grown on a $SrTiO_3$ (STO) substrate. The additional satellite peaks (thickness fringes) permit the film thickness to be precisely measured, as indicated by the green fine curve.

of measurements were carried out:

- $\theta - 2\theta$ scans
- Rocking curves (ω-scans)
- ϕ-scans

$\theta - 2\theta$ scans permit the spacing, d_{hkl}, between adjacent (hkl) lattice planes to be precisely measured by using the Bragg's law:

$$d_{hkl} = \frac{n\lambda}{2\sin\theta} \tag{4.1}$$

where h, k, and l are the Miller indices, n is the order of the diffraction, and $\lambda = 1.5406$ Å is the x-ray wavelength. Furthermore, due to the finite thickness size effect, the number of total diffracting planes in a sample (i.e., the sample thickness) can be determined by analyzing intensity oscillations (thickness fringes) close to the main diffraction peak, as can be seen from figure 4.5 for a 50 nm thick $SrRuO_3$ film grown on $SrTiO_3$.

Rocking curves are used to measure the mosaic spread of a sample, and the full width at half maximum (FWHM) value of the rocking curve peak gives information about the crystalline quality of the sample. Typical FWHM values in degrees of the $SrTiO_3$ (001), $SrRuO_3$ (110), and $PbTiO_3$

(001) reflections are 0.01 – 0.02, 0.02 – 0.03, and 0.02 – 0.03, respectively, indicative of good crystalline quality. Another use of rocking curves is to correct the sample misalignment, in order to maximize the intensity from the reflection peaks for $\theta - 2\theta$ scans.

ϕ-scans of the $PbTiO_3$ (101), $SrRuO_3$ (112), and $SrTiO_3$ (101) reflections have been carried out to check whether or not $PbTiO_3$ and $SrRuO_3$ thin films were grown epitaxially on $SrTiO_3$ substrates.

4.2.3 Atomic force microscopy

The surface morphology of all samples was examined by AFM [13]. The AFM can be operated in different modes, for example, contact, tapping, or non-contact modes, depending on whether the interaction force between the probing tip and the sample is attracting or repelling [14]. Our AFM topography measurements were carried out in tapping mode in ambient and at room temperature, using a Nanoscope III or V controller. Doped silicon probes with a nominal force constant of 40 N/m and a resonance frequency of 300 kHz were used.

Tapping-mode AFM operates by scanning a fine tip, which is attached to the end of an oscillating cantilever, across the sample surface. The cantilever is usually oscillated at a frequency close to its resonance frequency, with an amplitude ranging typically from 20 – 100 nm. This cantilever oscillation is driven by a small piezoelectric element mounted in the AFM tip holder. The tip gently taps on the sample surface during scanning, touching the surface at the bottom of its swing. A set-point amplitude, i.e.,

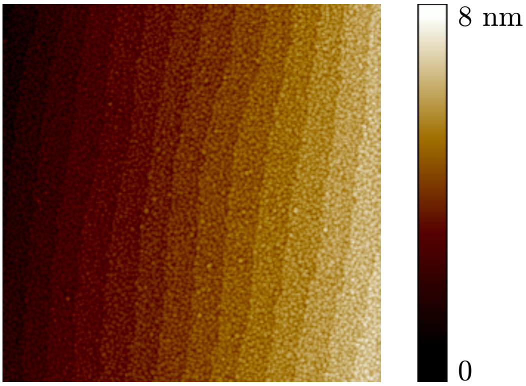

Figure 4.6: AFM topography image ($5 \times 5\ \mu m^2$) of a 12 nm thick $PbTiO_3$ film grown on a $SrRuO_3/SrTiO_3$ heterostructure showing a well-defined step and terrace surface structure.

a constant tip−sample interaction, is maintained using a feedback mechanism by maintaining a constant root-mean-square (RMS) of the oscillation signal, recorded by a position-sensitive photodiode detector, based on the measured laser signal reflected from the cantilever (figure 4.9). Changes in height across the sample surface will be corrected by adjusting and moving the piezoelectric scanner vertically, in order to keep the set-point amplitude constant. These height corrections are stored by a computer and translated to a topographic image of the sample surface. Figure 4.6 displays a typical tapping-mode AFM topography image of a 12 nm thick $PbTiO_3$ film grown on $SrRuO_3/SrTiO_3$. Note that the step and terrace structure, similar to that of the $SrTiO_3$ substrate, is preserved at the PTO film surface.

4.3 Scanning tunneling microscopy lithography

STM is a technique for surface imaging and characterization with an atomic-scale spatial resolution. It was invented by Gerd Binnig and Heinrich Rohrer at IBM Zürich in 1981, and they were awarded the *Nobel Prize in Physics* in 1986 for this great achievement. The STM is based on the concept of quantum-mechanical tunneling. When a bias voltage, V, is applied between a conducting tip and a metallic or semiconducting surface, electrons can tunnel through the gap[4] between the tip and the scanned surface, establishing a stable tunneling current. By measuring the tunneling current, I, the tip−surface separation distance, z, can be determined by the expression

$$I \sim V e^{-\mathrm{c}z} \tag{4.2}$$

where c is a constant. Since the tunneling current is exponentially dependent on the tip−surface distance, the depth resolution can be very high [15].

Recently, STM has been successfully employed to obtain nanoscale surface modifications of many different materials, including perovskite oxides [16, 17, 18] (see Paper I). In our group, we have established STM etching of $SrRuO_3$ thin film surfaces [19, 20, 21]. To perform STM line etching, a mechanically cut and conducting Pt/Ir tip is programmed to scan back and forth over a preselected area for a certain time, while a bias voltage, above a threshold value, is applied between the tip and the grounded $SrRuO_3$ film grown on a $SrTiO_3$ substrate, as schematically shown in figure 4.7(a). Examples of etched line patterns are displayed in figure 4.7(b). Note that multiple tips can be formed at the tip apex after extensive etching, as can

---

[4] The gap distance between the scanning tip and the sample surface must be narrow enough for their wave functions to overlap. Typically, it is on the order of a few nm.

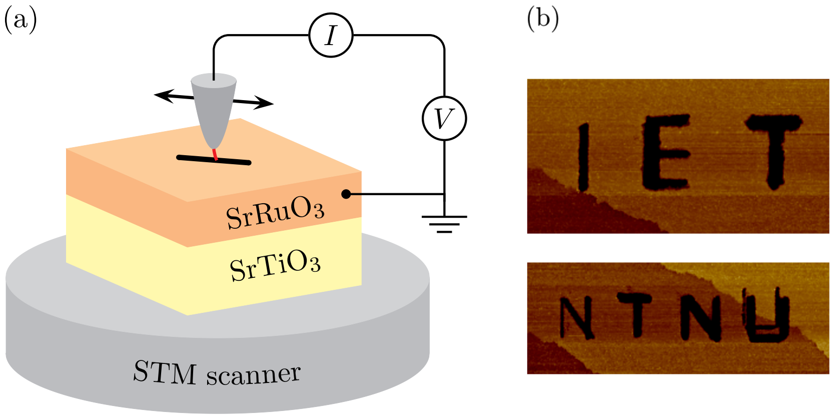

Figure 4.7: (a) Schematic illustration of STM line nanostructuring. (b) Patterns defined into a $SrRuO_3$ thin film surface. The horizontal scan sizes of the STM images are 500 nm (top) and 800 nm (bottom).

be seen from the letter *"U"* in the bottom STM image. For the $SrRuO_3$ material system, a lateral line resolution of $\sim$ 5 nm was achieved. The main motivation for STM lithography is to create nanoscale complex templates of $SrRuO_3$ for subsequent growth of laterally confined sub-50 nm $PbTiO_3$ nanostructures.

4.4 Piezoresponse force microscopy

Recently, contact-AFM operated in the PFM mode has been widely implemented to characterize the piezoelectric properties of ferroelectric nanostructures [23, 24]. In the PFM mode, an AC bias voltage is applied between the scanning metallic tip and the bottom electrode of the ferroelectric nanostructure, as depicted in figure 4.8. The modulation frequency and the amplitude of the AC bias signal are typically on the order of several kHz and a few volt, respectively. The amplitude is usually much lower than the coercive voltage of the sample in order not to switch the direction of polarization. The ferroelectric material will deform in response to the applied signal due to the converse piezoelectric effect (equation (2.12)). As can be seen in figure 4.8, the ferroelectric nanostructure will respond in-phase or out-of-phase with the applied oscillating signal, depending on the two possible polarization states. The nanostructure expands (figure 4.8(a)) when the applied electric field is oriented parallel to the polarization due to a positive longitudinal piezoelectric coefficient, d_{33}. Note that the transverse

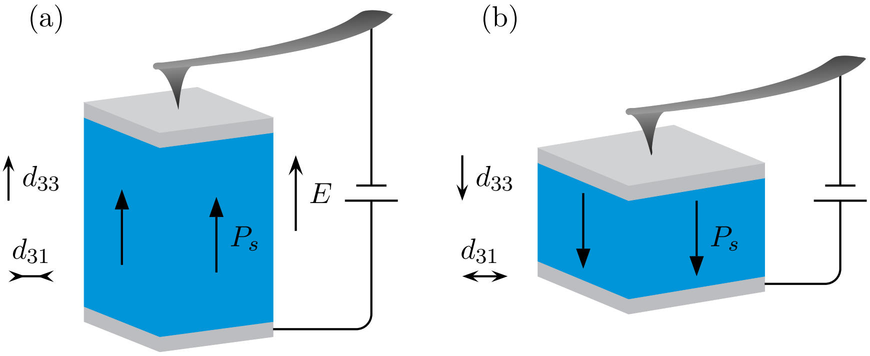

Figure 4.8: Investigation of the converse piezoelectric effect in ferroelectric perovskite nanostructures using PFM. (a) The nanostructure expands when the direction of applied electric field is parallel to the spontaneous polarization due to d_{33}. Also superimposed, d_{31} gives rise to a lateral contraction. (b) Antiparallel alignment of the applied electric field and the spontaneous polarization leads to a vertical contraction and a horizontal expansion of the nanostructure. From [22].

piezoelectric coefficient, d_{31}, also contributes to the overall longitudinal deformation if the nanostructure is not completely clamped. However, when the direction of polarization is oppositely oriented to the field (figure 4.8(b)), a vertical contraction occurs, and the nanostructure is expanded horizontally. The signals of the piezoelectric response are recorded and analyzed by a lock-in amplifier system. The amplitude (in-phase component) of the piezoelectric signal is a measure of the effective piezoelectric coefficient, and the phase gives the sign of polarization. The phase difference between two oppositely oriented polarizations is ideally 180°. Using this technique, ferroelectric domains with antiparallel polarization can be non-destructively visualized when the probing tip is scanned, in direct contact (i.e., without a top electrode), across the sample surface. Unlike the situation with a top electrode (figure 4.8), the electric field, generated by the tip, becomes inhomogeneous and is localized spatially beneath the tip [25], i.e., the field drops quickly in the radial direction away from the tip apex [26]. Hence, only local electromechanical properties of the ferroelectric material, averaged over a certain volume beneath the tip, are probed.

For the present study, a commercial Multimode V AFM equipped with both internal and external (Stanford Research 830) lock-in amplifier systems and a signal access module was used for the PFM measurements. Figure 4.9 shows the experimental setup for the PFM measurements of $PbTiO_3$

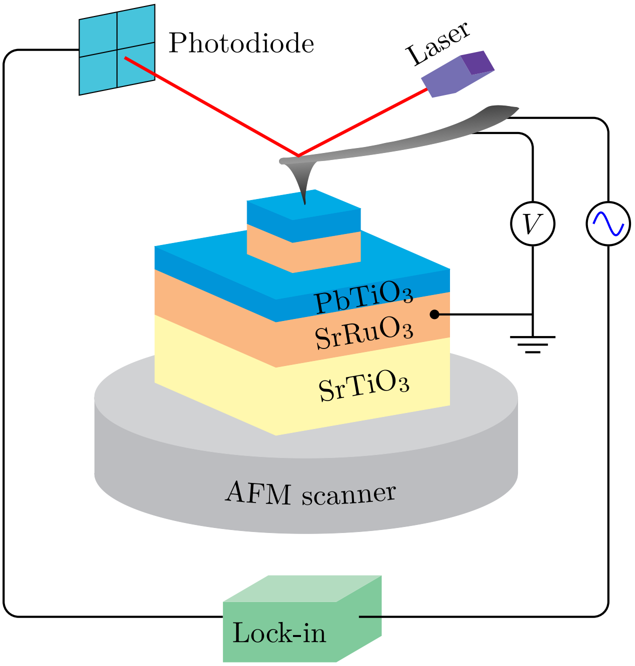

Figure 4.9: Schematic illustration of experimental setup for PFM measurements of piezoelectric properties of PbTiO$_3$ nanomesas, grown on nanostructured SrRuO$_3$/SrTiO$_3$ templates.

nanomesas, fabricated on nanostructured SrRuO$_3$/SrTiO$_3$ templates. In order to probe local piezoelectric hysteresis properties, a DC bias voltage is applied to the sample, in addition to the AC bias voltage. Typically, the applied AC bias voltage had an amplitude of 1 V and a modulation frequency of 10 kHz, and a lock-in time constant of 10 ms was used. Representative piezoelectric hysteresis amplitude loop (figure 4.10(a)) and phase loop (figure 4.10(b)) were measured on a PbTiO$_3$ nanomesa, with a lateral size of $\sim$ 55 nm and a thickness of $\sim$ 4 nm, by gradually sweeping the DC bias voltage in the range of -1 to $+1$ V in 512 steps with the duration of each step being 100 ms. The piezoresponse hysteresis loop in figure 4.10(c), defined as amplitude × cos(phase), is an evidence for the ferroelectric domain switching in the PbTiO$_3$ nanomesa investigated.

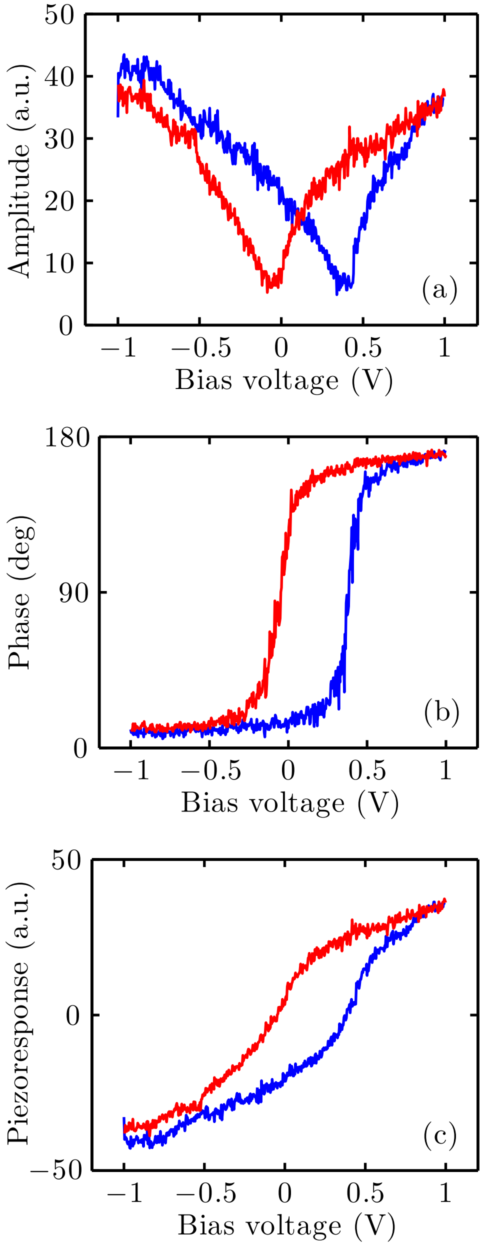

Figure 4.10: Piezoelectric hysteresis amplitude (a) and phase (b) loops measured on a $PbTiO_3$ nanomesa, with a lateral size of ∼ 55 nm and a thickness of ∼ 4 nm. The piezoresponse hysteresis loop (c) is defined as amplitude × cos(phase). The DC bias voltage was ramped from −1 to +1 V (blue curve) and then back to −1 V (red curve).

References

[1] J. H. Haeni, P. Irvin, W. Chang, R. Uecker, P. Reiche, Y. L. Li, S. Choudhury, W. Tian, M. E. Hawley, B. Craigo, A. K. Tagantsev, X. Q. Pan, S. K. Streiffer, L. Q. Chen, S. W. Kirchoefer, J. Levy, and D. G. Schlom. Room-temperature ferroelectricity in strained $SrTiO_3$. *Nature*, 430:758, 2004.

[2] M. Adachi, J. Harada, T. Ikeda, S. Nomura, E. Sawaguchi, and T. Yamada. Simple perovskite-type oxides. In *Oxides*, volume 16a of *Landolt-Börnstein – Group III Condensed Matter: Numerical Data and Functional Relationships in Science and Technology*, pages 45–87. Berlin: Springer-Verlag, 1981.

[3] M. Kawasaki, K. Takahashi, T. Maeda, R. Tsuchiya, M. Shinohara, O. Ishiyama, T. Yonezawa, M. Yoshimoto, and H. Koinuma. Atomic control of the $SrTiO_3$ crystal surface. *Science*, 266:1540, 1994.

[4] T. Ohnishi, K. Shibuya, M. Lippmaa, D. Kobayashi, H. Kumigashira, M. Oshima, and H. Koinuma. Preparation of thermally stable TiO_2-terminated $SrTiO_3(100)$ substrate surfaces. *Appl. Phys. Lett.*, 85:272, 2004.

[5] G. Shirane and S. Hoshino. On the phase transition in lead titanate. *J. Phys. Soc. Jpn.*, 6:265, 1951.

[6] M. E. Lines and A. M. Glass. *Principles and Applications of Ferroelectrics and Related Materials.* Oxford: Clarendon Press, 1979.

[7] R. E. Cohen. Origin of ferroelectricity in perovskite oxides. *Nature*, 358:136, 1992.

[8] C. B. Eom, R. J. Cava, R. M. Fleming, J. M. Phillips, R. B. van Dover, J. H. Marshall, J. W. P. Hsu, J. J. Krajewski, and W. F. Peck, Jr. Single-crystal epitaxial thin films of the isotropic metallic oxides $Sr_{1-x}Ca_xRuO_3$ $(0 \leq x \leq 1)$. *Science*, 258:1766, 1992.

[9] Q. Gan, R. A. Rao, and C. B. Eom. Control of the growth and domain structure of epitaxial $SrRuO_3$ thin films by vicinal (001) $SrTiO_3$ substrates. *Appl. Phys. Lett.*, 70:1962, 1997.

[10] W. Bensch, H. W. Schmalle, and A. Reller. Structure and thermochemical reactivity of $CaRuO_3$ and $SrRuO_3$. *Solid State Ionics*, 43:171, 1990.

[11] J.-M. Triscone, L. Frauchiger, M. Decroux, L. Miéville, Ø. Fischer, C. Beeli, P. Stadelmann, and G.-A. Racine. Growth and structural properties of epitaxial $Pb(Zr_xTi_{1-x})O_3$ films and $Pb(Zr_xTi_{1-x})O_3$-cuprate heterostructures. *J. Appl. Phys.*, 79:4298, 1996.

[12] A.-B. Posadas, M. Lippmaa, F. J. Walker, M. Dawber, C. H. Ahn, and J.-M. Triscone. Growth and novel applications of epitaxial oxide thin films. In K. M. Rabe, C. H. Ahn, and J.-M. Triscone, editor, *Physics of Ferroelectrics: A Modern Perspective*, volume 105 of *Topics in Applied Physics*, pages 219–304. Berlin Heidelberg: Springer-Verlag, 2007.

[13] G. Binnig, C. F. Quate, and Ch. Gerber. Atomic force microscope. *Phys. Rev. Lett.*, 56:930, 1986.

[14] Veeco Instruments Inc. *MultiMode SPM Instruction Manual*, 2006.

[15] G. Binnig, H. Rohrer, Ch. Gerber, and E. Weibel. Surface studies by scanning tunneling microscopy. *Phys. Rev. Lett.*, 49:57, 1982.

[16] I.-W. Lyo and P. Avouris. Field-induced nanometer- to atomic-scale manipulation of silicon surfaces with the STM. *Science*, 253:173, 1991.

[17] I. Heyvaert, E. Osquiguil, C. Van Haesendonck, and Y. Bruynseraede. Etching of screw dislocations in $YBa_2Cu_3O_7$ films with a scanning tunneling microscope. *Appl. Phys. Lett.*, 61:111, 1992.

[18] C. C. You, N. V. Rystad, A. Borg, and T. Tybell. Nanoscale structuring of $SrRuO_3$ thin film surfaces by scanning tunneling microscopy. *Appl. Surf. Sci.*, 253:4704, 2007.

[19] Ø. Dahl. Nanoscale structuring of $SrRuO_3$; a scanning tunneling microscopy approach. Master's thesis, Norwegian University of Science and Technology, 2003.

[20] S. Hallsteinsen. Nanoscale lithography of $SrRuO_3$ using an STM. Master's thesis, Norwegian University of Science and Technology, 2004.

[21] N. V. Rystad. STM nanostructuring of $SrRuO_3$. Master's thesis, Norwegian University of Science and Technology, 2005.

[22] A. Rüdiger, T. Schneller, A. Roelofs, S. Tiedke, T. Schmitz, and R. Waser. Nanosize ferroelectric oxides – tracking down the superparaelectric limit. *Appl. Phys. A*, 80:1247, 2005.

[23] M. Alexe and A. Gruverman, editor. *Nanoscale Characterisation of Ferroelectric Materials: Scanning Probe Microscopy Approach.* Berlin Heidelberg: Springer-Verlag, 2004.

[24] A. Gruverman and A. Kholkin. Nanoscale ferroelectrics: processing, characterization and future trends. *Rep. Prog. Phys.*, 69:2443–2474, 2006.

[25] S. V. Kalinin and D. A. Bonnell. Imaging mechanism of piezoresponse force microscopy of ferroelectric surfaces. *Phys. Rev. B*, 65:125408, 2002.

[26] D. A. Scrymgeour and J. W. P. Hsu. Absence of elastic clamping in quantitative piezoelectric force microscopy measurements of nanostructures. *Appl. Phys. Lett.*, 93:233114, 2008.

Chapter 5

Paper 1

Nanoscale structuring of $SrRuO_3$ thin film surfaces by scanning tunneling microscopy

Chang Chuan You, Nils Vidar Rystad, Anne Borg, and Thomas Tybell

Applied Surface Science **253** (2007) 4704–4708

Abstract

Surface modifications through line etching of $SrRuO_3$ thin films have been carried out using a scanning tunneling microscope under ambient conditions. The line etching is found to be dependent on both bias voltage and scan speed for a given number of scan repetitions. We observe that an applied voltage above a threshold value is required for successful line etching. The depth of the etched lines is increasing with increasing bias voltage and scan repetitions as well as with decreasing scan speed. Moreover, sub-50 nm laterally confined mesa structures could be reproducibly etched on the $SrRuO_3$ thin film surfaces.

5.1 Introduction

Functional oxide materials possess interesting electronic and mechanical properties for nanoelectronic applications [1]. As the material dimensions are scaled down to the nanometer length scale, the physical properties are expected to be altered by the size reduction. In order to study and understand the size effects it is important to develop new nanostructuring methods. The downscaling can be achieved by employing conventional top-down techniques such as photo and electron beam lithography or novel bottom-up approaches. Alternative nanostructuring routes based on scanning probes offer an exciting possibility in the development of nanoscale-engineered templates for growth of epitaxial oxide nanostructures.

Scanning probes have been intensively used to obtain nanoscale surface modifications of a variety of materials, for example, graphite [2, 3], gold [4, 5, 6, 7], silicon [8, 9], and $YBa_2Cu_3O_7$ (YBCO) [10, 11, 12]. The dependence of surface modification on bias voltage and tunneling current has been investigated under various chemical environments in some of these experiments. For example, a fixed threshold voltage for surface modification was found when a graphite surface was covered with water [2], whereas no surface modification was observed in vacuum or dry gases [2, 3]. Above a critical relative humidity, a nearly constant threshold voltage was observed for hole formation on gold [6]. For the hole formation on silicon, the threshold voltage was found to be dependent on the tunneling current [8], and the success rate of hole formation was increasing with decreasing tip–sample separation [9]. The ambient was also found to be important for surface modification of YBCO, investigations showed that water vapor and CO_2 are needed in order to achieve appreciable etching [11]. Based on these observations, several possible mechanisms have been proposed for the surface modifications in the various experiments, including mechanical contact [4, 5], chemical reactions [2, 6, 11], field-induced evaporation [7, 8, 9, 10, 11, 12], local heating [13], electromigration [14], and combinations of these.

In this paper, we report on scanning tunneling microscopy (STM) etching experiments carried out on metallic $SrRuO_3$ (SRO) thin films under ambient conditions. SRO is a chemically inert material well lattice-matched to most perovskites, which makes it an interesting material for the fabrication of nanoscale templates. We demonstrate the feasibility of using STM to etch the SRO film surface and to pattern nanoscale templates. Moreover, we present data on how bias voltage, tunneling current, and scan speed affect STM etching of SRO thin films.

5.2 Experimental

Thin films of ~ 500 Å (110)-oriented SRO were epitaxially grown on (001)-oriented $SrTiO_3$ (STO) substrates by off-axis radio frequency magnetron sputtering. The films were deposited in a mixed atmosphere of oxygen and argon ($O_2 : Ar = 4 : 10$) at a total pressure of 100 mTorr. The substrate temperature was varied between 750 and 850 °C. Atomic force microscopy (AFM) and STM topography measurements revealed a step and terrace

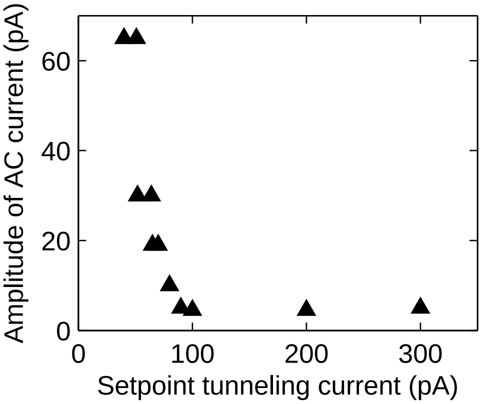

Figure 5.1: The amplitude of AC current oscillations versus setpoint tunneling current obtained at a bias voltage of 500 mV. The STM tip was positioned above a fixed point on the film surface during the measurements.

structure consisting of 150 – 250 nm wide terraces, separated by steps with a height of one to two unit cells. The root-mean-square surface roughness at the terraces was found to be typically ∼ 1 Å. X-ray diffraction analysis revealed single-crystal thin film growth, and the rocking curves measured around the (110) reflection showed a mosaic spread of less than 0.1°.

The etching experiments were performed in a commercial STM system using mechanically cut Pt/Ir tips. The STM was operated in air and at room temperature. Constant current mode was employed for the investigation and the feedback loop was switched on for both etching and imaging. For normal imaging, a positive bias voltage of typically 500 mV and a tunneling current of 300 pA were used. The nanostructuring was achieved by controlling bias voltage, tunneling current, and scan speed. The bias voltage was varied between 1.6 and 3.0 V, the scan speed between 100 and 1500 nm/s, and 50 to 200 scan repetitions were used. Prior to etching, the setpoint tunneling current was set to 40 – 60 pA with an imposed AC component with a frequency of 50 Hz and an amplitude of 30 – 65 pA as shown in figure 5.1. Since the feedback loop was on during etching, the imposed AC oscillation at the given setpoint tunneling currents results in a vertical displacement of the tip in the range of 1 – 2 nm. The AC component originates from the power line, and by carefully choosing the integral gain in the feedback loop and the setpoint tunneling current the AC component can be controlled. As can be seen in figure 5.1, the amplitude of the AC current oscillations is increasing with decreasing setpoint tunneling currents.

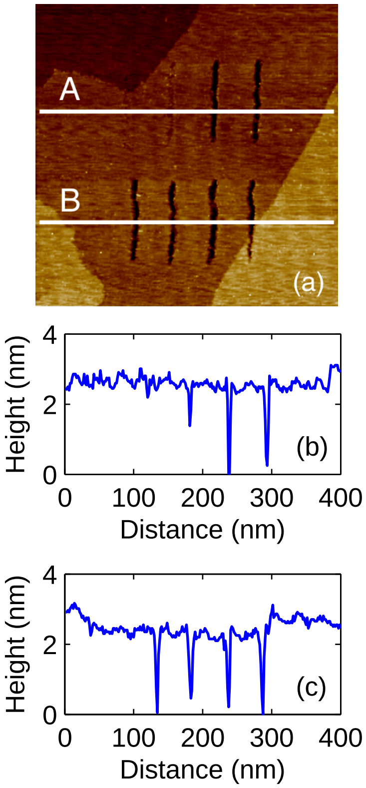

Figure 5.2: (a) STM image (400×400 nm^2) of a typical data set for line etching experiments. Eight lines ~ 100 nm long were consecutively etched on the SRO film surface using bias voltage of 2.2 V, setpoint tunneling current of 60 pA, scan speed of 100 nm/s and 50 scan repetitions. (b) and (c) show the surface profiles along the marker lines A and B in (a), respectively.

In order to perform line etching the STM tip was programmed to scan back and forth repeatedly over a preselected area. For the present experiments, eight lines were consecutively etched by moving the tip starting in the upper left and ending in the lower right corner of the selected area. The lines were approximately 100 nm long with a separation of 50 nm. The STM image in figure 5.2(a) displays a data set typical for the line etching experiments obtained at bias voltage 2.2 V, setpoint tunneling current 60 pA, scan speed 100 nm/s, and 50 scan repetitions. As can be seen in figure 5.2, there is an evolution of the etching from line to line in the upper row. After $3-4$ lines the etching process is more reproducible. This is illustrated

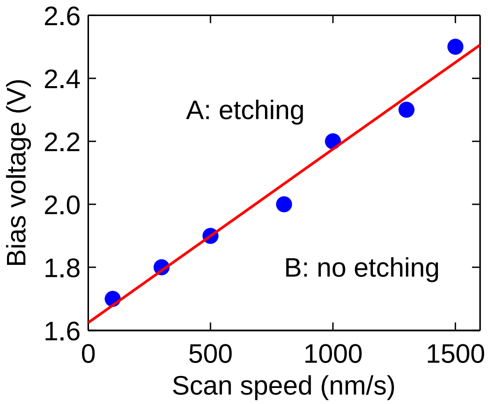

Figure 5.3: The dependence of successful etching on bias voltage and scan speed when scanning each line 50 times. The points correspond to the threshold voltage at which etching occurs. The line is guide to the eye.

by the shown surface profiles along line A (figure 5.2(b)) and line B (figure 5.2(c)). For this reason, only the four lower lines were used for data analysis of each data set.

5.3 Results and discussion

Figure 5.3 shows the dependence of successful etching on bias voltage and scan speed when scanning each line 50 times. Here we have defined the etching to be successful if the resulting line is continuous for at least 50 nm with a minimum average depth of half a unit cell. The points in figure 5.3 show the lowest voltage at which etching is observed for a given scan speed. For voltages below this value no etching is observed. The line through the data points thus indicates the division between combinations of applied voltage and scan speed where etching occurs (region A) and where etching does not occur (region B). Thus we find that the etching process requires a bias voltage larger than a threshold value, which depends on the scan speed of the STM tip. In contrast, no such threshold voltage could be established for line etching of SRO thin films under ultra-high-vacuum conditions using tungsten tips [15]. A threshold voltage has previously been observed for other systems [2, 6, 9]. However, this study shows that such threshold voltages in general may depend on scan speed. For the $SrRuO_3$ system, we note that the tip quality quickly deteriorates for bias voltages above 2.8 V by the formation of multiple tips or strongly altered tip shape.

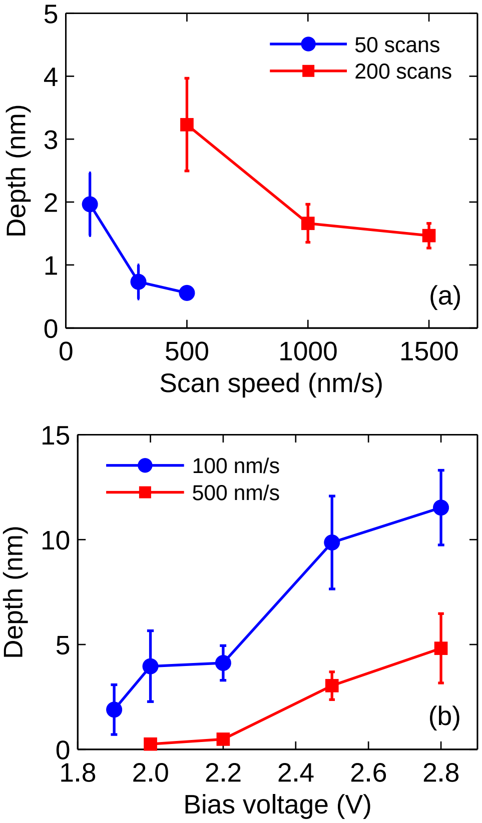

Figure 5.4: (a) Depth versus scan speed at a bias voltage of 2.2 V for 50 and 200 scan repetitions, respectively. The general trend is that the line depth decreases for increasing scan speed. (b) Depth versus bias voltage using 50 scan repetitions for scan speeds of 100 and 500 nm/s, respectively. The data indicate that the line depth increases with increasing bias voltage. The lines are guides to the eye.

In figure 5.4(a), we plot the correlation between the depth of the etched lines and the scan speed for a bias voltage of 2.2 V. We find that an increase in scan speed results in an decrease in line depth for both 50 and 200 scan repetitions. Figure 5.4(b) shows the dependence of depth on bias voltage using 50 scan repetitions for scan speeds of 100 and 500 nm/s, respectively. As can be seen, the line depth is increasing with increasing bias voltage. It should be pointed out that the discrepancy between the average depths in figure 5.4(a) and (b) for the identical set of etching parameters (i.e., bias voltage of 2.2 V, scan speed of 100 nm/s, and 50 scan repetitions) could

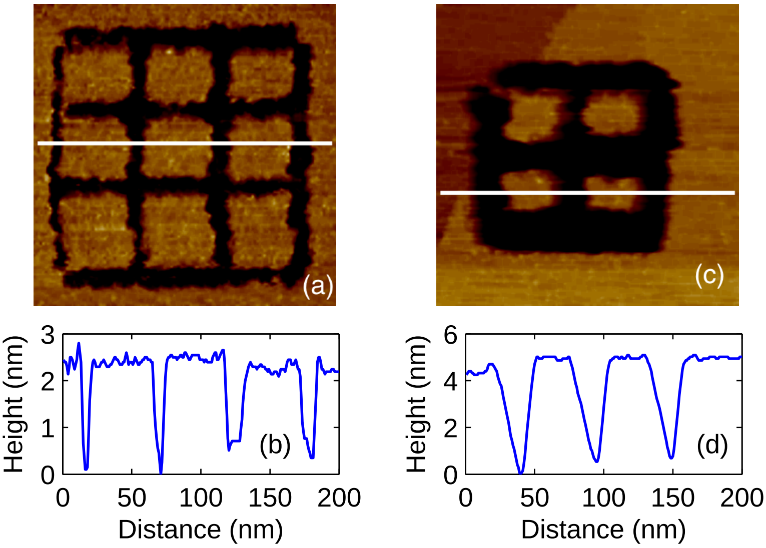

Figure 5.5: (a) 3 × 3 array structure created by STM etching using bias voltage of 2.8 V, setpoint tunneling current of 40 pA, scan speed of 100 nm/s, and 7 scan repetitions. The surface profile (b) along the marker line in (a) shows that the average width and depth of the SRO mesas are 46 and 2.1 nm, respectively. (c) 2 × 2 array structure created by using bias voltage of 2.4 V, setpoint tunneling current of 60 pA, scan speed of 100 nm/s, and 20 scan repetitions. The average width and depth of the SRO mesas are 42 and 4.2 nm, respectively, as shown by the surface profile (d).

tentatively be attributed to the difference between tip shapes since different tips were used to obtain data shown in figure 5.4(b). We note that the depth of the etched lines varied using different tips even though the film surface quality and the etching parameters were not changed. Although the value of line depth varies with the tip quality, the trends indicated by figure 5.4(a) and (b) are consistent with each other. It is interesting to note that for a given bias voltage and number of scan repetitions, deeper line etching is obtained by reducing the scan speed, as shown in figure 5.4(b). This result implies that the etching process is a function of the total time that the STM tip spends above each point on the film surface. Since the surface modification of SRO was obtained at a high voltage and a low tunneling current, material removal by mechanical contact is not expected. Mechanisms responsible for the STM etching of SRO thin films that are consistent with our observations could be electric field induced evaporation [16] and chemical reactions, or a combination of these two mechanisms.

In general, upon etching we observed that the amount of residual material debris near the etched area is depending on the setpoint tunneling current. We note that by applying an AC component at small setpoint tunneling currents, hence large current oscillations as shown in figure 5.1, the material build-up is reduced as compared to large setpoint tunneling currents [17]. Remaining material debris could be removed by scanning the tip with a scan rate of 10 Hz over the etched area typically 4 times using normal imaging conditions. Figure 5.2(a) shows an image obtained after using this procedure. No excess material accumulation near the etched area can be observed in the figure. We also note that topographic imaging using the same scan parameters prior and after the etching process showed no noticeable difference, hence indicating similar tip quality.

We have also examined the feasibility of using STM etching to fabricate nanoscale SRO templates. In order to pattern a template, the horizontal lines followed by the vertical lines were consecutively etched by moving the tip to the preselected area. Figure 5.5(a) shows an 3×3 array structure created by STM etching using bias voltage of 2.8 V, setpoint tunneling current of 40 pA, scan speed of 100 nm/s, and 7 scan repetitions. The surface profile in figure 5.5(b) along the marker line in figure 5.5(a) shows that the average width and depth of the SRO mesas are 46 and 2.1 nm, respectively. Figure 5.5(c) shows an 2×2 array structure created by applying a bias voltage of 2.4 V, setpoint tunneling current of 60 pA, scan speed of 100 nm/s, and 20 scan repetitions. The average width and depth of the SRO mesas are 42 and 4.2 nm, respectively, as shown by the surface profile in figure 5.2(d). It can be seen by comparing figures 5.2(b) and (d) that deeper grooves around the SRO mesas could be achieved by increasing the scan repetitions.

5.4 Conclusions

We have used a scanning tunneling microscope to modify the surface structure of SRO thin films. The line etching is found to be dependent on both bias voltage and scan speed when scanning each line 50 times. At a given scan speed, a threshold voltage has to be applied for successful etching. The depth of the etched lines is increasing with increasing bias voltage and scan repetitions as well as with decreasing scan speed. Moreover, it is demonstrated that templates of sub-50 nanometer lateral size could be reproducibly etched on SRO thin films.

References

[1] C. H. Ahn, J.-M. Triscone, and J. Mannhart. Electric field effect in correlated oxide systems. *Nature*, 424:1015, 2003.

[2] R. M. Penner, M. J. Heben, N. S. Lewis, and C. F. Quate. Mechanistic investigations of nanometer-scale lithography at liquid-covered graphite surfaces. *Appl. Phys. Lett.*, 58:1389, 1991.

[3] T. R. Albrecht, M. M. Dovek, M. D. Kirk, C. A. Lang, C. F. Quate, and D. P. E. Smith. Nanometer-scale hole formation on graphite using a scanning tunneling microscope. *Appl. Phys. Lett.*, 55:1727, 1989.

[4] C. X. Guo and D. J. Thomson. Material transfer between metallic tips and surface in the STM. *Ultramicroscopy*, 42–44:1452, 1992.

[5] J. I. Pascual, J. Méndez, J. Gómez-Herrero, A. M. Baró, N. García, and V. T. Binh. Quantum contact in gold nanostructures by scanning tunneling microscopy. *Phys. Rev. Lett.*, 71:1852, 1993.

[6] C. Lebreton and Z. Z. Wang. Critical humidity for removal of atoms from the gold surface with scanning tunneling microscopy. *J. Vac. Sci. Technol. B*, 14:1356, 1996.

[7] C. S. Chang, W. B. Su, and T. T. Tsong. Field evaporation between a gold tip and a gold surface in the scanning tunneling microscope configuration. *Phys. Rev. Lett.*, 72:574, 1994.

[8] A. Kobayashi, F. Grey, R. S. Williams, and M. Aono. Formation of nanometer-scale grooves in silicon with a scanning tunneling microscope. *Science*, 259:1724, 1993.

[9] I.-W. Lyo and P. Avouris. Field-induced nanometer- to atomic-scale manipulation of silicon surfaces with the STM. *Science*, 253:173, 1991.

[10] I. Heyvaert, E. Osquiguil, C. Van Haesendonck, and Y. Bruynseraede. Etching of screw dislocations in $YBa_2Cu_3O_7$ films with a scanning tunneling microscope. *Appl. Phys. Lett.*, 61:111, 1992.

[11] G. Bertsche, W. Clauss, F. E. Prins, and D. P. Kern. Investigation of the modification mechanism induced by a scanning tunneling microscope on $YBa_2Cu_3O_{7-\delta}$. *J. Vac. Technol. B*, 16:2833, 1998.

[12] Y. C. Fan, A. G. Fitzgerald, and J. A. Cairns. Nanoscale surface modification and nanostructural fabrication of $YBa_2Cu_3O_{7-x}$ thin films by scanning tunneling microscopy. *J. Vac. Sci. Technol. B*, 18:2377, 2000.

[13] Y. Z. Li, L. Vazquez, R. Piner, R. P. Andres, and R. Reifenberger. Writing nanometer-scale symbols in gold using the scanning tunneling microscope. *Appl. Phys. Lett.*, 54:1424, 1989.

[14] M. Ohto, S. Yamaguchi, and K. Tanaka. Migration of metals on graphite in scanning tunneling microscopy. *Jpn. J. Appl. Phys.*, 34:694, 1995.

[15] Ø. Dahl, S. Hallsteinsen, J. K. Grepstad, A. Borg, and T. Tybell. Nanoscale etching of metallic perovskites using STM. *Mater. Res. Soc. Symp. Proc.*, 811:445, 2004.

[16] T. T. Tsong. *Atom-Probe Field Ion Microscopy.* Cambridge: Cambridge University Press, 1990.

[17] S. Hallsteinsen. Nanoscale lithography of $SrRuO_3$ using an STM. Master's thesis, Norwegian University of Science and Technology, 2004.

Chapter 6

Paper 2

The fabrication and characterization of $PbTiO_3$ nanomesas realized on nanostructured $SrRuO_3/SrTiO_3$ templates

Chang Chuan You, Ryota Takahashi, Anne Borg,
Jostein K. Grepstad, and Thomas Tybell

Nanotechnology **20** (2009) 255705 (8pp)

Abstract

We report fabrication of $PbTiO_3$ nanomesas down to 30 nm lateral size and 4 nm high on nanostructured $SrRuO_3/SrTiO_3$ templates by off-axis radio frequency magnetron sputtering. The templates were prepared using a top-down lithography approach based on scanning tunneling microscopy. The growth rate of the $PbTiO_3$ nanomesas was found to decrease with increasing growth temperature as well as with shrinking template size. Piezoresponse force microscopy measurements for the $PbTiO_3$ nanomesas showed a strong increase in response with decreasing lateral size. A decrease of the coercive voltage was also observed for the same lateral size range. This laterally size-dependent behavior is attributed to reduction of in-plane strain, when shrinking the nanomesa lateral dimensions.

6.1 Introduction

Ferroelectric perovskite oxides possess functional properties, such as piezoelectricity, pyroelectricity, and ferroelectricity, which makes them interesting for a variety of applications, for example in sensors, actuators, surface acoustic wave filters, electro-optic modulators, and non-volatile random access memories [1, 2, 3, 4, 5]. With the aim of incorporating such materials in future nanoelectronic devices, there has been a tremendous effort to understand how size affects material properties at the nanometer length scale [6, 7, 8, 9, 10, 11, 12, 13]. Establishing the influence of film thickness on the ferroelectric polarization has been the target of a number of investigations [7, 8, 9, 10]. Recently, it was shown that ferroelectricity can be sustained in ultrathin films. For example, $PbTiO_3$ (PTO) films, with thicknesses down to 1.2 nm, were found to be ferroelectric [9]. For many envisaged devices effects from a small lateral size may also be important. According to recent theoretical findings [13], the ferroelectric phase transitions in zero-dimensional $Pb(Zr,Ti)O_3$ (PZT) nanostructures, with a diameter of ~ 8 nm and a height of ~ 6 nm, differ greatly from those of bulk ferroelectrics. This is attributed to the presence of a toroidal moment formed by electric dipole vortices.

In order to investigate ferroelectrics at the smallest length scale, it is important to develop suitable techniques for definition of nanoscale ferroelectric capacitor structures. Physical downscaling can be achieved by top-down approaches based on electron beam lithography (EBL) [14, 15, 16] and focused ion beam milling [17, 18], and by bottom-up approaches using self-assembly, self-patterning [19, 20, 21] or fabrication techniques which utilize shadow masks [22, 23]. Ferroelectric Pt/PZT/Pt capacitors of ~ 60 nm lateral size and $20 - 40$ nm high were grown using pulsed laser deposition with anodic aluminium oxide masks [23], while ferroelectric PTO nanograins down to ~ 20 nm in lateral size and ~ 6 nm high were achieved by deposition from chemical solution [20]. Investigation of the physical properties of such nanostructures revealed that the piezoelectric properties are strongly dependent on size. A prominent increase in the piezoelectric response was observed for 200 nm thick PZT nanostructures with decreasing lateral size from 200 to 100 nm [15], whereas the response was significantly decreased when the lateral size of 100 nm thick PZT cells was reduced from 1 μm to 100 nm [14]. These findings underline the importance of developing novel nanostructuring techniques, which offer the capability to define high quality and defect-free ferroelectric structures of nanoscale dimensions, so as to facilitate experimental investigations of size effects.

Alternative methods for nanostructuring based on scanning probes have recently attracted attention due to their high lateral resolution [24, 25, 26, 27, 28]. In particular, scanning tunneling microscopy (STM) was successfully employed for nanoscale surface modifications of perovskite oxides and to provide a lateral line resolution as small as 3 nm [27]. In a previous study [28], we have shown that nanoscale surface structures can be routinely etched in $SrRuO_3$ (SRO) thin films by such STM lithography. Here, we report on such top-down nanostructuring of SRO thin films by STM, to form templates for subsequent growth of PTO nanomesas by magnetron sputter deposition. These PTO nanomesas had a lateral size and thickness down to 30 and 4 nm, respectively. This approach offers the possibility to control the nanomesa geometry, which is highly desirable for investigation of physical properties of nanostructured ferroelectrics. The present fabrication technique also provides opportunities for construction of device structures from other technically important perovskite oxides such as multiferroics, manganites, and high-T_c superconductors. Moreover, we discuss how substrate temperature and template size affect the growth of PTO nanomesas, as well as the dependence of the piezoelectric response and coercive voltage on the nanomesa lateral size.

6.2 Experimental

SRO thin films of $\sim 35 - 50$ nm thickness were deposited on as-received, (001)-oriented single-crystalline $SrTiO_3$ (STO) substrates by off-axis radio frequency (RF) magnetron sputtering. The films were grown at substrate temperatures ranging from $\sim 590 - 690$ °C in a 100 mTorr atmosphere of oxygen and argon (O_2 : Ar = 4 : 10)[1]. Nanoscale templates were defined in the SRO thin films by employing a commercial ambient STM system equipped with mechanically cut Pt/Ir tips. The STM was operated in constant current mode, and the feedback was on for both etching and imaging. For normal imaging, a positive bias voltage of typically 500 mV and a tunneling current of 300 pA were used. In order to pattern a rectangular template, four lines were etched consecutively by scanning the tip over a preselected area. Typically, we used a bias voltage of 2.8 V, a set-point tunneling current of $40 - 60$ pA, a scan speed of 300 nm s^{-1}, and $200 - 300$ scan repetitions per line. Further details can be found elsewhere [28]. A series of templates with lateral size ranging from $\sim 30 - 260$ nm were prepared. PTO thin films with thicknesses $\sim 3 - 16$ nm were subsequently grown on

---

[1] The substrate temperature was typically measured at the center of the substrate, using an optical pyrometer at wavelength 1.5 μm with the emissivity set at 0.7.

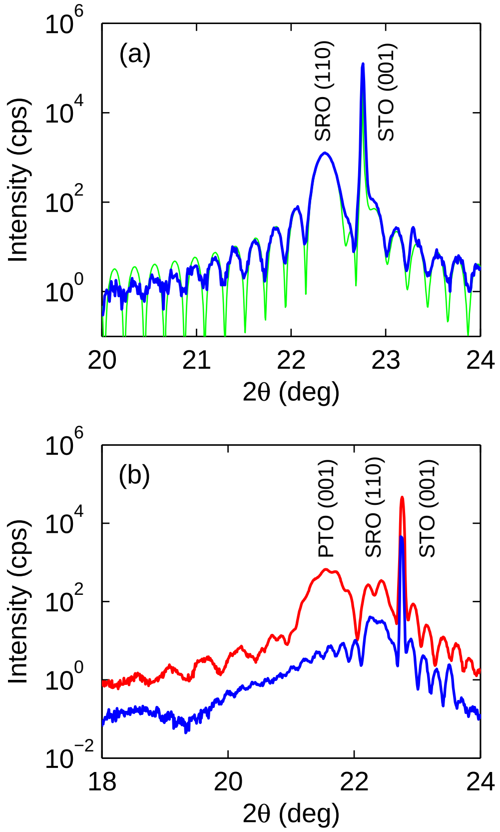

Figure 6.1: (a) $\theta - 2\theta$ diffractogram of the SRO (110) reflection for a 42 nm thick film. The additional satellite peaks (oscillation fringes) allow for precise measurement of the film thickness as indicated by the green fine curve. (b) $\theta - 2\theta$ diffractograms taken around the PTO (001) reflection for a 16 nm thick (upper red curve) and a 4 nm thick (lower blue curve) film deposited on an SRO thin film. Note that the measured intensity of the 4 nm thick sample is offset by an order of magnitude relative to the 16 nm thick sample.

the nanostructured SRO thin film templates by RF magnetron sputtering, in order to obtain the PTO nanomesas. The PTO films were deposited at a substrate temperature of $\sim 500 - 530$ °C in mixed ambient of oxygen and argon ($O_2 : Ar = 4 : 10$) with an overall pressure of 165 mTorr.

To analyze the crystalline properties of the PTO and SRO thin films, x-ray diffraction (XRD) measurements were carried out using a Bruker D8 Discover diffractometer. XRD analysis revealed single-crystalline epitax-

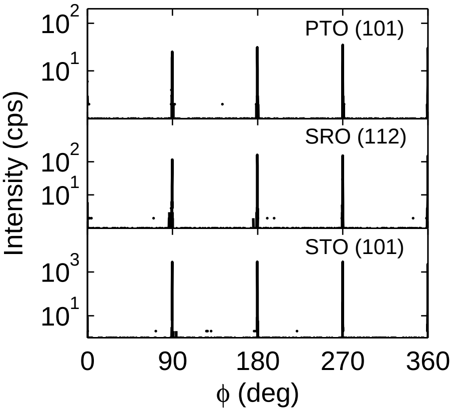

Figure 6.2: ϕ-scans of the PTO (101), SRO (112), and STO (101) reflections recorded for a 16 nm thick PTO film grown on SRO/STO.

ial growth of the SRO thin films. Figure 6.1(a) shows a typical $\theta - 2\theta$ diffractogram of SRO grown on STO substrate, with clearly defined finite thickness oscillation fringes. The SRO film thickness was determined at 42 nm by numerical fit to the measured oscillation fringes [29], as shown by the green fine curve. Rocking curves measured around the (110) Bragg reflection displayed a full width at half maximum of typically 0.02 – 0.03°, similar to that of the (001) STO substrate reflection. Figure 6.1(b) reports $\theta - 2\theta$ diffractograms taken of the (001) reflection for 16 nm thick (upper red curve) and 4 nm thick (lower blue curve) PTO films grown on SRO. Note that the thickness fringes of the SRO layer is superimposed on the PTO signal. The XRD data indicates c-axis oriented growth of a tetragonal PTO film. Rocking curves taken around the (001) Bragg peak showed a mosaic spread of less than 0.03° for the 16 nm thick film of PTO. Figure 6.2 displays ϕ-scans of the PTO (101), SRO (112), and STO (101) reflections for a PTO (16 nm)/SRO (39 nm)/STO sample. The four-fold symmetry apparent in the azimuthal scans is evidence of epitaxial growth for both PTO and SRO.

The surface morphology of the PTO, SRO, and STO layers was examined with tapping mode atomic force microscopy (AFM). Figure 6.3(a) shows a representative 2×2 μm^2 AFM topography scan of the SRO thin film surface. The SRO surface consists of a well-defined step and terrace structure, similar to that of the STO substrate. Such atomically smooth surfaces are a key prerequisite for successful and reproducible STM nanostructuring. Figures 6.3(b) – (c) show 2×2 μm^2 AFM topography scans of

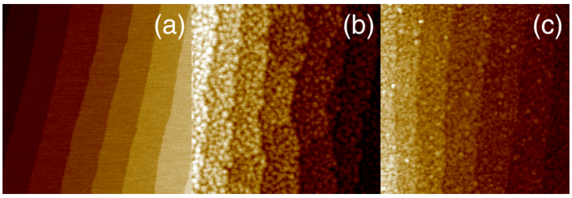

Figure 6.3: (a) Typical AFM topography image of the SRO thin film surface. AFM topography images of (b) 16 nm and (c) 4 nm thick PTO films grown on SRO. The scan size is 2 x 2 μm^2 for all three images.

the 16 and 4 nm thick films of PTO on SRO, respectively. The step and terrace surface structure is preserved, similar to that of the SRO thin film and STO substrate surfaces.

In order to carry out local nanoscale AFM investigations, markers were etched in the STO substrates prior to the subsequent film deposition, using a commercial RAITH Elphy Plus EBL system. To prepare these markers, a $\sim$ 2 μm thick layer of PMMA (polymethyl methacrylate) resist was spun onto the STO substrate. Markers with a linewidth of 8 μm were subsequently written by e-beam using an accelerating voltage of 20 kV, a probe current of 120 – 130 pA, and an area dose of 260 μA/cm^{-2}. After resist development, the markers were defined in the STO substrate by argon ion etching. Residual PMMA was removed by annealing at 950 °C for 1 h in an oxygen gas flow. The obtained markers could be readily located using the optical positioning system of the AFM.

In order to investigate the piezoelectric properties of the PTO thin films and nanomesas, both piezoresponse force microscopy (PFM) imaging and local hysteresis measurements were performed using a commercial Multimode V AFM equipped with an internal lock-in amplifier system and a signal access module [7, 30]. All PFM measurements were performed in air and at room temperature. Conductive Pt/Ir-coated Si tips were used as mobile top electrode[2]. For imaging, an ac bias voltage of amplitude 1 V and modulation frequency 10 kHz was applied between the conductive scanning tip and the SRO film, which served as a bottom electrode. In

---

[2] We note that for two different batches of AFM tips were used here, one was found to yield a systematically higher piezoelectric amplitude than the other under exactly same experimental conditions. Force curve measurements showed a force constant of typically $\sim$ 2.5 and 4.5 Nm^{-1} for the two batches. As a result, each amplitude data set was obtained with tips from the same batch. The amplitude data shown in figures 6.9 and 6.10(b) for the 16 nm thick PTO sample was obtained using tips from the batch with force constant 4.5 Nm^{-1}, otherwise tips from the batch with force constant 2.5 Nm^{-1} were employed.

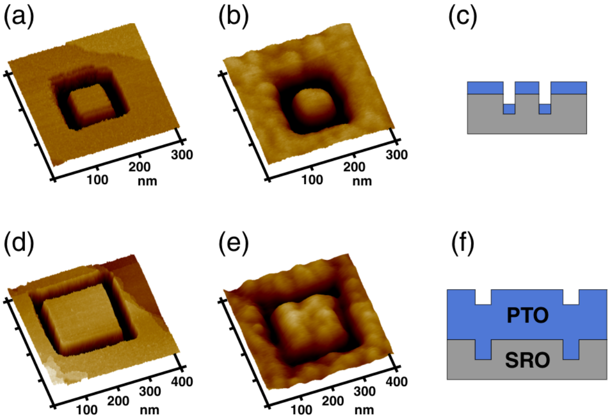

Figure 6.4: STM topography images (a) and (d) show two representative templates defined in the SRO thin film surface by STM lithography. AFM topography images of the PTO nanomesas obtained after (b) 4 nm and (e) 16 nm thick PTO film depositions on these SRO templates as shown in (a) and (d). The ideal growth of PTO on a nanostructured SRO template is illustrated for the 4 nm thick (c) and the 16 nm thick (f) depositions, respectively.

order to probe the local piezoelectric hysteresis properties, a dc bias voltage was superimposed on the tip ac bias voltage, while the amplitude and phase signals were continuously recorded. The amplitude is a measure of the local effective piezoelectric coefficient d_{33}, and the phase reflects the direction of polarization in the film underneath the tip. In our epitaxial thin films of tetragonal PTO, the two equivalent polarization states were aligned parallel to the growth direction, i.e., perpendicular to the film surface [31, 32]. A dc bias voltage sweep of ±2 V was employed for PTO continuous films and nanomesas alike, based on a 16 nm thick PTO sample, while ±1 V was sufficient to switch the nanomesas defined for a 4 nm thick PTO sample. An estimate of the piezoelectricity was obtained from the saturation regions of the piezoresponse hysteresis loops, using average amplitudes acquired from bias voltages of $\pm(1.9-2)$ V (all continuous films and nanomesas obtained from the 16 nm thick PTO sample) and $\pm(0.9-1)$ V (nanomesas obtained from the 4 nm thick PTO sample)[3].

---

[3] The observed trend of increasing piezoelectricity upon shrinking the lateral dimensions was found to be independent on the region of the saturated hysteresis loop that was used for this analysis; e.g., $\pm(1.6-2)$ V and $\pm(0.6-1)$ V.

6.3 Results and discussion

The STM topography images in figures 6.4(a) and (d) show typical SRO templates with an average lateral size of ~ 65 and ~ 175 nm, respectively. The AFM images in figures 6.4(b) and (e) show the resulting topography after deposition of 4 and 16 nm thick PTO films. The average lateral size of these PTO nanomesas are ~ 60 and ~ 160 nm. The average depth of the etched trenches surrounding the SRO template was estimated at $\sim 4 - 6$ nm. This suggests that for PTO film thicknesses less than the depth of the trenches, which outline the SRO template, it is possible to form isolated islands of PTO, as illustrated in figure 6.4(c). For film thicknesses exceeding the depth of the trenches, the template surface topography is preserved at the PTO surface, as is evident from comparison of figures 6.4(d) and (e) and schematically illustrated in figure 6.4(f). Hence, the proposed fabrication scheme for physical deposition on nanoscale templates can be used to define free standing islands as well as preparing nanostructured surfaces in thick homogeneous films.

Figure 6.5 depicts STM topography scans of two SRO templates with lateral size (a) 122 nm and (b) 47 nm, respectively. Figures 6.5(c) and (d) show AFM scans of the PTO nanomesas on these SRO templates after deposition of 4 nm PTO. The lateral size of these PTO nanomesas was estimated at 116 and 42 nm in (c) and (d), respectively. The width of the PTO nanomesa is always found to be smaller than that of the corresponding SRO growth template. The correlation between the average lateral size of the PTO nanomesas and their corresponding SRO templates is displayed in figure 6.5(e) for 3, 4, and 16 nm thick PTO samples. The solid line in this figure is a linear fit to the data, with a slope of 0.93. This indicates that the lateral size of PTO nanomesa is in general $\sim 5 - 10\%$ smaller than that of the SRO template.

Figure 6.6(a) shows an AFM line scan across a PTO nanomesa. As can be seen, the height of the nanomesa is lower than that of the surrounding thin film. In figure 6.6(b), this difference in height, Δh, is plotted versus the average lateral size of the nanomesas for the 3, 4, and 16 nm thick PTO films grown at a substrate temperature of 515 °C. A distinct increase in Δh was observed upon shrinking the lateral size below ~ 50 nm. Surface height differences up to $\Delta h \sim 1$ nm were measured for the smallest nanomesas. Figure 6.6(c) displays Δh versus substrate temperature during growth[4].

---

[4] The PTO nanomesas used for the temperature data analysis are taken from three different ~ 4 nm thick PTO samples with the average lateral sizes of the nanomesas being $\sim 30 - 50$ nm.

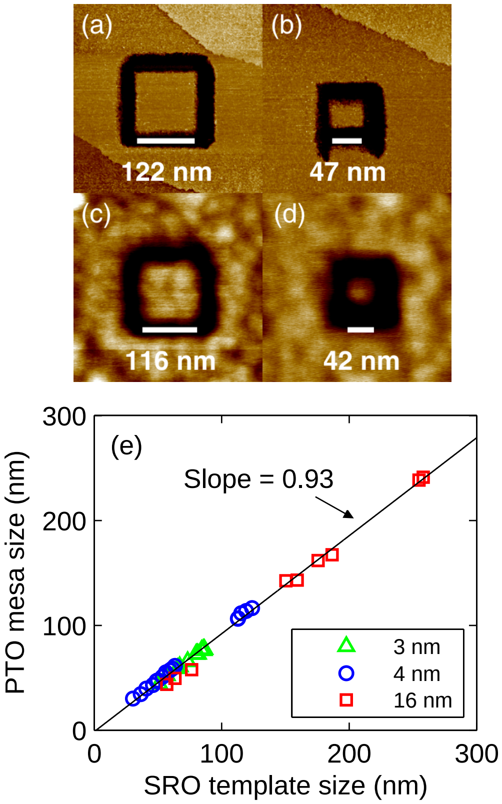

Figure 6.5: STM topography images of two templates with lateral size (a) 122 nm and (b) 47 nm, as defined by STM lithography in the SRO thin film. AFM topography measurements of the PTO nanomesas with lateral size (c) 116 nm and (d) 42 nm, grown on the SRO templates shown in (a) and (b) for 4 nm PTO deposition. (e) Average lateral size of the PTO nanomesas versus the SRO growth templates. The PTO nanomesas were obtained from 3, 4, and 16 nm thick PTO films. The solid line is a linear fit to the data, with a slope of 0.93.

The height difference was found to increase at substrate temperatures above 530 °C, which suggests that the PTO growth rate on the SRO template is reduced accordingly. The measured dependence of Δh on lateral size and substrate temperature indicates that the growth rate of the PTO nanomesas is affected by the adatom surface diffusion. It has been previously shown that the adatom diffusivity increases with increasing growth temperature for similar deposition techniques [33, 34]. It is possible for adatoms arriving within a diffusion length of the template edges to migrate directly into

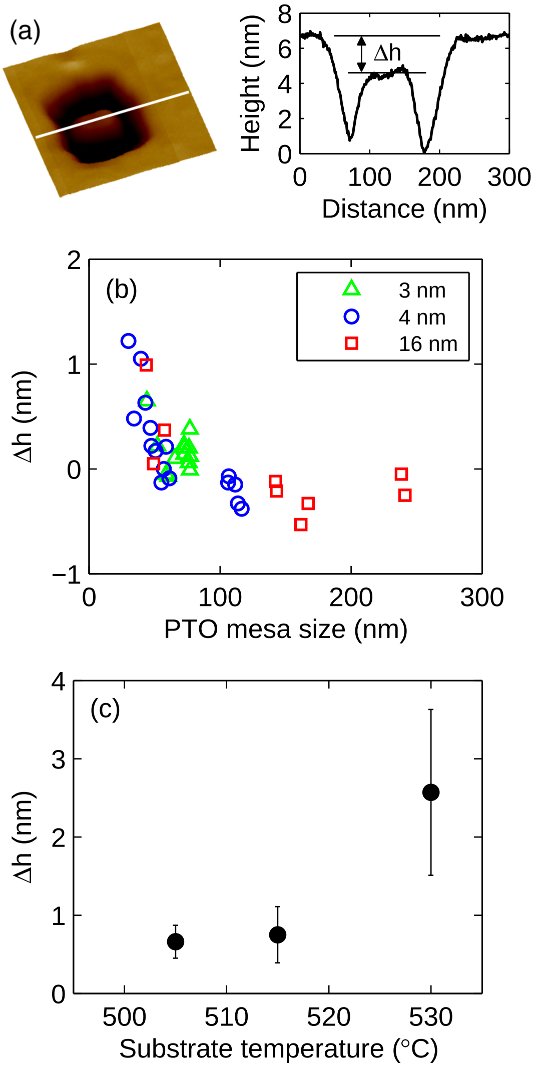

Figure 6.6: (a) Left: AFM topography image of a PTO nanomesa. Right: a cross-section profile along the center of the nanomesa surface, displaying a height difference, Δh, between the nanomesa surface and the surrounding film. (b) The height difference, Δh, versus the average lateral size of PTO nanomesas defined in 3, 4, and 16 nm thick PTO samples. (c) The dependence of Δh on substrate temperature. The data is obtained from PTO nanomesas of average lateral size $\sim 30 - 50$ nm, defined in three different ~ 4 nm thick PTO samples.

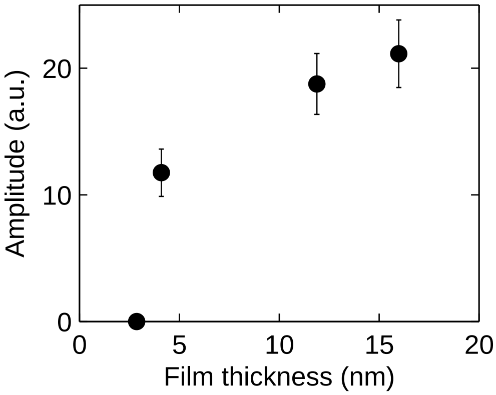

Figure 6.7: The dependence of the piezoelectric amplitude on the PTO film thickness. Note that the 3, 4 and 16 nm thick PTO films were grown on nanostructured SRO thin films.

the trenches of the SRO template, thereby effectively reducing the total number of atoms available for formation of the PTO nanomesa. Since the surface diffusion length increases with increasing growth temperature [33], more adatoms can diffuse into the STM-etched trenches, thus resulting in a lower growth rate for the PTO nanomesa. Similarly, when the size of the template is reduced, a larger proportion of adatoms may be expected to migrate to the trenches, thus contributing to the observed increase in Δh with decreasing template dimensions, shown in figure 6.6(b). Moreover, such growth scenarios are also in agreement with the observations from figure 6.5, in which the size of the PTO nanomesas was found to be smaller than that of the corresponding SRO templates.

In order to establish a reference level for the PTO nanomesas, piezore-

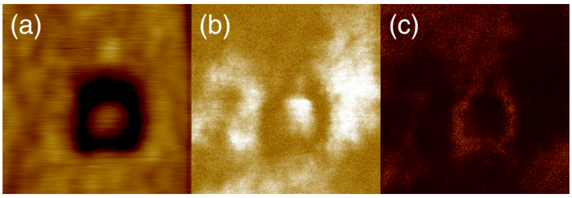

Figure 6.8: (a) PFM topography image of a pristine nanomesa defined in a 4 nm thick PTO sample. (b) Amplitude image revealing an increased piezoresponse on the nanomesa and the adjacent film region. (c) Phase image of the nanomesa. The scan size is 400×400 nm^2 for all three images.

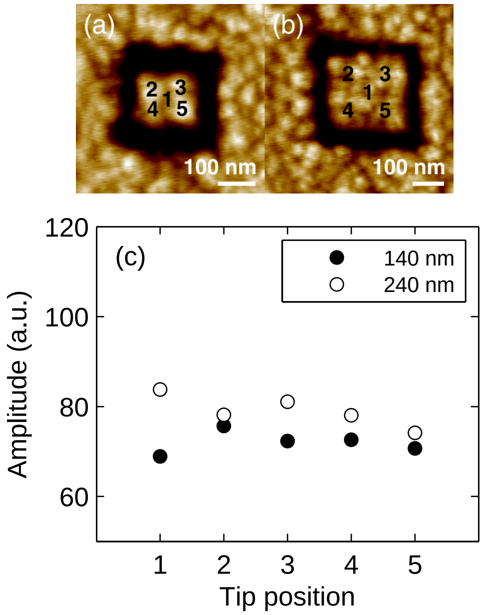

Figure 6.9: AFM topography images of PTO nanomesas defined in a 16 nm thick PTO sample with average lateral sizes (a) 140 nm and (b) 240 nm, respectively. The numbers denote the tip measurement positions. (c) Variation of the average piezoelectric amplitude with tip position for the two PTO nanomesas shown in (a) and (b).

sponse hysteresis loop measurements were performed on continuous films. Figure 6.7 shows the dependence of the piezoelectric amplitude on the PTO film thickness. The amplitude was found to drop gradually with decreasing film thickness from 16 to 4 nm, as was previously reported [7, 11]. We note that no piezoresponse hysteresis loop could be obtained on the $\sim$ 3 nm thick film in this study, as the measured signal dropped below the noise level of the PFM measurements.

Figure 6.8(a) shows a PFM topography scan of a pristine nanomesa with an average lateral size of $\sim$ 50 nm defined in a 4 nm thick PTO sample. Figures 6.8(b) and (c) show the amplitude and phase of the piezoresponse, measured on the PTO nanomesa. In the amplitude image, an increased amplitude is observed on the PTO nanomesa. Such an increase of the piezoelectric amplitude was also found close to the trenches right across from the nanomesa[5]. 3×3 μm^2 PFM scans revealed that these PTO thin

---

[5] The maximum amplitude level measured on the surrounding film was for certain structures larger than that measured on the PTO nanomesa.

film regions with increased piezoresponse are typically confined within an area of up to $\sim$ 200 nm from the trenches. In addition, the piezoelectric amplitude decreased markedly as the tip was scanned across the trenches.

The AFM scans in figures 6.9(a) and (b) depict two PTO nanomesas defined in a 16 nm thick PTO sample, with average lateral sizes of $\sim$ 140 and $\sim$ 240 nm, respectively. The numbers $1-5$ denote the various tip positions for the piezoelectric hysteresis loop measurements. The average piezoelectric amplitude showed little variation with the tip measurement position for both PTO nanomesas (figure 6.9(c)), suggesting that the piezoelectric response is homogeneous across the nanomesas.

Figure 6.10(a) shows piezoresponse hysteresis loops recorded on two PTO nanomesas in a 4 nm thick sample with average lateral size of $\sim$ 30 and $\sim$ 115 nm, respectively. As can be seen, the measured piezoelectric amplitude is strongly enhanced for the smaller nanomesa compared to that of the larger. Figure 6.10(b) displays the piezoelectric amplitude as a function of average lateral size for nanomesas defined in both 4 and 16 nm thick PTO samples. In this chart, the piezoelectric amplitude of the nanomesas is normalized with respect to the average amplitude measured on the continuous films. The error bars indicate the standard deviation, as calculated from hysteresis loops obtained with different tips, including different measurement positions on the nanomesa surface. For the nanomesas defined in the 4 nm thick PTO sample, the piezoelectric amplitude increases sharply with decreasing lateral size. For lateral dimensions below $\sim$ 60 nm, it is shown that the piezoelectric amplitude is up to $\sim$ 3 times larger than that of the continuous film. It was previously reported for 200 nm thick PZT structures, that the piezoelectric response increased when the structure was scaled down from 200 to 100 nm in lateral dimensions [15]. The present study confirms this trend, even for the smallest PTO nanomesas ($30 \times 30 \times 4$ nm^3). According to recent work [16, 35] the strain state in island nanostructures was found to be dependent on the aspect ratio of the nanostructure. For aspect ratios below 20 the in-plane strain is reduced compared to a continuous film [16]. Furthermore, the in-plane strain relaxation is most pronounced at the regions near the edges and corners and lowest in the center of the island, indicating that the clamping conditions are not uniform over the nanomesas. In the present study, the aspect ratio ranges from $\sim 7-30$ for the nanomesas in the 4 nm thick PTO film, indicating a strong increase of average strain relaxation as the dimension is reduced below 50 nm. AFM tips with a nominal tip radius of curvature of $20-25$ nm, and a tip–surface contact force of $\sim$ 200 nN, as derived from the force curve measurements, were used in the PFM measurements. Hence,

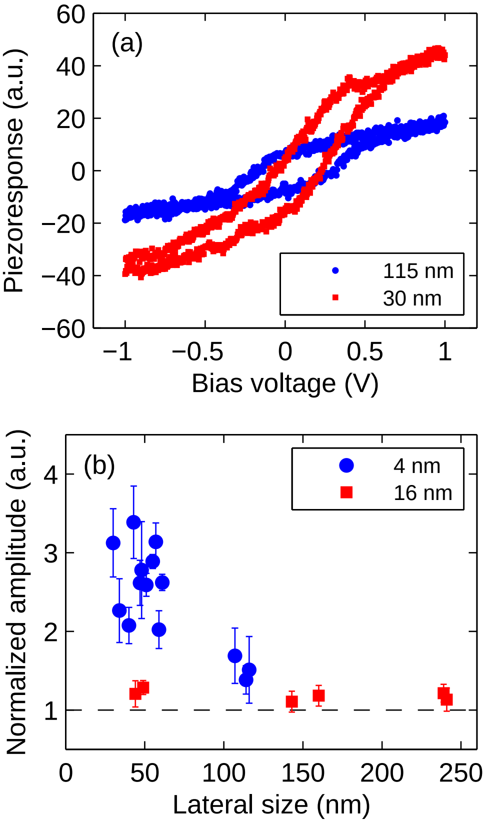

Figure 6.10: (a) Piezoresponse hysteresis loops recorded from nanomesas defined in a 4 nm thick PTO sample showing increased piezoresponse with decreasing lateral size. (b) Normalized piezoelectric amplitude as a function of the average lateral size for nanomesas obtained from 4 and 16 nm thick PTO samples. The dashed line indicates the reference piezoelectric amplitude obtained for a continuous film.

the PFM measurements were carried out in the strong indentation regime [36]. In this regime, the electric field distribution inside the ferroelectric is predominantly determined by the tip–surface contact area [36, 37], enabling to measure a true electromechanical response of the ferroelectric material underneath the tip. We note that there might also be a small contribution from the field distribution outside the contact area to the piezoelectric signal. It has been shown that the normal component of the electric field drops rapidly along the radial direction, reaching $\sim 1/3$ of the value at the tip apex at a distance corresponding to one tip radius [38]. As a result, the

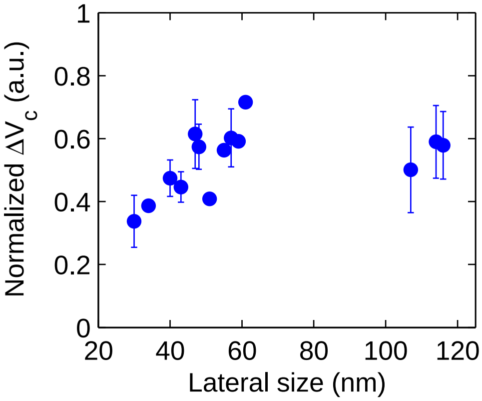

Figure 6.11: Normalized ΔV_c as a function of the average lateral size of the PTO nanomesas, as obtained from the 4 nm thick PTO sample. ΔV_c is defined as the difference between the positive and negative coercive voltages, i.e., $\Delta V_c = V_c^+ - V_c^-$. Here ΔV_c is normalized to the average ΔV_c measured on the continuous film.

entire mesa structure is believed to contribute to the signal for nanomesas below $50 - 60$ nm, the lateral size below which an appreciable reduction of in-plane strain is expected. Hence, we interpret the measured increase in piezoelectric amplitude as a result of the decrease of average in-plane strain upon shrinking the dimensions of the nanomesas [15, 18, 39, 40]. As the in-plane strain is reduced, the nanomesas may expand and contract more freely in lateral directions due to the electromechanical response determined by the piezoelectric coefficient d_{31}. This response is otherwise impeded by clamping of the continuous film to the substrate [41].

Figure 6.10(b) also reports that the measured piezoelectric amplitude does not vary significantly with nanomesa lateral size for the 16 nm thick PTO sample. This finding can be understood in terms of the contribution from the continuous PTO film underneath the nanomesa mounds, as illustrated in figure 6.4(f). However, it should be noted that the piezoelectric amplitude obtained from these nanomesas is still up to $\sim 30\%$ larger compared to that of the continuous film, presumably a result of the unclamped edges and sidewalls in the upper section of the nanomesas.

The dependence of the measured coercive voltage on the lateral size is shown in figure 6.11, where ΔV_c is plotted versus average lateral size of the PTO nanomesa for a 4 nm thick sample. $\Delta V_c = V_c^+ - V_c^-$, as derived from piezoresponse hysteresis loops, and is averaged over data obtained from different tip measurement positions and normalized to the average ΔV_c for a continuous film. ΔV_c was found to be nearly constant, at ~ 0.6 of the bulk ΔV_c value, for lateral sizes above ~ 50 nm, with appreciable reduction for lateral dimensions below ~ 50 nm. We note that for nanomesas smaller than ~ 160 nm lateral size in the 16 nm thick sample, ΔV_c is ~ 0.5 of the bulk ΔV_c value. In figure 6.11, the rapid decrease in ΔV_c appears in the same lateral size range for which a large increase in the piezoelectric amplitude was observed. For all lateral sizes, ΔV_c was found to be $\sim 2-3$ times lower than that of a continuous film. It has been previously verified both experimentally and theoretically that the coercive field is dependent on strain for homogeneous ferroelectric thin films [42, 43, 44, 45]. For strain-relaxed thin films, the energy barrier for domain nucleation is reduced, leading to a lower coercive field [44, 45]. As discussed above, when the nanomesa lateral size decreases, the in-plane strain is reduced due to relaxation at the free surfaces, including sidewalls [16, 46]. Hence, the present data supports a scenario where the observed decrease of ΔV_c is due to strain relaxation in the PTO nanomesas, when their lateral size is diminished.

6.4 Conclusions

We have developed a new technique for definition of ferroelectric nanostructures with lateral sizes down to a few tens of nanometers. This technique should in principle allow even smaller structures to be defined by carefully choosing STM nanostructuring parameters, template materials, and physical growth conditions. It also provides the possibility of maintaining nanostructured surfaces in thick homogeneous films. Moreover, the present approach should be suitable for definition of nanomesas in other material classes, such as superconductors, ferromagnets, and dielectrics, which renders probing of their physical properties at nanometer dimensions in a controlled fashion. We have shown that the piezoelectric response of 4 nm high PTO nanomesas increases with decreasing lateral size down to 30 nm. The coercive voltage of these PTO nanomesas was found to decrease with reduced lateral size.

References

[1] M. E. Lines and A. M. Glass. *Principles and Applications of Ferroelectrics and Related Materials.* Oxford: Clarendon Press, 1979.

[2] C. H. Ahn, K. M. Rabe, and J.-M. Triscone. Ferroelectricity at the nanoscale: Local polarization in oxide thin films and heterostructures. *Science*, 303:488, 2004.

[3] J. F. Scott. Applications of modern ferroelectrics. *Science*, 315:954, 2007.

[4] A. K. Sarin Kumar, P. Paruch, J.-M. Triscone, W. Daniau, S. Ballandras, L. Pellegrino, D. Marré, and T. Tybell. High-frequency surface acoustic wave device based on thin-film piezoelectric interdigital transducers. *Appl. Phys. Lett.*, 85:1757, 2004.

[5] B. W. Wessels. Ferroelectric epitaxial thin films for integrated optics. *Annu. Rev. Mater. Res.*, 37:659, 2007.

[6] S. Li, J. A. Eastman, Z. Li, C. M. Foster, R. E. Newnham, and L. E. Cross. Size effects in nanostructured ferroelectrics. *Phys. Lett. A*, 212:341, 1996.

[7] T. Tybell, C. H. Ahn, and J.-M. Triscone. Ferroelectricity in thin perovskite films. *Appl. Phys. Lett.*, 75:856, 1999.

[8] J. Junquera and P. Ghosez. Critical thickness for ferroelectricity in perovskite ultrathin films. *Nature*, 422:506, 2003.

[9] D. D. Fong, G. B. Stephenson, S. K. Streiffer, J. A. Eastman, O. Auciello, P. H. Fuoss, C. Thompson. Ferroelectricity in ultrathin perovskite films. *Science*, 304:1650, 2004.

[10] C. Lichtensteiger, J.-M. Triscone, J. Junquera, and P. Ghosez. Ferroelectricity and tetragonality in ultrathin $PbTiO_3$ films. *Phys. Rev. Lett.*, 94:047603, 2005.

[11] V. Nagarajan, J. Junquera, J. Q. He, C. L. Jia, R. Waser, K. Lee, Y. K. Kim, S. Baik, T. Zhao, R. Ramesh, P. Ghosez, and K. M. Rabe. Scaling of structure and electrical properties in ultrathin epitaxial ferroelectric heterostructures. *J. Appl. Phys.*, 100:051609, 2006.

[12] T. Tybell, P. Paruch, T. Giamarchi, and J.-M. Triscone. Domain wall creep in epitaxial ferroelectric $Pb(Zr_{0.2}Ti_{0.8})O_3$ thin films. *Phys. Rev. Lett.*, 89:097601, 2002.

[13] I. I. Naumov, L. Bellaiche, and H. Fu. Unusual phase transitions in ferroelectric nanodisks and nanorods. *Nature*, 432:737, 2004.

[14] M. Alexe, C. Harnagea, D. Hesse, and U. Gösele. Patterning and switching of nanosize ferroelectric memory cells. *Appl. Phys. Lett.*, 75:1793, 1999.

[15] S. Bühlmann, B. Dwir, J. Baborowski, and P. Muralt. Size effect in mesoscopic epitaxial ferroelectric structures: Increase of piezoelectric response with decreasing feature size. *Appl. Phys. Lett.*, 80:3195, 2002.

[16] K. Lee, H. Yi, W.-H. Park, Y. K. Kim, and S. Baik. Lateral size effects on domain structure in epitaxial $PbTiO_3$ thin films. *J. Appl. Phys.*, 100:051615, 2006.

[17] C. S. Ganpule, A. Stanishevsky, Q. Su, S. Aggarwal, J. Melngailis, E. Williams, and R. Ramesh. Scaling of ferroelectric properties in thin films. *Appl. Phys. Lett*, 75:409, 1999.

[18] V. Nagarajan, A. L. Roytburd, A. Stanishevsky, S. Prasertchoung, T. Zhao, L. Chen, J. Melngailis, O. Auciello, and R. Ramesh. Dynamics of ferroelastic domains in ferroelectric thin films. *Nat. Mater.*, 2:43, 2003.

[19] M.-W. Chu, I. Szafraniak, R. Scholz, C. Harnagea, D. Hesse, M. Alexe, and U. Gösele. Impact of misfit dislocations on the polarization instability of epitaxial nanostructured ferroelectric perovskites. *Nat. Mater.*, 3:87, 2004.

[20] A. Rüdiger, T. Schneller, A. Roelofs, S. Tiedke, T. Schmitz, and R. Waser. Nanosize ferroelectric oxides – tracking down the superparaelectric limit. *Appl. Phys. A*, 80:1247, 2005.

[21] H. Nonomura, M. Nagata, H. Fujisawa, M. Shimizu, H. Niu, and K. Honda. Structural control of self-assembled $PbTiO_3$ nanoislands fabricated by metalorganic chemical vapor deposition. *Appl. Phys. Lett.*, 86:163106, 2005.

[22] H.-J. Shin, J. H. Choi, H. J. Yang, Y. D. Park, Y. Kuk, and C.-J. Kang. Patterning of ferroelectric nanodot arrays using a silicon nitride shadow mask. *Appl. Phys. Lett.*, 87:113114, 2005.

[23] W. Lee, H. Han, A. Lotnyk, M. A. Schubert, S. Senz, M. Alexe, D. Hesse, S. Baik, and U. Gösele. Individually addressable epitaxial ferroelectric nanocapacitor arrays with near Tb inch^{-2} density. *Nat. Nanotechnol.*, 3:402, 2008.

[24] A. Kobayashi, F. Grey, R. S. Williams, and M. Aono. Formation of nanometer-scale grooves in silicon with a scanning tunneling microscope. *Science*, 259:1724, 1993.

[25] L. Pellegrino, E. Bellingeri, A. S. Siri, and D. Marré. Current-controlled lithography on conducting $SrTiO_{3-\delta}$ thin films by atomic force microscopy. *Appl. Phys. Lett.*, 87:064102, 2005.

[26] R. H. Kim, W. S. Ahn, S. H. Han, and S. K. Choi. Two-dimensional self-patterning of $PbTiO_3$ on a $Nb-SrTiO_3$ (001) surface using atomic force microscope lithography and hydrothermal epitaxy. *Appl. Phys. Lett.*, 90:172907, 2007.

[27] G. Bertsche, W. Clauss, and D. P. Kern. Nanometer-scale surface modifications of $YBa_2Cu_3O_{7-\delta}$ thin films using a scanning tunneling microscope. *Appl. Phys. Lett.*, 68:3632, 1996.

[28] C. C. You, N. V. Rystad, A. Borg, and T. Tybell. Nanoscale structuring of $SrRuO_3$ thin film surfaces by scanning tunneling microscopy. *Appl. Surf. Sci.*, 253:4704, 2007.

[29] C. Thompson, C. M. Foster, J. A. Eastman, and G. B. Stephenson. Observation of the polarization of domains in ferroelectric thin films using x-ray interference. *Appl. Phys. Lett.*, 71:3516, 1997.

[30] A. Gruverman and A. Kholkin. Nanoscale ferroelectrics: processing, characterization and future trends. *Rep. Prog. Phys.*, 69:2443–2474, 2006.

[31] Ø. Dahl, J. K. Grepstad, and T. Tybell. Crystalline and dielectric properties of sputter deposited $PbTiO_3$ thin films. *J. Appl. Phys.*, 103:114112, 2008.

[32] R. Takahashi, Ø. Dahl, E. Eberg, J. K. Grepstad, and T. Tybell. Ferroelectric stripe domains in $PbTiO_3$ thin films: Depolarization field and domain randomness. *J. Appl. Phys.*, 104:064109, 2008.

[33] J. H. Neave, P. J. Dobson, B. A. Joyce, and J. Zhang. Reflection high-energy electron diffraction oscillations from vicinal surfaces – a new pproach to surface diffusion measurements. *Appl. Phys. Lett.*, 47:100, 1985.

[34] G. Rijnders, D. H. A. Blank, J. Choi, and C. B. Eom. Enhanced surface diffusion through termination conversion during epitaxial $SrRuO_3$ growth. *Appl. Phys. Lett.*, 84:505, 2004.

[35] V. Nagarajan. Scaling of the piezoelectric response in ferroelectric nanostructures: An effective clamping stress model. *Appl. Phys. Lett.*, 87:242905, 2005.

[36] S. V. Kalinin and D. A. Bonnell. Imaging mechanism of piezoresponse force microscopy of ferroelectric surfaces. *Phys. Rev. B*, 65:125408, 2002.

[37] S. V. Kalinin, E. Karapetian, and M. Kachanov. Nanoelectromechanics of piezoresponse force microscopy. *Phys. Rev. B.*, 70:184101, 2004.

[38] D. A. Scrymgeour and J. W. P. Hsu. Absence of elastic clamping in quantitative piezoelectric force microscopy measurements of nanostructures. *Appl. Phys. Lett.*, 93:233114, 2008.

[39] A. L. Roytburd, S. P. Alpay, V. Nagarajan, C. S. Ganpule, S. Aggarwal, E. D. Williams, and R. Ramesh. Measurements of internal stresses via the polarization in epitaxial ferroelectric films. *Phys. Rev. Lett.*, 85:190, 2000.

[40] J.-H. Li, L. Chen, V. Nagarajan, R. Ramesh, and A. L. Roytburd. Finite element modeling of piezoresponse in nanostructured ferroelectric films. *Appl. Phys. Lett.*, 84:2626, 2004.

[41] K. Lefki and G. J. M. Dormans. Measurement of piezoelectric coefficients of ferroelectric thin films. *J. Appl. Phys.*, 76:1764, 1994.

[42] N. A. Pertsev, J. Rodríguez Contreras, V. G. Kukhar, B. Hermanns, H. Kohlstedt, and R. Waser. Coercive field of ultrathin $Pb(Zr_{0.52}Ti_{0.48})O_3$ epitaxial films. *Appl. Phys. Lett.*, 83:3356, 2003.

[43] K. J. Choi, M. Biegalski, Y. L. Li, A. Sharan, J. Schubert,R. Uecker, P. Reiche, Y. B. Chen, X. Q. Pan, V. Gopalan, L.-Q. Chen, D. G. Schlom, and C. B. Eom. Enhancement of ferroelectricity in strained $BaTiO_3$ thin films. *Science*, 306:1005, 2004.

[44] S. Choudhury, Y. L. Li, L. Q. Chen, and Q. X. Jia. Strain effect on coercive field of epitaxial barium titanate thin films. *Appl. Phys. Lett.*, 92:142907, 2008.

[45] J. Paul, T. Nishimatsu, Y. Kawazoe, and U. V. Waghmare. Polarization switching in epitaxial films of $BaTiO_3$: A molecular dynamics study. *Appl. Phys. Lett.*, 93:242905, 2008.

[46] J. X. Zhang, R. Wu, S. Choudhury, Y. L. Li, S. Y. Hu, and L. Q. Chen. Three-dimensional phase-field simulation of domain structures in ferroelectric islands. *Appl. Phys. Lett.*, 92:122906, 2008.

Chapter 7

Paper 3

Ferroelectric domain structure in $PbTiO_3$ nanomesas

Chang Chuan You, Ryota Takahashi, Anne Borg,
Jostein K. Grepstad, and Thomas Tybell

Preprint

Abstract

The ferroelectric domain structure in $PbTiO_3$ nanomesas was investigated by piezoresponse force microscopy under ambient conditions. The $PbTiO_3$ nanomesas were grown on nanostructured $SrRuO_3$ templates on $SrTiO_3$ substrates using off-axis radio frequency magnetron sputtering. It was found that the $PbTiO_3$ nanomesas, with a thickness of $\sim$ 4 nm and a lateral size down to $\sim$ 35 nm, had a polydomain structure, similar to that observed in the as-grown, surrounding, homogeneous PTO thin film.

7.1 Introduction

Ferroelectric materials are attractive for a wide range of applications due to their excellent dielectric, piezoelectric, and pyroelectric properties, for example in sensors, actuator, and non-volatile random access memories [1]. For many potential nanodevice applications, ferroelectric materials in the form of thin films or nanostructures are required. Previously, it has been shown that ferroelectric domain structures [2] and domain dynamics [3] have a profound influence on the physical properties of ferroelectric materials [4].

Hence, understanding the ferroelectric domain structure at the nanoscale is essential for the optimization of nanodevice performance.

For ferroelectric thin films, the influence film thickness has on the ferroelectric domain structure was recently studied both theoretically and experimentally for $Pb(Zr,Ti)O_3$ [5] and $PbTiO_3$ (PTO) [6]. It was shown that for PTO thin films with a monodomain structure, the depolarization field increases with decreasing film thickness. In order to reduce the depolarization energy, a monodomain configuration was found to switch to polydomain below a critical film thickness [6]. For ferroelectric nanostructures with a fixed thickness, an interesting question is whether or not such domain transition can take place for a certain critical lateral size, at which a monodomain structure becomes energetically favorable compared to polydomain structure. According to recent experimental results, the domain structure was found to be dependent on the lateral size for single separated PTO grains, fabricated on $Pt/TiO_2/SiO_2/Si$ substrates by chemical solution deposition [7]. It was found that the grains often exhibited two domains with 180° domain walls for a size in the range of $40-50$ nm, whereas the grains became monodomain for grain sizes smaller than 40 nm.

Here, we report a piezoresponse force microscopy (PFM) study of the ferroelectric domain structure in PTO thin films and nanomesas, sputter-deposited on as-grown and nanostructured $SrRuO_3$ (SRO) thin films. The PTO nanomesas had a well-defined and controlled geometry, with a thickness of ~ 4 nm and a lateral size ranging from $\sim 35-115$ nm.

7.2 Experimental

SRO thin films of thickness $\sim 40-50$ nm were grown on (001)-oriented single-crystalline $SrTiO_3$ (STO) substrates by off-axis radio frequency magnetron sputtering. A 100 mTorr atmosphere of oxygen and argon ($O_2 : Ar = 4 : 10$) and a substrate temperature of $\sim 590-690$ °C were used. PTO thin films were subsequently sputter-deposited onto SRO-coated STO substrates. The PTO films were grown in a 165 mTorr gas mixture of oxygen and argon ($O_2 : Ar = 4 : 10$). The substrate temperature was $\sim 510-520$ °C. Three different thicknesses of PTO films were used in this study: 4, 16, and 40 nm. The fabrication process of PTO nanomesas involved the following 4 steps: (1) Markers were defined into the STO substrates by electron beam lithography and Ar ion etching. (2) SRO thin films were sputter-deposited on the prestructured STO substrates. (3) Nanoscale templates were defined into SRO thin film surfaces, near the markers, by scanning tunneling microscopy (STM) lithography. Details on the STM etching of SRO templates

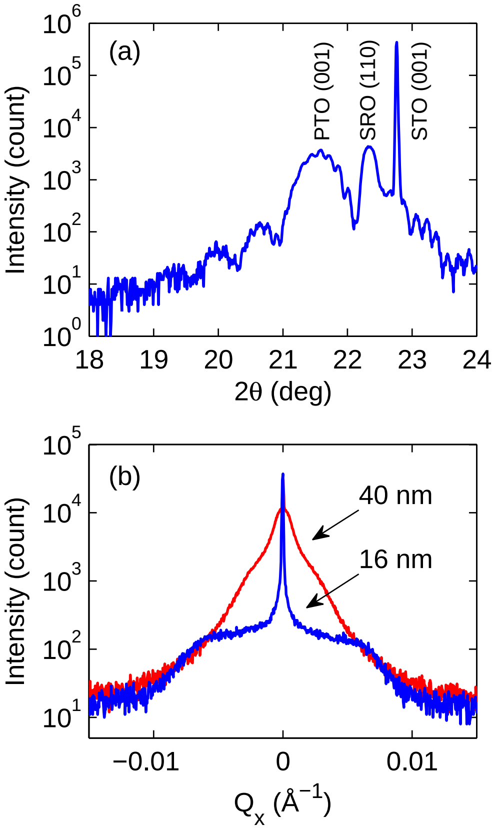

Figure 7.1: (a) $\theta - 2\theta$ diffractogram taken around the (001) reflection for a 16 nm thick PTO film grown on an SRO (110)/STO (001) heterostructure. (b) High-resolution linear Q_x-scans recorded around the (001) reflection for PTO thin films with thicknesses of 16 and 40 nm, revealing two apparent satellite peaks. These peaks were separated by the same ΔQ_x-value as measured from the specular reflection.

can be found elsewhere [8, 9]. (4) PTO thin films were grown on top of the nanostructured SRO templates to form mesas. Note that the SRO samples were cleaned with a nitrogen gas blow only prior to PTO film deposition.

The crystalline properties of PTO thin film samples were examined by x-ray diffraction (XRD) measurements, using a Bruker D8 Discover diffractometer. Figure 7.1(a) displays a representative $\theta - 2\theta$ diffractogram recorded around the (001) reflection for a PTO thin film, grown onto a (110)-oriented SRO layer on STO. The thickness of the PTO sample was 16 nm, as estimated from the thickness fringes observed around the (001) reflection. Notice that the thickness fringes due to the SRO thin film are superimposed on the PTO satellite peaks. The XRD data indicates c-axis oriented growth of a tetragonal PTO film, giving rise to an out-of-plane polarization. Rocking curve measurements of the (001) reflection showed a full width at half maximum of less than 0.03°, indicative of good crystalline quality. Furthermore, epitaxial growth for both PTO and SRO is inferred from ϕ-scans (not shown) of the PTO (101), SRO (112), and STO (101) reflections for a 16 nm thick PTO film on SRO/STO [9].

To check the ferroelectric domain structure we performed both XRD[1] and PFM measurements of PTO thin films, but only PFM for PTO nanomesas. PFM measurements [10, 11] were carried out in air and at room temperature, using a Veeco Multimode atomic force microscope (AFM) equipped with both internal and external (Stanford Research 830) lock-in amplifier systems and a signal access module. The AFM was operated in contact mode, and conductive Si tips coated with Pt/Ir were employed as a mobile top electrode. For normal PFM imaging, an AC bias voltage with amplitude 1 V and modulation frequency 10 kHz was applied between the scanning tip and the bottom SRO electrode layer, across the ferroelectric material. Typically, the scan rate was 0.2 Hz, the image resolution was 512×512 pixels, and the lock-in time constant was 10 ms. Since a ferroelectric material is also piezoelectric, it will deform in response to an applied electric field. The resulting piezoelectric response was recorded and analyzed by the amplifier system, leading to amplitude and phase signals. The amplitude is a measure of the local effective piezoelectric activity (averaged over a certain volume beneath the tip due to a localized electric field [12]), and the phase gives the direction of polarization in the ferroelectric material. In order to examine the initial domain structure in the PTO thin films, a $3 \times 3\ \mu\text{m}^2$ surface area was first switched by applying a negative DC bias voltage to the SRO bottom electrode, i.e., the resulting electric field is pointing along the surface to bottom direction, leading to a domain with down-polarization. At the center of that area, a $1 \times 1\ \mu\text{m}^2$ domain was subsequently written by applying a positive DC bias voltage, reversing the direction of polarization from down to up. Hence, the initial domain structure in the as-grown film regions can be determined by comparing the PFM signals measured from the oppositely polarized regions with those from the unpolarized regions (see figure 7.2). Typically, a scan rate of 0.5 Hz, an image resolution of 512×512 pixels, and a bias voltage of ±(3, 4, and 5) V were used to write domains in the 4, 16, and 40 nm thick PTO films, respectively. In addition,

---

[1] The experimental details of the XRD technique for probing the ferroelectric domain structure can be found elsewhere [2].

all domains were written twice to ensure a homogeneous polarization.

To probe the local piezoelectric hysteresis properties of PTO nanomesas, a DC bias voltage was applied to the bottom SRO electrode in addition to the tip AC bias voltage, while the amplitude and phase signals were continuously recorded. The DC bias voltage was ramped from −1 to +1 V in 512 steps with the duration of each step being 100 ms.

7.3 Results and discussion

Figure 7.1(b) shows high-resolution linear Q_x-profiles taken around the (001) reflection for 16 and 40 nm thick PTO films deposited on as-grown SRO/STO. On both sides of the specular reflection, a satellite peak can be clearly seen, separated by $\Delta Q_x = \pm 0.00825$ and ± 0.00288 for the 16 and 40 nm thick PTO films, respectively. These diffuse satellite peaks are attributed to the presence of ferroelectric in-plane stripe domains, oriented perpendicularly to the film surface with 180° domain walls, similar to those reported for PTO thin films grown on STO and Nb-doped STO substrates [2]. Hence, the XRD data indicates a polydomain structure for these samples. Furthermore, the stripe periodicity of the 16 and 40 nm thick PTO films are estimated at ~ 20 and ~ 56 nm, as derived from the ΔQ_x-values, in accordance with previous reported values for PTO samples grown on STO and Nb-doped STO substrates [2]. We note that for a 4 nm thick PTO sample, the stripe domain structure was not observed, possibly due to the low intensity of the specular reflection, as the intensity decreases with decreasing film thickness [2]. This might also be caused by a overlap of the PTO (001) and SRO (110) Bragg reflections. For PTO thin films, the *c*-axis lattice constant was found to be significantly reduced with decreasing film thickness [13], resulting in a shift of the PTO (001) Bragg peak towards the SRO (110) Bragg peak.

In order to determine the domain structure in a 4 nm thick PTO film the PFM technique was therefore employed instead. Figure 7.2 reports 5×5 μm^2 PFM amplitude (a), (d), and (g), phase (b), (e), and (h) images of ferroelectric domains written in 4, 16, and 40 nm thick PTO films, respectively. Figures 7.2(c), (f), and (i) display the piezoresponse data, defined as the in-phase component of the PFM signal (i.e., amplitude × cos(phase)), averaged over the cross-sectional profiles outlined in the PFM images. As shown, the piezoresponse signal measured from the unpolarized regions differ from the signals given by the areas written with negative and positive (−/+) bias voltages, suggesting that these samples are polydomain, consistent with the XRD data for the 16 and 40 nm thick PTO samples. However,

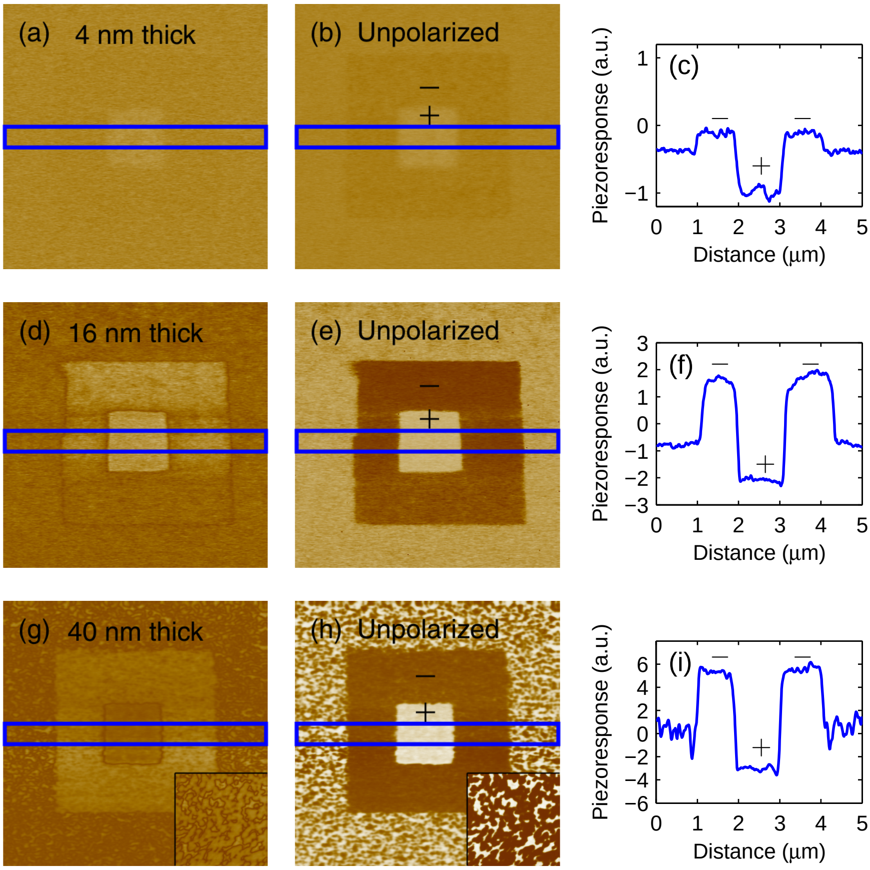

Figure 7.2: PFM scans (5×5 μm^2) of amplitude (a), (d), and (g), phase (b), (e), and (h), recorded after the application of DC bias voltages, with negative and positive polarities (−/+) across film surface areas of 3×3 μm^2 and 1×1 μm^2, to the PTO films with thicknesses of 4, 16, and 40 nm, respectively. Piezoresponse signals in (c), (f), and (i), corresponding to the average of the cross-sectional profiles marked in the PFM scans, indicate a polydomain structure in the 4, 16, and 40 nm thick PTO/SRO/STO samples. The insets in (g) and (h) show high-resolution (1×1 μm^2) amplitude and phase images taken from the unpolarized region.

according to a previous synchrotron XRD study [14], the PTO thin films, grown on SRO/STO substrates, were observed to be monodomain for film thicknesses down to 1.2 nm. This discrepancy may arise from the different electrostatic boundary conditions at the interfaces. In the present study, the PFM experiments were carried out in air, while in Ref. [14], the PTO surfaces were exposed to a vapor environment, providing free charges at the film surface. The presence of free charges has been verified theoretically to reduce the depolarization energy and thus stabilizes a monodomain configuration [14]. Another possibility is the thin film processing procedure, as we have obtained monodomain PTO samples when the PTO films were grown on SRO/STO without breaking the vacuum [15].

It should be pointed out that for the 40 nm thick PTO sample, the domains with different polarities were clearly distinguished, as shown by the insets in figures 7.2(g) and (h). In addition, the domain width was found to be in the range of $\sim 20 - 120$ nm. On the other hand, PFM measurements did not directly visualize the domain structure for the 4 and 16 nm thick PTO samples. As discussed above, the average domain width was found to decrease from 28 to 10 nm when the PTO film thickness was reduced from 40 to 16 nm. For the present study, AFM tips with a nominal tip radius of curvature of $20 - 25$ nm were used. Hence, it is possible that for the 4 and 16 nm thick PTO samples the domains are smaller than the tip resolution. Such a scenario is also in agreement with the piezoresponse data shown in figures 7.2(c) and (f), in which the PFM signal measured from an uniformly polarized monodomain was stronger than that from an unpolarized polydomain region, because the signal given by a polydomain region is averaged over the different domains with up- and down-polarizations when the domain size is smaller than the tip resolution[2]. In addition, all written domains were stable for at least 12 hours, although a slight decay of the PFM signal was observed.

Figures 7.3(a) and (d) show PFM topography images of two as-grown PTO nanomesas with an average lateral size of ~ 35 nm and ~ 115 nm, defined in the 4 nm thick PTO film. The PFM phase scans for the PTO nanomesas are displayed in figures 7.3(b) and (e), with scan sizes corresponding to the outlined areas in the topography images. Figures 7.3(c) and (f) report piezoresponse phase loops recorded locally on the PTO nanomesas. The up and down arrows in the phase loop indicate a domain with up- and down-polarization. For the switched domains with down-polarization in figures 7.3(c) and (f), the average phase signals were found to be $\sim -112 \pm 2^\circ$

---

[2] This is clearly demonstrated in figure 7.2(i) in which an average of the PFM signal given by a polydomain region is weaker than that of a monodomain region.

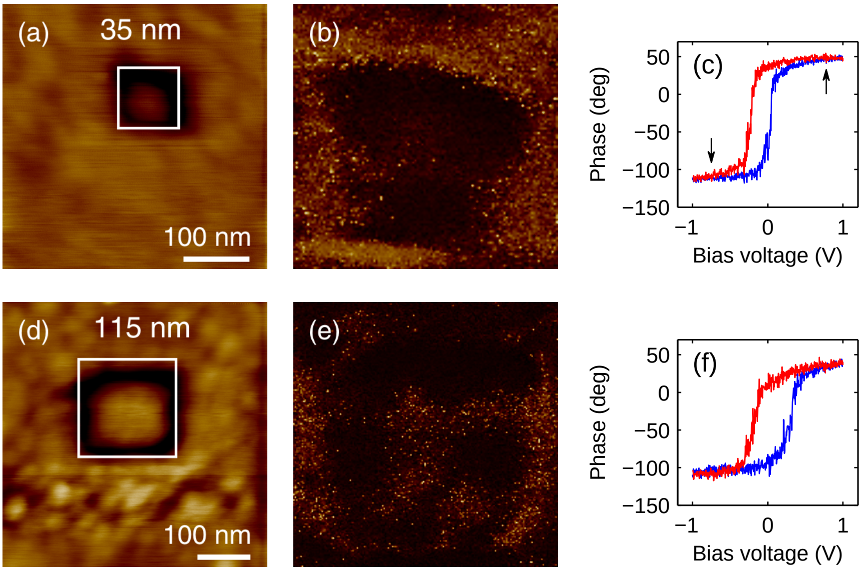

Figure 7.3: (a) and (d) PFM topography images taken from PTO nanomesas with lateral sizes of ∼ 35 and ∼ 115 nm, defined in a 4 nm thick PTO film grown on nanostructured SRO/STO templates. (b) and (e) PFM phase scans of the PTO nanomesas corresponding to the marked squares in (a) and (d), respectively. (c) and (f) display piezoresponse phase loops measured on the PTO nanomesas.

and $\sim -108 \pm 4°$, respectively. By comparing the phase signals obtained from the PFM imaging with those from the phase loop measurements, the initial domain structure of the PTO nanomesas can be determined. As can be seen from the PFM phase images, the phase response of the PTO nanomesas varied considerably across the mesa structures. The average PFM phase signals, as derived from the whole mesa, are estimated at $\sim -100 \pm 24°$ and $\sim -102 \pm 40°$ for the PTO nanomesas with 35 nm and 115 nm lateral sizes, which are significantly different as compared to those acquired from the phase loops. In particular, the variation of the PFM phase signals across the nanomesas is clearly manifested in the large standard deviation of the phase values[3]. This finding suggests that the PTO nanomesas are, overall, polydomain, similar to the domain structure observed in the as-grown homogeneous PTO thin film, as shown in figures 7.2(a)−(c). For an even distribution of up and down domains, the average

---

[3] The standard deviation of the average PFM signals measured from a homogeneous polydomain PTO film region is typically ∼ 40°.

phase signal from the nanomesa should be $\sim -30°$, according to the phase loops shown in figures 7.3(c) and (f). Hence, for an average phase signal of $\sim -100°$, a higher percentage of domains with down-polarization is expected. Moreover, it can be seen that the regions close to the edges and corners of the nanomesas often had a different phase response as compared to the regions near the center of the nanomesas. For regions close to the edges and corners, the phase signal is often the same as for a single domain, whereas the phase signal is similar to that of a polydomain for regions close to the center of the nanomesas. Previously, we have observed [9] that in-plane strain relaxation can take place in laterally confined nanostructures due to free surfaces at the edges and corners of the nanostructures, where strain relaxation is strongest. Hence, it is possible that the observed ferroelectric domain structure of the PTO nanomesas is related to the in-plane strain state, and their exact correlation needs to be addressed in further studies.

The observed domain structure of our smallest PTO nanomesa contrasts with the observations made in previous reports [7, 16]. For example, in Ref. [7], it was found that the PTO nanograins, prepared on platinum electrodes, became monodomain for a grain size below ~ 40 nm. We attribute this discrepancy to two possible effects: (1) The different results could stem from the different bottom electrodes used. According to recent theoretical findings [17], the depolarization field in ferroelectric perovskite nanocapacitors is reduced when platinum electrodes are used instead of SRO electrodes, thus promoting a monodomain structure. (2) The different geometry of the nanostructures since the depolarization field is geometry-dependent [18]. The depolarization effect is stronger for the PTO mesa structures with a parallel-plate geometry than for the PTO nanograins with a nearly spherical shape in Ref. [7].

7.4 Conclusions

We have used piezoresponse force microscopy to investigate the ferroelectric domain structure in PTO mesa structures, sputter-deposited on nanostructured SRO/STO templates. A polydomain structure was observed in the 4 nm thick PTO nanomesas, as well as in the surrounding, as-grown, homogeneous PTO film region. In addition, the polydomain structure of the PTO nanomesas, with a parallel-plate geometry, was found to be stable when decreasing the lateral size from 115 nm down to 35 nm.

References

[1] O. Auciello, J. F. Scoot, and R. Ramesh. The physics of ferroelectric memories. *Physics Today*, 51:22, 1998.

[2] R. Takahashi, Ø. Dahl, E. Eberg, J. K. Grepstad, and T. Tybell. Ferroelectric stripe domains in $PbTiO_3$ thin films: Depolarization field and domain randomness. *J. Appl. Phys.*, 104:064109, 2008.

[3] T. Tybell, P. Paruch, T. Giamarchi, and J.-M. Triscone. Domain wall creep in epitaxial ferroelectric $Pb(Zr_{0.2}Ti_{0.8})O_3$ thin films. *Phys. Rev. Lett.*, 89:097601, 2002.

[4] D. Damjanovic. Ferroelectric, dielectric and piezoelectric properties of ferroelectric thin films and ceramics. *Rep. Prog. Phys.*, 61:1267–1324, 1998.

[5] V. Nagarajan, J. Junquera, J. Q. He, C. L. Jia, R. Waser, K. Lee, Y. K. Kim, S. Baik, T. Zhao, R. Ramesh, P. Ghosez, and K. M. Rabe. Scaling of structure and electrical properties in ultrathin epitaxial ferroelectric heterostructures. *J. Appl. Phys.*, 100:051609, 2006.

[6] C. Lichtensteiger, M. Dawber, N. Stucki, J.-M. Triscone, J. Hoffman, J.-B. Yau, C. H. Ahn, L. Despont, and P. Aebi. Monodomain to polydomain transition in ferroelectric $PbTiO_3$ thin films with $La_{0.67}Sr_{0.33}MnO_3$ electrodes. *Appl. Phys. Lett.*, 90:052907, 2007.

[7] A. Roelofs, T. Schneller, K. Szot, and R. Waser. Piezoresponse force microscopy of lead titanate nanograins possibly reaching the limit of ferroelectricity. *Appl. Phys. Lett.*, 81:5231, 2002.

[8] C. C. You, N. V. Rystad, A. Borg, and T. Tybell. Nanoscale structuring of $SrRuO_3$ thin film surfaces by scanning tunneling microscopy. *Appl. Surf. Sci.*, 253:4704, 2007.

[9] C. C. You, R. Takahashi, A. Borg, J. K. Grepstad, and T. Tybell. The fabrication and characterization of $PbTiO_3$ nanomesas realized on nanostructured $SrRuO_3/SrTiO_3$ templates. *Nanotechnology*, 20:255705, 2009.

[10] T. Tybell, C. H. Ahn, and J.-M. Triscone. Ferroelectricity in thin perovskite films. *Appl. Phys. Lett.*, 75:856, 1999.

[11] S. V. Kalinin, B. J. Rodriguez, A. Y. Borisevich, A. P. Baddorf, N. Balke, H. J. Chang, L.-Q. Chen, S. Choudhury, S. Jesse, P. Maksymovych, M. P. Nikiforov, and S. J. Pennycook. Defect-mediated polarization switching in ferroelectrics and related materials: From mesoscopic mechanisms to atomistic control. *Adv. Mater.*, 21:1, 2009.

[12] S. V. Kalinin and D. A. Bonnell. Imaging mechanism of piezoresponse force microscopy of ferroelectric surfaces. *Phys. Rev. B*, 65:125408, 2002.

[13] Ø. Dahl, J. K. Grepstad, and T. Tybell. Crystalline and dielectric properties of sputter deposited $PbTiO_3$ thin films. *J. Appl. Phys.*, 103:114112, 2008.

[14] D. D. Fong, A. M. Kolpak, J. A. Eastman, S. K. Streiffer, P. H. Fuoss, G. B. Stephenson, C. Thompson, D. M. Kim, K. J. Choi, C. B. Eom, I. Grinberg, and A. M. Rappe. Stabilization of monodomain polarization in ultrathin $PbTiO_3$ films. *Phys. Rev. Lett.*, 96:127601, 2006.

[15] Ø. Dahl, J. K. Grepstad, and T. Tybell. Unpublished, 2009.

[16] H. Zeng, S. Lu, L. Dai, J. Liu, Z. Wang, and C. Zuo. Ferroelectric domain structure of discrete $PbTiO_3$ nanograins. *Mater. Lett.*, 59:2808, 2005.

[17] M. Stengel, D. Vanderbilt, and N. A. Spaldin. Enhancement of ferroelectricity at metal−oxide interfaces. *Nat. Mater.*, 8:392, 2009.

[18] A. N. Morozovska, E. A. Eliseev, and M. D. Glinchuk. Size effects and depolarization field influence on the phase diagrams of cylindrical ferroelectric nanoparticles. *Physica B*, 387:358, 2007.

Chapter 8

Conclusions and outlook

In the last decade, substantial progress has been made in the achievement of ferroelectric perovskite nanostructures using a wide variety of fabrication techniques. In the present study, we have demonstrated a novel fabrication scheme to realize $PbTiO_3$ mesa structures on nanostructured $SrRuO_3$ templates by off-axis radio frequency magnetron sputtering. It is also shown that scanning tunneling microscopy (STM) lithography can be used to define $SrRuO_3$ templates in a controllable and reproducible fashion.

The present fabrication scheme is based on a combination of top-down template patterning and subsequent bottom-up material deposition. It combines some of the best attributes of modern top-down and bottom-up approaches for achieving laterally confined nanostructures. For example, it provides the capability to define high-quality ferroelectric perovskite nanostructures with a well-defined and controllable geometry. Nanostructures with a sub-50 nm lateral size and a thickness down to a few nanometer can be achieved. In addition, the bottom-up deposition approach avoids processing damage from high-energetic ions, a common challenge for top-down techniques such as focused ion beam milling. The nanostructures can also be grown on appropriately chosen metallic templates, e.g., with a closely matched lattice constant, allowing ferroelectric size effects to be investigated under controlled electrical and mechanical boundary conditions, which, as pointed out in chapter 2.4, play a vital role for the stability of ferroelectricity and also in the formation of novel complex domain and polarization configurations in low-dimensional ferroelectric nanoscale systems. Furthermore, this fabrication scheme should in principle allow even smaller structures to be defined by carefully choosing STM nanostructuring parameters, template materials, and physical growth conditions. Ultimately, the minimum attainable size is determined by STM resolution.

The key challenges related to this fabrication technique are: (1) The growth rate of the $PbTiO_3$ nanomesas decreases with shrinking $SrRuO_3$ template size. (2) The average lateral size of the nanomesa is up to 10% smaller as compared to the corresponding template size. These two factors can adversely affect the size definition and control of smallest nanomesas. (3) The fabrication process is relatively slow due to the STM operation, and thus it is not suitable for large-scale manufacturing.

The fabrication scheme demonstrated in the present study also opens possibilities for definition of other technologically important materials, such as superconductors, multiferroics, ferromagnets, and antiferromagnets, permitting their physical properties to be probed at the nanoscale and in a controlled fashion. Moreover, the present template material, $SrRuO_3$, can be replaced with, for instance, a room-temperature metallic ferromagnetic perovskite oxide, such as $La_{0.7}Sr_{0.3}MnO_3$. By following the proposed fabrication procedure, nanostructures of a chosen material can be achieved on predefined $La_{0.7}Sr_{0.3}MnO_3$ templates using, e.g., physical deposition, leading to new combinations of oxide heterostructures. For example, for a heterostructure system such as $BiFeO_3/La_{0.7}Sr_{0.3}MnO_3$, it would be interesting to explore how exchange bias interaction between the multiferroic antiferromagnetic nanomesa and the ferromagnetic template material is influenced by size reduction.